

Christian-Albrechts-Universität zu Kiel

Institut für Geowissenschaften

Marine and Limnic Archaeological Prospection with Geoelectrics and Ground-Penetrating Radar

Dissertation zur Erlangung des Doktorgrades
der Mathematisch-Naturwissenschaftlichen Fakultät
der Christian-Albrechts-Universität zu Kiel

vorgelegt von

Annika Fediuk

Kiel, Juni 2022

Referent: Prof. Dr. Wolfgang Rabbel

Koreferent: Prof. Dr. Immo Trinks

Mündliche Prüfung: 30. August 2022

Zum Druck genehmigt: _____

Der Dekan

Abstract

In recent years, near-surface geophysical prospection of archaeological issues such as wooden shipwrecks or harbours in the littoral zone has gained increasing interest. So far, in shallow water environments (water depth < 5 m), seismic measurements usually have been chosen. The two methods geoelectrics and ground-penetrating radar (GPR) have hardly been used for archaeological prospection in littoral zones and are mostly known for their limitations in water environments. In addition, there is a lack of knowledge on the physical parameters of the materials to be prospected, including water-saturated, possibly weathered wood that was regularly used as construction material in northern Europe.

My thesis is based on three published papers. In two papers, I systematically investigate possible areas of application of the methods geoelectrics and GPR in the littoral zone with regard to archaeological prospection. A special focus is towards the application under field conditions. I investigate the methods' limitations and conditions under which they can be used individually or as a complementary method to seismics. For this, I focus on aspects of measurement accuracy, spatial resolution, depth penetration and material contrasts. The targeted prospection of the material wood with the methods is treated in detail in the third paper.

First, application possibilities of geoelectrics were exemplarily investigated by in situ measurements in the Baltic Sea and complemented by numerical resolution tests. Different measurement setups (towed vs. stationary and floating vs. lowered streamer) were compared. My results show that the method is suitable, amongst others, to resolve archaeological stone settings and groundwater upwelling areas. However, it is difficult to differentiate materials such as clay and sand in the sea bottom. This also applies to the differentiation of various rock formations with a porosity < 15%. For survey measurements and geological issues, time-saving towed, floating electrode arrays are well suited (spatial resolution on the seafloor > 2 m for a conductivity of 0.3 Ω m with a water depth of 1 m). Submerged electrodes should be used for archaeological prospection (spatial resolution of 0.5 m–1 m for the above conditions).

Second, the characteristics of GPR in water under field conditions were analysed based on four different measurement locations. Depending on the conductivity and attenuation coefficient of the water, penetration depths of 2 m–4 m were achieved, almost independent of the antenna frequency (200 MHz and 400 MHz) and the presence of organic material in the water column. The spatial resolution across profile direction is in the dm-m range, depending on the penetration depth. Therefore, an antenna array would have to be used for areal archaeological prospection with centimetre accuracy. In addition, it is recommended to choose an antenna frequency of 400 MHz, which, however, is disturbed massively by the effect of antenna ringing at water depths of >2 m. Numerous archaeological material contrasts such as peat and stone, sand and gyttia, and wood and stone can be resolved.

The topic of the third part is “wood”. In order to evaluate possibilities of prospecting archaeological wooden objects such as shipwrecks with GPR and geoelectrics, archae-

ological wood was approximated by unweathered, water-saturated "modern" softwood and hardwood. Its physical parameters were determined experimentally and material contrasts were calculated, which were used for depth estimations to resolve wooden objects with the methods. Both methods are suitable for the prospecting of wood in freshwater. GPR shows weaknesses in the contrast of hardwood in saturated sand and softwood in saturated clay. A 400 MHz antenna is able to resolve wooden objects of 0.1 m–0.5 m diameter at a depth of 1 m–3 m below the water surface. With geoelectrics, wooden objects with diameters of > 0.5 m can be detected at depths of > 0.5 m below the water surface.

This thesis enabled an accurate evaluation of the limitations of geoelectrics and GPR in water environments. This allows them to be used in the future for well-defined research issues and, in particular, to complement seismic measurements.

Zusammenfassung

Seit einigen Jahren gewinnt die oberflächennahe geophysikalische Prospektion in Uferzonen von archäologische Fragestellungen wie hölzernen Schiffswracks oder Häfen zunehmend an Interesse. Bisher wird im Flachwasserbereich (Wassertiefe < 5 m) zumeist die Methode Seismik gewählt. Die beiden Methoden Geoelektrik und Georadar wurden bisher kaum für die archäologische Prospektion in Uferzonen eingesetzt sind hauptsächlich für ihre Einschränkungen im Flachwasserbereich bekannt. Zudem fehlen Kenntnisse über die physikalischen Parameter der zu prospektierenden Materialien, u.a. wassergesättigtes, möglicherweise verwittertes Holz, das als Baustoff in Nordeuropa diente.

Meine Arbeit basiert auf drei veröffentlichten wissenschaftlichen Artikeln. In den ersten beiden Artikeln untersuche ich systematisch die möglichen Anwendungsgebiete der Methoden Geoelektrik und Georadar im Uferbereich hinsichtlich archäologischer Prospektion unter Feldbedingungen. Ich erforsche die Einschränkungen und Bedingungen, unter denen diese einzeln oder auch als zusätzliche Methode neben der Seismik eingesetzt werden können. Dazu betrachte ich Aspekte der Messgenauigkeit, räumlichen Auflösung, Tiefeneindringung und Materialkontraste. Die Prospektion des Materials Holz wird im dritten Artikel im Detail behandelt.

Zuerst wurden die Möglichkeiten der Geoelektrik beispielhaft durch in situ Messungen in der Ostsee ausgelotet und durch numerische Auflösungs-tests ergänzt. Verschiedene Messsetups (bewegtes vs. ortsfestes und schwimmendes vs. abgesenktes Elektrodenkabel) wurden verglichen. Meine Ergebnisse zeigen, dass die Methode u.a. geeignet ist, archäologische Steinsetzungen und Grundwasser-Austrittsgebiete zu detektieren. Schwierig ist es, Materialien wie Ton und Sand zu differenzieren. Dies trifft auch auf die Unterscheidung von verschiedenen Gesteinsformationen mit einer Porosität $< 15\%$ zu. Für Übersichtsmessungen und geologische Fragestellungen sind gezogene, schwimmende Elektrodenauslagen gut geeignet, da sie sehr zeitsparend sind (räumliche Auflösung am Meeresboden > 2 m für Leitfähigkeit $0,3 \Omega\text{m}$ mit einer Wassertiefe von 1 m). Für archäologische Prospektion sollten abgesenkte Elektroden verwendet werden (räumliche Auflösung von $0,5$ m– 1 m für obige Bedingungen).

Als zweites wurden die Besonderheiten von Georadar im Wasser unter Feldbedingungen anhand von vier verschiedenen Messlokalationen analysiert. Je nach Leitfähigkeit und Dämpfungskoeffizient des Wassers wurden Eindringtiefen von 2 m– 4 m erreicht, nahezu unabhängig von der Antennenfrequenz (200 MHz and 400 MHz) und dem Vorhandensein von organischem Material in der Wassersäule. Die räumliche Auflösung quer zur Profilrichtung liegt je nach Tiefe im dm-m Bereich, sodass für die flächenhafte zentimetergenaue archäologische Prospektion ein Antennenarray verwendet werden müsste. Zudem empfiehlt sich die Wahl der Antennenfrequenz von 400 MHz, die allerdings bei Wassertiefen von > 2 m massiv durch den Effekt des Antennenklingelns gestört wird. Es können zahlreiche Materialkontraste wie Torf und Stein, Sand und Gytta sowie Holz und Stein aufgelöst werden.

Das Thema der dritten Veröffentlichung ist „Holz“. Um Möglichkeiten der Prospek-

tion von archäologischen Holzobjekten wie Schiffswracks mit Georadar und Geoelektrik zu bewerten, wurde archäologisches Holz durch unverwittertes, wassergesättigtes „modernes“ Hart- und Weichholz approximiert. Dessen physikalische Parameter wurden experimentell ermittelt und Materialkontraste berechnet, die für die Tiefenabschätzungen zur Erkundung von Holzobjekten mit den Methoden verwendet wurden. Beide Methoden sind für die Prospektion von Holz insbesondere in Süßwasser geeignet. Georadar zeigt Schwächen beim Kontrast von Hartholz in gesättigtem Sand und Weichholz in gesättigtem Ton. Georadar (400 MHz) ist in der Lage, Holzobjekte von 0,1 m–0,5 m Durchmesser in 1 m–3 m Tiefe unter der Wasseroberfläche aufzulösen. Mit Geoelektrik können Hölzer mit einem Durchmesser von $>0,5$ m in $> 0,5$ m Tiefe unter der Wasseroberfläche detektiert werden.

Mithilfe der Arbeit können die Einschränkungen von Geoelektrik und Georadar im Flachwasserbereich genau eingeschätzt werden. Damit können sie zukünftig für genau definierte Fragestellungen eingesetzt werden und insbesondere die Methode Seismik ergänzen.

Contents

1	Introduction	1
1.1	Motivation	1
1.2	State of the art of geophysical methods applied in the littoral zone . . .	2
1.2.1	Seismics	3
1.2.2	Magnetics	3
1.2.3	Geoelectrics	4
1.2.4	Ground-Penetrating Radar	5
1.3	Study aim	6
1.4	Thesis outline	7
1.5	Authors' contributions	9
2	The applicability of an inverse Schlumberger array for near-surface targets in shallow water environments	11
2.1	Introduction	11
2.2	Methods	13
2.2.1	Measurement configurations, Field measurements and Investigated Materials	13
2.2.2	Repeated field measurements	16
2.2.3	Resolution of layer thickness and resistivity in 1D media	20
2.2.4	Spatial resolution in 2D media	23
2.3	Results	25
2.3.1	Repeated field measurements	25
2.3.2	Resolution of layer thickness and resistivity in 1D media	30
2.3.3	Spatial resolution in 2D media	33
2.4	Discussion	35
2.4.1	Repeated Field Measurements	35
2.4.2	Spatial resolution	36
2.4.3	Depth of penetration	37
2.4.4	Inversion ambiguity	38
2.4.5	The preferable measurement setup for prospecting a 2L respectively 3L/4L case	39
2.5	Conclusion	40
2.6	Appendix A	40
2.6.1	Resolution of layer thickness and resistivity from forward modelling of layered media	40
2.7	Appendix B	42
2.7.1	Sensitivity kernels	42

3	Ground- Penetrating Radar measurements in shallow water environments- a case study	51
3.1	Introduction	51
3.2	Measurement locations	54
3.3	Methods	56
3.3.1	GPR data acquisition and standard processing	58
3.3.2	Study procedure	60
3.4	Results	68
3.4.1	Attenuation effects	68
3.4.2	Maximum sounding depth	71
3.4.3	Spatial resolution	74
3.4.4	Material contrasts in field applications	76
3.5	Discussion	78
3.5.1	Maximum Sounding Depth	78
3.5.2	Spatial resolution and antenna directivity	81
3.5.3	Material contrasts	82
3.6	Conclusion	83
4	Physical Parameters and Contrasts of Wooden Objects in Lacustrine En- vironment: Ground Penetrating Radar and Geoelectrics	85
4.1	Introduction	85
4.2	Materials and Methods	87
4.2.1	Preliminary Considerations to Determine Wooden Material Prop- erties	87
4.2.2	Experimental Setup	88
4.2.3	Determination of the Electric Resistivity	90
4.2.4	Determination of the Dielectric Permittivity	91
4.2.5	Determination of Relative Material Parameter Contrasts	92
4.2.6	Geophysical Detection Swell of Wooden Targets in Lacustrine Environment	93
4.3	Results	95
4.3.1	Water Absorption, Swelling, and Density Increase of Moisturized Wood during the Experiment	95
4.3.2	Electric Resistivity	96
4.3.3	Dielectric Permittivity	99
4.3.4	Relative Material Parameter Contrasts	99
4.3.5	Geophysical Detection Swell of Wooden Targets in Lacustrine Environment	101
4.4	Discussion	102
4.4.1	Swelling and Density Increase of Moisturized Wood during the Experiment	102
4.4.2	Electric Resistivity	105
4.4.3	Dielectric Permittivity	106
4.4.4	Relative Material Parameter Contrasts	107
4.4.5	Comparison of Measurement Methods	108

4.4.6	Conclusions	108
5	Conclusion	111
6	Outlook	115
6.1	Geoelectrics	115
6.2	Ground-Penetrating Radar	116
6.3	Material contrasts of wood	117
6.4	Example of application: A Viking age ship in Hadebyer Noor, Schleswig, Germany	118
	Bibliography	123
	List of Figures	138
	List of Tables	141

1 Introduction

Und das Thema heute, es heißt Holz.

(275ers, Holz, 2016)

1.1 Motivation

Near-surface geophysical prospection of targets from meter to centimeter size has been successfully carried out on land for many years (Linington, 1963; Mommsen, 1986; Stümpel, 1988), especially for archaeological issues, e.g. house fundamentals, graves and fortifications. In addition, there are applications from the field of engineering geophysics (Mellett, 1995; Wightman et al., 2003), e.g. the maintenance of pipes and highways and from explosive ordnance clearance for recovering munitions and bombs (Butler, 1997; Bowers and Bidwell, 1999). Geophysical methods used frequently on land are magnetics, geoelectrics, ground-penetrating radar (GPR) and seismics (so far less used for objects than for landscape reconstruction) (Beblo, 1997; Knödel et al., 2013; Johnson, 2004). These methods offer different physical parameters to resolve the material contrast between the target and its surrounding material and different limitations in depth penetration and spatial resolution. Depending on the object material, dimensions, depth and the environmental parameters, the methods show certain strengths and weaknesses (see section 1.2). Thus, especially the combination of methods offers several advantages (Woelz et al., 2004; Wunderlich et al., 2015a). As an example, archaeological constructions often consist of various materials such as e.g. stones and wood that can be distinguished using different methods. Another point is, that the physical properties of typical materials in the subsurface are well known (Schön, 1983; Butler, 2005), but often have a wide range, so that ambiguities can be excluded more successfully using several methods.

In recent years, interest in the prospection of marine and limnic (archaeological) issues in the centimetre to decimetre range and in water depths of less than 10 m has increased e.g. (Kritikakis et al., 2015). However, there are still few approaches since the 1980s to resolve those structures. This includes, for example, the prospection of the harbours of Haithabu (Stümpel and Meissner, 1982) and Alexandria (Goddio, 1998). Other targets were archaeological shipwrecks, ports and geoarchaeological evidence of port environments (Passaro, 2010; Fediuk et al., 2019; Seeliger et al., 2013).

In addition, objects that were submerged due to rising sea level or river relocations were prospected (Müller et al., 2009; Simyrdanis et al., 2016; Seeliger et al., 2014).

Other problems included the recovery of logs (Jol and Albrecht, 2004) and of objects for the investigation of accidents (Ruffell, 2006, 2014) and the search for explosive ordnance (Arcone et al., 2010). Investigations regarding the morphology, stratigraphy or bathymetry of lakes, rivers and coastal waters as well as freshwater upwelling below the seafloor have been more regularly published (Manheim et al., 2004; Arcone et al., 1992; Sellmann et al., 1992)

It will be desirable to apply all methods approved on land in the water in order to have the largest selection of methods available here as well. However, due to the physical parameters of the water column as well as the sensitivity of the methods, the conditions for the application of the methods in water sometimes change considerably. The most widely used method in shallow water of <10 m depth is seismics, whose spatial resolution in the centimetre range benefits from the presence of a water column as frequencies in the kilohertz range can be used here (Bull et al., 2005; Plets et al., 2009; Wilken et al., 2019). Magnetics can be applied in shallow water with appropriate equipment, since the water column has a negligible magnetization and therefore the physical parameters do not change (Klein, 2011; Boyce et al., 2004). This is different with the methods geoelectrics and GPR. The decreased specific resistivity of the water column with increasing salinity has a limiting influence on the applicability of these methods (Loke et al., 2013; Arcone, 1995). So, they have been used less so far for issues in the littoral zone. Moreover, the remaining potential application areas have not been systematically investigated yet. In detail, the advantages and disadvantages of the methods as well as their current fields of application are described in the next section. The water column also affects the material parameters of submerged objects and their surrounding soil. The physical parameters, such as the seismic velocity, density, the specific resistivity and the dielectric permittivity are well known for the materials water-saturated sand, clay and weathered rocks can be found in numerous literature (Schön, 1983; Butler, 2005). However, the physical parameters of resistivity and dielectric permittivity are not sufficiently known for many other water-saturated materials, e.g. wood. As wood is a very common building material for ships and houses in Northern Europe (McGrail, 2014; Crumlin-Pedersen, 2004; Diener, 2012), there are also many archaeological wooden targets that show a wide range of wood species and possible weathering. The knowledge on the parameters of water-saturated wood is therefore very important. In summary, the application of the geophysical methods geoelectrics and GPR in the littoral zone still offers opportunities for development, especially for wooden targets.

1.2 State of the art of geophysical methods applied in the littoral zone

This chapter provides an introduction of the currently used geophysical methods in the littoral zone and of their advantages and disadvantages. In addition to a brief discussion of depth penetration and spatial resolution, the current application fields of the methods are presented.

1.2.1 Seismics

In this method, longitudinal seismic waves (P-Waves) are mechanically induced from various sources, e.g. a pinger and propagate at different velocities, according to the material in the subsurface. They are sensitive to changes in elastic subsoil properties, which are the elastic, shear and bulk modulus and the Poisson's ratio as well as to changes in the density. The travel time of P-waves, which are reflected at interfaces in the subsurface, is registered with a hydrophone and then evaluated. Usually, the travel time is converted to the depth scale using the velocities.

A great advantage is that there is only low attenuation of the seismic waves in water. Therefore, measurement frequencies in the kilohertz range can be applied depending the required resolution and depth penetration of a problem (Stümpel and Meissner, 1982). Disadvantages of the method are the interference of the measured signal by multiple reflections of the seafloor, as well as an attenuation of the signal by gases in the subsurface (Whiticar et al., 1986) or vegetation in the water column (Kovacs, 1991).

The resolution is in the decimeter range. For single channel measurements, a measurement frequency of 4 kHz and a water velocity of $v = 1500 \frac{\text{m}}{\text{s}}$, the spatial resolution in profile direction after migration is 10 cm (Fediuk et al., 2019; Wilken et al., 2019). An improvement of the horizontal resolution across the profile direction to those in profile direction can be achieved by multi-channel systems (Bull et al., 2005; Gutowski et al., 2008). At a frequency of 4 kHz, the depth penetration of the method in water-saturated sandy sediments below a 2 m–10 m thick water column is more than 25 m below the sea surface (Fediuk et al., 2019). This is the main reason it is the most commonly used method in the littoral zone so far.

First experiences with seismic prospection in shallow water (depth <10 m) were acquired by investigating a shipwreck (McKee, 1973) and the harbour of Haithabu (Stümpel and Meissner, 1982). Currently, numerous applications are known in harbour environments (Müller et al., 2009; Fediuk et al., 2019), for the prospection of shipwrecks (Plets et al., 2009; Grøn et al., 2015; Wilken et al., 2019) and for wooden poles (GRØN et al., 2007).

1.2.2 Magnetics

Magnetic measurements record changes of the earth's magnetic field (Knödel et al., 2013) due to variations in the subsurface. The changes are caused by induced and remanent magnetization (Le Borgne, 1955).

The advantage of the method is that the magnetization of the water column is negligible, and the application in water is well realisable when using waterproof equipment. Also, the method can cover large areas in a time-saving manner using arrays of multiple sensors (Fassbinder, 2009). For that, total field magnetometers or gradiometers are used. Disadvantages are that the method does not provide direct information on depth of the object of interest and that, for example, materials with ferromagnetic properties such as iron waste or volcanic rocks can mask surrounding structures due

to their large anomalies. The measurement coverage is dependent on the handling and navigability of the equipment (Scollar et al., 1990). Due to the water column, there is an increased distance of the sensors to magnetic anomaly sources, which reduces the signal strength. Depending on the bathymetry, the measured signals are of irregular strength, which can lead to erroneous interpretation of the data without any corrections (Blakely, 1996).

The depth resolution of the method depends, among others, on the position, size and susceptibility of the object in the soil. On average, signals can be received from 1 m–2 m depth below the magnetic sensors and from objects of metre to centimetre size. The data coverage usually is in the centimeter range in profile direction and in the decimeter range across the profile.

Only in recent years there have also been initial approaches for the reconstruction of archaeological targets in shallow water, e.g. a sunken military ship (Passaro, 2010) and the harbour piers of Caesarea Maritima in Israel (Boyce et al., 2004). Passaro (2010) used the Overhauser magnetometer "Sea Spy", towed 20 m behind a boat, which provides total field measurements. The sensor position, as well as influences of the bathymetry and of diurnal variations were corrected in the data before they were interpolated on a 10 m × 10 m grid. Boyce et al. (2004) used the same measurement setup and a similar data processing. Here, the data was interpolated to a 3 m × 3 m grid. Magnetic prospection with centimetre resolution was done by Klein (2011), presenting a study of magnetic prospection in the harbour basin of Elaia, Turkey and by Wunderlich et al. (2015b), surveying the harbour basin of Groß Strömkendorf.

1.2.3 Geoelectrics

With geoelectrics, changes in the electric resistivity of the subsurface are detected (Knödel et al., 2013). These are caused, for example, by a change in porosity, water or electrolyte content. In the standard application, a four electrode layout is used to inject a current into the ground at two points. The resulting potential field is measured from the other points. Since the subsurface is heterogeneous, an apparent resistivity value of a soil volume is measured. The specific resistivity distribution of the subsurface can therefore only be determined by inversion approaches. The method is used both in 1D for depth sounding and in 2D, 2.5D and 3D for earth resistivity tomography (Beblo, 1997). However, the equivalence principle, which describes ambiguous solutions of the modelling of the subsurface, must always be considered for the interpretation of data.

A major advantage of the method is that it can be applied in most environmental conditions. The (saline) water column allows a very good coupling of the electrodes to the water layer and provides new opportunities to use different measurement setups (floating vs. lowered and towed vs. stationary electrodes). These can be used depending on the application where faster (floating, towing) or very precise (lowered, stationary) measurements are required. A disadvantage is that the apparent resistivity can be seen as a weighted average of the resistivity of all bodies through which

the current flows. Since the current flows mainly through the water, the bottom below the water column hardly contributes to the measured values. In the following inversion it is hardly possible to determine the correct specific resistivity of the soil or even to resolve variations of the specific resistivity in the soil. This can be overcome by a very long measurement setup, which in turn, makes the measurements very time-consuming.

The water depth, water conductivity, measurement configuration and the electrode layout influence the spatial resolution and the depth of penetration of the method. The resolution is usually in the decimetre to metre range. Most archaeological prospection studies have average penetration depths up to about 5 m below the water surface.

There are only a few specific applications on archaeological prospection in the Mediterranean area of Roman wall fundamentals (Seeliger et al., 2014; Kritikakis et al., 2015; Simyrdanis et al., 2016). In this context, the feasibility of the method for prospecting wall foundations was systematically tested for the first time (Simyrdanis et al., 2015).

1.2.4 Ground-Penetrating Radar

Ground-penetrating radar (GPR) is sensitive to changes in the dielectric permittivity and the specific resistivity of the soil. The sensitivity of the method for changes in the magnetic permeability is mostly neglected under the assumption that the soil has a constant permeability. The permittivity refers to the polarisation capability of a material by electric fields. A unique aspect of water is that it is the material with the highest permittivity of approx. 81. GPR antennas transmit electromagnetic waves into the ground, which are partly reflected, absorbed or transmitted by interfaces caused by changes of above parameters. The travel times and amplitudes are recorded. The GPR frequency spectrum ranges from 30 MHz to 3 GHz (Kovacs, 1991).

Advantages of the method are a fast and simple application of the land equipment in the water. In addition, the data can be examined on site. Furthermore, because water has such a high permittivity, the contrasts to other materials are strong. The major disadvantage of the method is the growing attenuation of the electromagnetic waves with increasing salinity of the water. Thus, the method cannot be used at all in the sea and brackish water. In addition, GPR antennas are actually built for low permittivity environments, (e.g. granite with a permittivity of 3). This results in antenna ringing in the water, which reduces data quality, and a frequency decrease of about 25 % (Kovacs et al., 1985).

The spatial resolution as well as the depth penetration of the method is mostly frequency dependent. For a prospection of archaeological objects in water, frequencies of 200 MHz–400 MHz are mainly used. Therefore, the spatial resolution is in the centimetre to decimetre range. The depth penetration is a few metres.

So far, only the strong contrast between ice and groundwater (Schwamborn et al., 2002; Annan and Davis, 1977) and geological issues (Sellmann et al., 1992; Sambuelli and Bava, 2012; Sambuelli et al., 2009) have been prospected. For some years now, there

have also been a few applications for the localization of objects, e.g. wood and ordnances (Jol and Albrecht, 2004; Arcone et al., 2010). In addition, the location of a jet ski was reconstructed (Ruffell, 2006) and walls were searched for in the Black Sea (Abramov and Vasiliev, 2004).

1.3 Study aim

The previous sections show that there are promising objectives in the shallow water (depth <10 m) and that several geophysical methods are available for this purpose. Thus, studies on applications in shallow water are increasing, but methodological investigations have so far always been limited to the respective problem. In particular for the methods geoelectrics and GPR, there are no systematic studies whether and under which conditions they can be used for archaeological prospection complementary or alternatively to seismic measurements, considering the limitations due to the physical parameters of the water column. In addition, the materials of potential targets, especially wooden constructions in the surrounding soil, have not yet been systematically investigated according to their physical parameters.

For geoelectrics, the methodological approach of some studies was mainly focused to overcome the influence of the water column for the respective problem. A common approach has been to compare inversion results of synthetic 2D data (Simyrdanis et al., 2015; Orlando, 2013). Simyrdanis et al. (2015) are the only ones to study archaeological issues, such as underwater wall fundamentals below a salty water column, differentiating between measurement configurations as well as between submerged and floating electrodes. Another approach was to calculate vertical sounding curves (VES) approximating shallow water two-layer and three-layer cases for respective problems (Kwon et al., 2005; Orlando, 2013). As a third approach, Mansoor and Slater (2007) calculated sensitivity kernels for various electrode configurations in a homogenous subsurface and investigated measurement uncertainties. Only Lagabrielle (1983) showed VES curves for submerged and floating electrodes, for various scenarios in the soil, regardless of one specific issue. What is missing is an integrated analysis of field measurement uncertainty, theoretical spatial resolution of vertical sounding curves and 2D profiles for two and three/four layer geology models, as well as sensitivity and inversion reproducibility analyses for different measurement setups of a marine geoelectric system.

In contrast to geoelectrics, some methodical studies have been published for the prospection of GPR in water, which allow general conclusions to be drawn on the behaviour of the method in water. This was mostly done for antenna frequencies below 100 MHz. The behaviour of a GPR antenna in water including frequency reduction and the effect of ringing is well known (Kovacs, 1991). Various studies have been carried out to estimate the depth penetration of different antenna systems depending on water depth, conductivity and lake bottom parameters (Annan et al., 1977; Sellmann et al., 1992). The antenna radiation characteristics and their resulting footprint size (as a function of water depth) have also been determined in various approaches, both theoretically and

practically for a 50 MHz antenna (Arcone, 1995; Sellmann et al., 1992), as well as for the 200 MHz antenna (Wensink et al., 1990). There are hardly studies that specifically address the requirements for the prospection of archaeological issues in water (using 400 MHz and 200 MHz antennas) and take into account the measurement conditions in the field. This includes, for example, the influence of noise caused by turbulence, as well as of organic material on the penetration depth. Further points are the resolution in the water and the expected material contrasts.

For the archaeological material wood, the seismic parameters of softwood and hardwood in weathered and unweathered state and its material contrasts to different surrounding materials have already been investigated very precisely in two studies (Dix et al., 2001; Arnott et al., 2005). However, the electric resistivity and the dielectric permittivity of wood, which is also used as a construction material (McGrail, 2014; Crumlin-Pedersen, 2004; Diener, 2012), is mostly known from investigations of the wood industry (Niemz and Sonderegger, 2017; Kollmann, 1968; Skaar, 2012). Here, most studies focus on wood moisture contents of 0-30% (Peyskens et al., 1984), which are not representing the expected higher moisture content of fully water-saturated (archaeological) wood. The studies focussing on fully water-saturated wood do not cover all aspects regarding the influence of structural orientation and the distinction between hardwood and softwood (Niemz and Sonderegger, 2017). In addition, the values of the electrical resistivity and dielectric permittivity are usually not determined using a four point geoelectrical array or a GPR antenna (Niemz and Sonderegger, 2017). So far, no research has been done to determine the electrical resistivity and dielectric permittivity of water-saturated softwoods and hardwoods, taking into account all the above mentioned points, as well as to determine and evaluate the material contrasts of different woods to various environmental materials.

From the above aspects, the central theme for this thesis follows:

What can we expect in terms of depth penetration, resolution and detectable material contrasts in shallow water (depth <10 m) for the prospection of archaeological issues regarding

- i) Geoelectrics
- ii) GPR
- iii) The material wood, using above methods

and which further fields of application arise?

1.4 Thesis outline

The three research questions defined in section 1.3. are discussed in the following chapters based on three scientific papers, which form the main body of this thesis.

1) The applicability of an inverse Schlumberger array for near-surface targets in shallow water environments

Fediuk, A., Wilken, D., Thorwart, M., Wunderlich, T., Erkul, E., and Rabbel, W. Remote Sensing 2020, 12(13), 2132.

2) Ground-Penetrating Radar measurements in shallow water environments- a case study

Fediuk, A., Wilken, D., Wunderlich, T., and Rabbel, W. Remote Sensing 2022, 14(15), 3659.

3) Physical parameters and contrasts of wooden objects in lacustrine environment: Ground-penetrating radar and geoelectrics

Fediuk, A., Wilken, D., Wunderlich, T., and Rabbel, W. Geosciences 2020, 10(4), 146.

The first paper focuses on the applicability of geoelectrics in shallow water. We systematically investigate shore-parallel measurements of a multi-electrode streamer in a brackish water column of about 1 m and 0.3 Ω m. An inverse Schlumberger configuration as a compromise between horizontal and vertical resolution is used. Different measurement setups are distinguished (mobile vs. stationary as well as floating vs. submerged). As a preliminary step, we determine the measurement accuracy. This is followed by the determination of the resolution of layer thickness and resistivity for the prospection of three to four layers (1D) and objects (2D), as well as of the inversion reproducibility. Therefore, we use amongst others forward modelling and sensitivity calculation of synthetic data.

In the second paper we investigate specific features of GPR measurements in shallow water at different survey locations, as well as the methodological requirements for archaeological prospection. We use measurements of a 200 MHz and 400 MHz antenna at four different measuring locations with different water depths, conductivity and ground material parameters: A swimming pool, a river, a flooded gravel pit and a pond. The noise level in the water column and at the end of the radargram allows conclusions to be drawn on the penetration depth. We check the influence of organic material in the water column on the measurements. In addition, we test different resolution criteria theoretically and practically and study the antenna radiation characteristics. Material contrasts that can be expected during archaeological prospections are calculated.

The possibilities of prospecting submerged archaeological wooden structures such as shipwrecks using geoelectrics and GPR are analysed in the third paper. For this purpose, the electric resistivity and the dielectric permittivity of wood are determined in relation to the water saturation in a laboratory experiment with "modern" wood pieces and geophysical equipment. Therefore, we use a first assumption that modern water-saturated wood is comparable to unweathered archaeological wood. We distinguish different wood types and anisotropy directions. From these data, contrasts of water-saturated wood to various surrounding materials are calculated and compared with seismic material contrasts. Furthermore, a depth estimation for the detection of wood with GPR and geoelectrics is done.

1.5 Authors' contributions

I (Annika Fediuk) wrote the introduction and conclusion of this thesis (chapters 1, 5 and 6). For the three scientific papers (chapters 2 to 4), I contributed the initial idea, supervised all related measurements and experiments and provided the initial version of the manuscripts. I created all figures (except 4, Figure 4.2) and conducted the analyses with contributions from Tina Wunderlich, Dennis Wilken, Martin Thorwart, Ercan Erkul and Wolfgang Rabbel.

2 The applicability of an inverse Schlumberger array for near-surface targets in shallow water environments

Abstract We investigate the applicability of offshore geoelectrical profiling in the littoral zone, e.g., for archaeological prospection, sediment classification and investigations on coastal ground water upwelling. We performed field measurements with a 20 m long multi-electrode streamer in inverse Schlumberger configuration, which we used to statistically evaluate measurement uncertainty and the reproducibility of offshore electric resistivity tomography. We compared floating and submerged electrodes, as well as stationary and towed measurements. We found out that apparent resistivity values can be determined with an accuracy of 1% to 5% (1σ) depending on the measurement setup under field conditions. Based on these values and focusing on typical metre-scale targets, we used synthetic resistivity models to theoretically investigate the tomographic resolution and depth penetration achievable near-beach underneath a column of brackish water of about 1 m depth. From the analysis, we conclude that offshore geoelectric sounding allows the mapping of archaeological stone settings. The material differentiation of low-porosity rock masses <15% is critical. Submerged wooden objects show a significant resistivity contrast to sand and rocks. Distinguishing brine-saturated sandy sediments from cohesive silty-clayey sediments is difficult due to their equal or reversed resistivity contrasts. Submarine freshwater discharges in sandy aquifers can be localized well, though difficulties may occur if the seafloor encounters massive low-porosity rock masses. As to the measurement setups, submerged and floating electrodes differ in their spatial resolution. Whereas stone settings of 0.5 m to 1 m can still be located with submerged electrodes within the uppermost 4 m underneath the seafloor, they have to be >2 m if floating electrodes are used. Therefore, we recommend using submerged electrodes, especially in archaeological prospection. Littoral geological and hydrogeological mapping is also feasible with floating electrodes in a more time-saving way.

2.1 Introduction

In recent years, various research issues in shallow water environments were investigated by marine electrical resistivity tomography (ERT). The method is sensitive to

lateral and vertical changes in the subsurface electric resistivity and can be used to address materials, especially in extremely shallow water and gassy environments. Investigations include issues such as local groundwater upwelling in coastal areas (Manheim et al., 2004) and geological variations of the subsoil (Okyar et al., 2013; Snyder and Wightman, 2002) as well as metre-scale investigations prospecting archaeological objects, such as wall fundaments or ancient harbor installations (Papadopoulos et al., 2016; Simyrdanis et al., 2018). In a shallow water environment, geoelectric measurements can be performed under excellent coupling conditions due to low water resistivity values and uniformly good contact of the electrodes to the medium. This allows stationary measurements as well as continuously towed measurements. Towed measurements show a faster and denser measurement coverage and therefore enable the survey of larger areas in less time than stationary measurements, whilst the positioning of the measurements is more imprecise (Passaro, 2010). However, the main limitation of the method also results from the low apparent resistivity values of the water, which is reducing the depth penetration (Lagabrielle, 1983).

Several studies investigated different aspects concerning the applicability of marine geoelectrical measurements for different measurement configurations and setups regarding the resolution. Simyrdanis et al. (2015) compare inversion results of synthetic two-dimensional (2D) data for isolated underwater wall fundaments in a homogenous subsurface below a salty water column at 0.5 m to 2 m water depth. They differ between a Dipole–Dipole, Schlumberger and Pole–Dipole configuration as well as between submerged and floating electrodes. They recommend a Pole–Dipole or Schlumberger configuration and did not notice any difference for submerged and floating electrodes up to 1 m water depth. According to the study, objects have to be twice as wide as the electrode spacing to be resolved properly. A priori information, especially about the water depth, improves the results. However, incorrect a priori information can easily falsify the results. Orlando (2013) compare one-dimensional (1D) vertical electric sounding (VES) curves of floating and submerged electrodes for a three-layer case for both Schlumberger and Dipole–Dipole configuration. A higher contrast of the middle layer to its surrounding can be resolved with both setups and configurations more easily, no matter whether the resistivity values are larger or smaller than the surrounding. For small resistivity contrasts, the most feasible setup or configuration changes. Additionally, the study shows VES curves of a Wenner α configuration submerged to the bottom of an approximated shallow water two-layer case, with a maximum sub-bottom resistivity of 10 Ωm . For streamer lengths <20 m and sub-bottom resistivity values >7 Ωm , small uncertainties of the apparent resistivity can induce errors estimating the sub-bottom resistivity. VES curves approximating shallow water two-layer cases are also presented in Kwon et al. (2005) for a Dipole–Dipole configuration. This study also considers that a streamer length >20 m is required in order to be able to resolve resistivity values >7 Ωm in the subsurface, but this in turn influences the spatial resolution. A study to overcome the limitations of deeper water (~ 50 m) is presented in Baumgartner (1996), designing a “fishing rod streamer” which is a vertical Pole–Pole configuration. Mansoor and Slater (2007) calculated sensitivity kernels for various electrode configurations in a homogenous subsurface, e.g., a modified Wenner

α configuration, which is preferable to a Dipole–Dipole configuration regarding depth penetration. They estimated measurement uncertainties by calculating the relative standard deviation of tie points in the measured profiles that include the forward and backward directions. A mean average uncertainty of 3.5% was observed.

Based on all this background, the presented study provides, for the first time, an integrated analysis of all field measurement uncertainty, theoretical spatial resolution of vertical sounding curves and two-dimensional (2D) profiles for two- and three/four-layer geology models, as well as sensitivity analyses for different measurement setups of a marine geoelectric system. We examine the ability of different measurement setups (mobile vs. stationary and floating vs. submerged electrodes) of a multi-electrode streamer of inverse Schlumberger configuration to reconstruct shallow water submarine stratigraphy. This includes:

- i) Repeated measurements of parallel near-shore profiles in about 1 m water depth in different measurement setups to obtain a dataset that enables the statistical inquiry of measurement uncertainties and inversion reproducibility.
- ii) Theoretical considerations based on forward modelling and inverse modelling to estimate the spatial resolution and depth penetration in 1D and 2D resistivity model data.

Following the studies of Simyrdanis et al. (2015) and Orlando (2013), we use field measurement uncertainties to investigate the spatial resolution from layer resistivity and thickness from 1D forward modelling and inversion for different layer models. We provide information about the required streamer length and the depth resolution of layers. Furthermore, the 2D spatial resolution of multiple non-isolated objects below a water column are also considered. The paper starts with the investigation of the measurement accuracy and inversion reproducibility of field data before focusing on synthetic data to investigate the resolution and depth penetration for 1D cases, followed by the investigation of the spatial resolution of a 2D case.

2.2 Methods

2.2.1 Measurement configurations, Field measurements and Investigated Materials

To investigate the applicability of geoelectrical measurements in shallow water environments, a 20 m long multi-electrode streamer was used on test profiles conducted parallel to the Baltic Sea coastline. Due to its short length, it is easy to handle with two persons in about 1 m water depth without using a boat. An inverse Schlumberger configuration was used. The current electrodes C1 and C2 are positioned in the middle of the streamer and the potential electrodes P1a–P1b to P8a–P8b are symmetrically spaced to the sides around the streamer midpoint (Table 2.1, Figure 2.1a). This enables simultaneous measurements on all potential electrode pairs during current injection, meaning that one complete sounding curve of apparent electric resistivity is

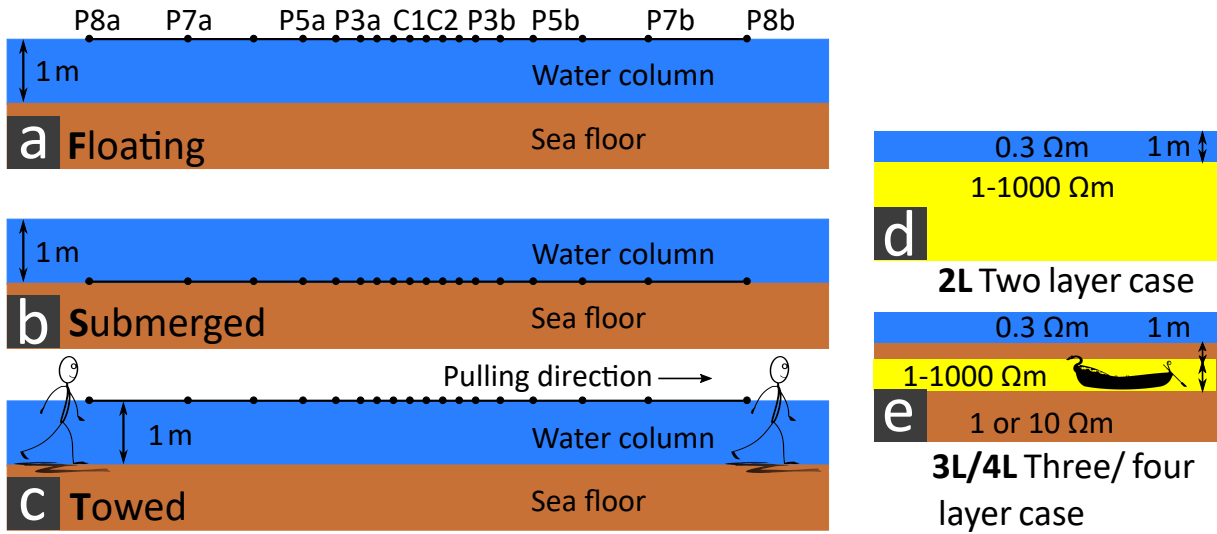


Figure 2.1: Left column: Schematic view of different measurement setups including stationary floating electrodes (setup F, a), stationary submerged electrodes (setup S, b) and towed floating electrodes (setup T, c). Right column: Images of two-layer (2L, d) respectively three-layer cases (3L, e) approximating metre-scale targets. “C” indicates the current electrodes and “P” the potential electrodes of the streamer.

recorded during each measurement cycle. The sounding was performed with RESECS (Resistivity Electrode Control System) multi-channel geoelectric unit and stainless-steel electrodes (see also Figure 2.2b). All equipment was manufactured by the company GeoServe in Kiel, Germany. The following three experimental setups were investigated:

- i) Stationary floating electrodes (Figure 2.1a, setup F)
- ii) Stationary submerged electrodes (Figure 2.1b, setup S)
- iii) Continuously towed floating electrodes (Figure 2.1c, setup T)

For positioning, we used a Leica 1200 Smart Rover RTK-GNSS (manufactured by Leica Geosystems, Heerbrugg, Switzerland). For the towed measurements, streamer coordinates were registered at the front part of the streamer. For the stationary measurements, the coordinates were recorded at the streamer midpoint. A 40 m long test profile was conducted in the Eckernförde Bay, Baltic Sea, Germany (Figure 2.2a), in a distance of 6 m from the shore. The water depth was about 1 m underneath the profile, with the sea bottom dipping 10° from the beach. The resistivity of the brackish water was $0.3 \Omega\text{m}$, measured with a digital conductivity meter GMH 3430 (manufactured by Greisinger, Regenstauf, Germany). The sea bottom consisted of medium sand. To investigate the measurement uncertainty under field conditions, we repeated the measurements 8 times for setup T and 16 times for setup F and S (Figure 2.2b) and tested the reproducibility of the electric tomography with the collected data.

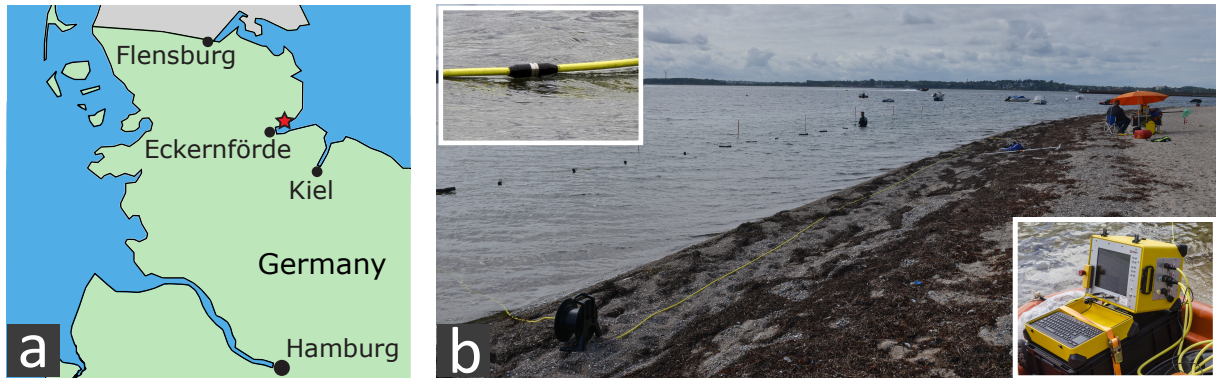


Figure 2.2: a) Location of Eckernförde Bay in Germany, b) Profile using setup F in Eckernförde Bay, Baltic Sea, Germany. Ranging-poles mark the profile of 40 m length in which the 20 m long, inverse Schlumberger multi-electrode streamer is positioned.

Electrode pair	Half electrode layout $L/2$ [m]
C1-C2	± 0.25 m
P1a-P1b	± 0.75 m
P2a-P2b	± 1.25 m
P3a-P3b	± 1.75 m
P4a-P4b	± 2.50 m
P5a-P5b	± 3.50 m
P6a-P6b	± 5.00 m
P7a-P7b	± 7.00 m
P8a-P8b	± 10.00 m

Table 2.1: Inverse Schlumberger configuration used for Eckernförde repetition measurements.

Furthermore, we use modelled datasets of a two-layer (2L) case (Figure 2.1d), representing an integral sea bottom/sediment rock resistivity, and a three- and four-layer (3L/4L) case (Figure 2.1e) representing possible thin layers embedded in the sea bottom, e.g., an archaeological object in the sea floor. The specific resistivity of the water column corresponds to brackish water of the Baltic Sea. For the 2L case, we usually assume a water column of 1 m, which for some investigations we vary from 0.2 m–2 m. The specific resistivity of the second layer was varied from $1 \Omega\text{m}$ – $1000 \Omega\text{m}$. This includes materials such as fully saturated clay and sand (saturation of 1) of about $1 \Omega\text{m}$ (Schön, 1983). Porous, weathered rocks, e.g., limestone, show specific resistivity values of about $100 \Omega\text{m}$, whereas unweathered rocks such as granite are up to $1000 \Omega\text{m}$ (Schön, 1983). Another possible field of application is the upwelling of groundwater below the sea floor. According to Archie’s law (Archie et al., 1942), freshwater-saturated sand shows a specific resistivity of about $100 \Omega\text{m}$.

For the **3L/4L** case, we again define a brackish water column of 1 m. The subsurface shows values of $1\ \Omega\text{m}$ and $10\ \Omega\text{m}$ for this case. A specific resistivity of $10\ \Omega\text{m}$ corresponds to saturated sandy soil (saturation 0.3) (Schön, 1983). A layer of variable thickness, which again shows resistivity values of $1\ \Omega\text{m}$ – $1000\ \Omega\text{m}$, is inserted into the subsurface at variable depths. This range includes possible archaeological stone settings from $100\ \Omega\text{m}$ – $1000\ \Omega\text{m}$ in sandy or clayey environments, depending on the material and weathering. Furthermore, targets such as extended wooden constructions, e.g., shipwrecks, are considered (Figure 2.1e). Fediuk et al. (2020b) determined a specific resistivity of wood of about $210\ \Omega\text{m}$ in fresh water of $21\ \Omega\text{m}$. If this ratio is applied to brackish water, water-saturated wood is about $3\ \Omega\text{m}$ in this case. Both aims shall conclude in the most appropriate measurement setup to resolve the above-mentioned fields of application, including subbottom layers and objects of meter-scale extend issues.

2.2.2 Repeated field measurements

Measurement uncertainty

We repeated the stationary measurements for the floating (**F**) and submerged (**S**) setups 16 times on each position before we moved the cable 1 m to the next point on the profile. Mean values and relative standard deviations were calculated for each position and electrode spacing. The towed measurements (setup **T**) were repeated eight times in both forward and back direction (with and against wind direction) for two measurement cycle lengths of 0.25 s and 0.5 s (see Figure 2.3). The RTK-GNSS (global navigation satellite systems) coordinates were smoothed using a spline interpolation before they were assigned to the streamer midpoint. The profile data was divided into bins, for which again mean values and relative standard deviations were calculated. The inline bin size was chosen to be 30 cm, which corresponds to the streamer displacement during the delay time of 0.8 s between two measurements for an average pulling velocity of $0.4\ \frac{\text{m}}{\text{s}}$. The delay time consists of the longest selectable measurement cycle of 0.5 s (see Figure 2.3) and the internal data storage time of 0.3 s. For a better comparison of setup **T** with setup **S** and **F**, where a measurement was taken each meter, an inline bin size of 1 m for setup **T** was chosen as a second option. We differentiate between five error sources, all of which are dependent on the electrode array distance. Therefore, we will exemplarily focus on the maximum error of the 7th electrode pair with a half potential electrode distance of $L/2 = 7\ \text{m}$.

Noise As it is common for geoelectric instruments, the injected currents and related potential differences are reversed in polarity during one measurement cycle and follow typical rise and decay time functions (Figure 2.3). The recording unit evaluates the quality/noise level within the time intervals of the plateaus of the step functions and accepts or declines a single apparent resistivity value due to a selectable threshold. Single events, such as water waves, contribute to the noise level and are thus recorded by the acquisition unit. We quantify “noise” as the standard deviation of a single mea-

surement within the time intervals of two half cycles (Figure 2.3, yellow line) during a measurement cycle of 0.25 s or 0.5 s (Figure 2.3, red line) from their average value corresponding to the measured resistivity value.

Smearing effects In setup **T**, the continuous movement of the electrode streamer causes a spatial “smearing” of data values along the profile (“inline”) during one cycle. This also affects the standard deviation of the single measurements within the intervals of two half cycles (Figure 2.3, yellow line) and can therefore not be distinguished from noise. Therefore, we do not consider this effect separately. It results in an increased standard deviation for setup **T** and is included in the term “noise”.

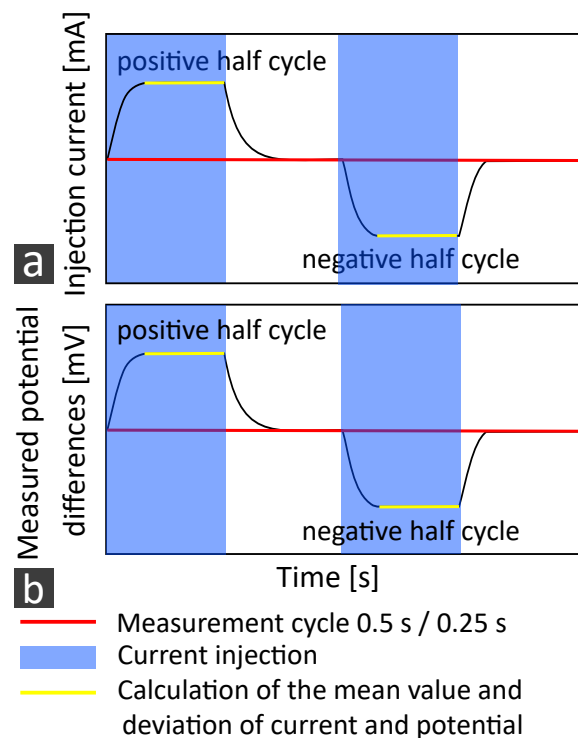


Figure 2.3: Sketch of a geoelectric measurement cycle, showing a) the strength of the injected current and b) the measured potential differences with time within the time window of two half cycles. The red line describes the full length of either 0.5 s or 0.25 s used for the measurements. The blue box highlights the time interval of current injection. The yellow line shows the interval for the calculation of the mean measured value of current and potential, from which the standard deviation is given, defining the measurement noise.

Streamer deflections Uncertainties in apparent resistivity are also caused by deflections of the electrode streamer that result from wind and swell, especially during towed prospections. Streamer deflections change the electrode spacing and, therefore, the geometry factor required for computing the apparent resistivity values. To

estimate this error type, we assume a relative inline displacement $e = 10\text{cm}$ of each streamer end with respect to their midpoint (Figure 2.4). Since the length b of the streamer remains constant, this displacement causes a deflected streamer that we assume to be approximated by the shape of a circle segment, such that the streamer midpoint is displaced by a distance, a , orthogonally from the inline direction. In this geometry, the streamer is an arc segment of length b and its ends are connected inline by a secant of length s . The midpoint displacement a can be calculated using the center angle of the arc α and the circle radius r according to:

$$a = \frac{2 \cdot r - \sqrt{4 \cdot r^2 - s^2}}{2} \quad (2.1)$$

From this, the geometry factor k can be calculated from the symmetrical distance of $f = \overline{C1P7a} = \overline{C2P7b}$ and $g = \overline{C1P7b} = \overline{C2P7a}$ (Figure 2.4) for floating electrodes:

$$k_{floating} = \frac{2\pi}{\left(\frac{1}{f} - \frac{1}{g} - \frac{1}{g} + \frac{1}{f}\right)} \quad (2.2)$$

and for submerged electrodes using the mirror source technique, depending on the water depth t_w :

$$k_{submerged} = \frac{4\pi}{\left(\frac{1}{f} - \frac{1}{g} - \frac{1}{g} + \frac{1}{f} + \frac{1}{h} - \frac{1}{i} - \frac{1}{i} + \frac{1}{h}\right)} \quad (2.3)$$

$$h = \sqrt{(2 \cdot t_w)^2 + \overline{C1P7a}^2} = \sqrt{(2 \cdot t_w)^2 + \overline{C2P7b}^2} \quad (2.4)$$

$$i = \sqrt{(2 \cdot t_w)^2 + \overline{C1P7b}^2} = \sqrt{(2 \cdot t_w)^2 + \overline{C2P7a}^2} \quad (2.5)$$

The uncertainty for the apparent resistivity of an electrode pair results from the difference of the geometry factor for the straight and deflected cable and the arithmetic mean value for the repeated measured current and voltage.

Effective water-level variations There are two effects, which we combine into an “effective water-level variation”. The first one is swell, which displaces the electrodes in the vertical direction, thus changing their distance to the sea bottom. It depends

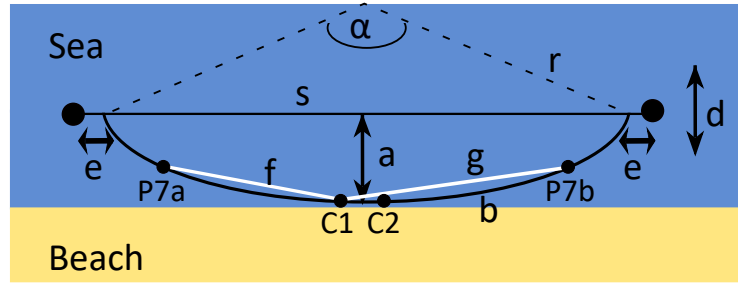


Figure 2.4: Simplified drawing of measurements carried out parallel to the coastline causing a deflected streamer, approximated by the height of a small circle segment. α is the centre angle of the arc, r is the circle radius, b is the length of the streamer, s is the secant, a is the orthogonal displacement from the midpoint, e is the relative in-line displacement. C1 and C2 are the current electrodes, P7a and P7b are the potential electrodes, f is the distance between P7a and C1 respectively P7b and C2, g is the distance between P7a and C2 respectively P7b and C1.

on the speed, lengths and heights of the water waves. The second effect is the possible variation of bathymetry in the crossline direction, which affects the measurements through the varying crossline deflections of the streamer. Quantifying these effects in an exact way would require, besides bathymetry, accurate knowledge of the 3D positions. As this is hardly achievable, we attempt to estimate the order of magnitude of the resulting uncertainties by assuming that they can be modelled by the temporal variation of an “effective water-level”. For this purpose, we compute the apparent resistivity values for a set of two-layer (2L) models. The thickness of the upper layer, identified with the water column of $0.3 \Omega\text{m}$ resistivity, is varied between 0.8 m and 1.2 m in intervals of 10 cm. At an average water depth of 1 m, the curves correspond to an effective water-level variation of ± 10 cm and ± 20 cm. For the bottom layer, resistivity values of $1 \Omega\text{m}$ and $100 \Omega\text{m}$ were chosen. A bottom resistivity of $1 \Omega\text{m}$ corresponds to saturated sand or clay, whereas a bottom resistivity of $100 \Omega\text{m}$ corresponds to saturated limestone (Schön, 1983). In order to estimate the measurement uncertainty for the different setups, an effective water-level variation of 5 cm was assumed for setup S, of 10 cm for setup F and of 20 cm for setup T. The uncertainty is defined to be the difference between apparent resistivity of the average water depth and of the maximum water displacement.

Repeatability of profile locations To complete the considerations on the errors of the three measurement setups (F,S,T), the general positioning uncertainty of the mid streamer point was evaluated in inline and cross-line directions using the data of setup T, which is assumed to have the largest uncertainties in positioning. This was estimated using the deviations of the GNSS (global navigation satellite systems) coordinates from the mean profile track, the possible streamer deflections and the inline “smearing interval length” of data due to the streamer movements during a measure-

ment cycle for setup **T**. The positioning uncertainty provides effective water-level variations in a sloped seafloor, similar to cable deflections, and thus uncertainties in apparent resistivity. They have been summarized above in point (d). In addition, the positioning uncertainty restricts the prospection of laterally limited objects.

Inversion reproducibility

We tested the reproducibility of inversion results from eight repeated profiles in Eckernförde Bay for all three setups. The inversions were carried out with the software RES2DInv (Loke and Barker, 1996). We did not provide a priori information with the inversion for setup **F** and **T**. However, the specification of water depth and water resistivity was required for setup **S**. From the inversion results of eight repetition profiles, mean values and standard deviations were determined for each setup. For setup **T**, an inline data bin size of 1 m was compared to a lower bin size of 30 cm.

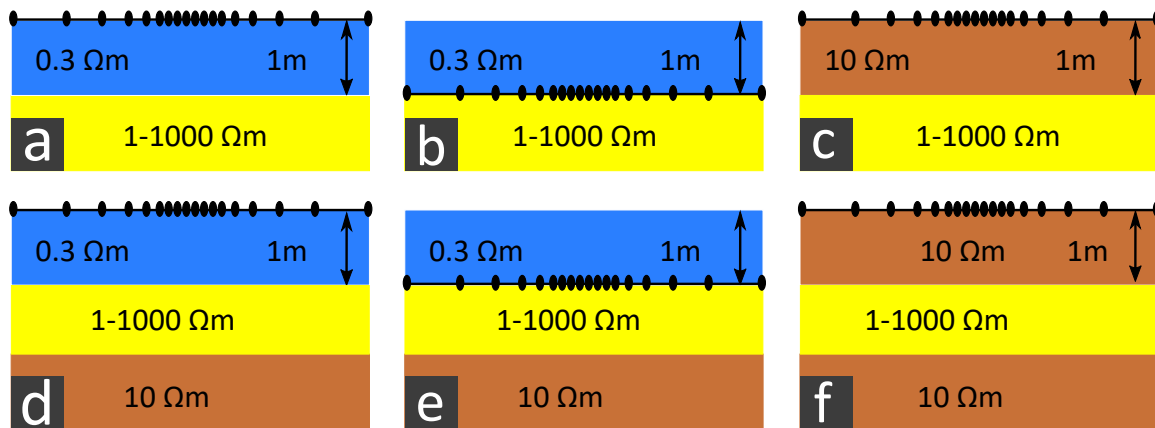


Figure 2.5: Subsurface models used for forward calculations in the 2L case for a) a shallow water environment, setup **F**, b) a shallow water environment, setup **S** and c) an onshore environment, as well as in the 3L case for d) a shallow water environment, setup **F**, e) a shallow water environment, setup **S** and f) an onshore environment.

2.2.3 Resolution of layer thickness and resistivity in 1D media

We investigated the resolution of layer thickness and resistivity for our inverse Schlumberger streamer with different measurement setups based on numerical studies of 1D cases with 2L and 3L/4L models and on field measurement uncertainties. This involved:

- Forward modelling of layered media, to investigate which apparent resistivity values and layer thicknesses can be differentiated due to field measurement inaccuracies in a number of scenarios for setups **F**, **S** and **T**.

- Stochastic inversion of the forward modelled data for setups **F** and **S** to investigate how the results of the forward modelling affect equivalent solutions of layer thickness and resistivity during the inversion.

Forward modelling of layered media

In order to understand the characteristics of geoelectric measurement curves in shallow water, we calculated Schlumberger sounding curves comparing shallow-water and onshore settings. To approximate sediment and rock below a water layer, we have defined three possible **2L** scenarios (Figure 2.5a–c). They correspond to shallow water (Figure 2.5a, b) and to onshore settings (Figure 2.5c). The shallow water settings are based on the **2L** case shown in Figure 2.1, with a brackish water column of 1 m depth and a second layer of material varying from saturated clay to granite. Specific resistivity values from $1 \Omega\text{m}$ – $1000 \Omega\text{m}$ were chosen in irregular steps. Offshore archaeological features are often sanded in shallow depth underneath the seafloor (see also Figure 2.1e). Targets such as wrecks or harbor constructions may extend horizontally over several meters, but much less in depth. This motivated us to make an attempt to assess the arrays' ability to locate this type of target. Therefore, we have defined three **3L** cases (Figure 2.5d–f), again comparing shallow water (Figure 2.5a, b) and onshore settings (Figure 2.5c). Here, we included a 1 m thin sea-bottom layer over a half-space thought to represent an archaeological feature. The third layer satisfies the criteria for moistened sand. In the onshore scenario, the 1 m thick water layer was replaced by moistened sand, and the other layer parameters were kept constant. The measurement configurations selected were setup **F** (Figure 2.5b) and **S** (Figure 2.5c) for shallow water settings. For the onshore settings, electrodes at the surface were used. The formulae for computing theoretical sounding curves were derived for the Schlumberger configuration. However, because of the reciprocity theorem, they also apply to the inverse Schlumberger configuration. They are given in the Appendix 2.6, where floating and submerged electrodes are differentiated. Based on the sounding curves, we followed further considerations to investigate which specific subsurface resistivity values can be resolved based on the measurement uncertainty of the three measurement setups using forward modelling:

- i) We calculated the required streamer length for an inverse Schlumberger configuration to differentiate the specific resistivity of the subsurface from a **2L** case. We distinguished between a shallow water and an onshore scenario, in which the depth of the first layer is varied.
- ii) We defined a **2L** shallow water scenario with a brackish water column of 1 m depth and a subsurface resistivity of $1 \Omega\text{m}$, respectively $10 \Omega\text{m}$. The streamer used for the field measurements in section 2.2.1 was chosen for the measurement configuration. We inserted a layer of variable thickness and resistivity into the homogeneous half-space of the **2L** case at a variable depth, resulting in a **3L** or **4L** case. We investigated the conditions at which the layer can still be differentiated from the homogeneous half-space.

Required streamer length in the 2L case We calculated the required streamer length to differentiate between subsurface resistivity values with a tolerance of 100%. First, we calculated the apparent resistivity for specific resistivity values of 1 Ωm –1000 Ωm as a function of the electrode layout of 1 m–1000 m. Then, we calculated the apparent resistivity values for the doubled resistivity values described above for the same electrode layout. For each streamer length, the apparent resistivity values are subtracted from each other. The required length is reached when this difference is more than three times larger than the field measurement uncertainty, depending on the measurement setup.

Resolution of a layer in the sea bottom (3L/4L case) To determine the resolution of a layer in the sea bottom, we calculated sounding curves for the 3L/4L case within the following ranges: The specific resistivity of the layer ranges from 1 Ωm –1000 Ωm and thickness of the layer is 0.1 m–1.8 m. The depth of the layer is 0 m–10 m below the 1 m deep sea bottom and the specific resistivity of the half-space is 1 Ωm and 10 Ωm . Then, the quotient is calculated from the 3L/4L case with an embedded layer and the 2L case (with a sea bottom resistivity of the half-space). For eight quotients for each measurement curve, the variance with respect to the value 1 is calculated and then a one-sided F-test is done. Thus, 2L and 3L/4L curves can be separated from each other with a probability of 95% if the calculated variance is greater than a multiplied factor (here, 2.1, depending on the degrees of freedom) of the squared measurement accuracy. The measurement accuracy depends on the chosen measurement setup.

Calculation of equivalent model solutions by stochastic inversion by particle swarm optimization

After examining sounding curves, we wanted to investigate to what extent measurement uncertainties affect ambiguities of inversion results. We applied stochastic inversion as a statistical approach to quantify equivalent model solutions within a defined parameter space. For this purpose, we chose the particle swarm optimization method, after Millonas (1994). It was applied to minimize the misfit between modelled sounding curves and our exemplary curve, measured at Eckernförde bay, and to explore the space of suitable models at the same time. Furthermore, interdependencies of the subsurface parameters can be quantified. Here, so-called particles (different models, \vec{m}_t) of a “swarm” (a certain number of models) are randomly chosen and then move through the parameter space searching for minimum misfit solutions within a value range. The moving corresponds to adding a movement vector, \vec{v}_t , to each particle of an iteration step t . The new particle (comprising the subsurface parameters (resistivity ρ_i and thickness h_i , of a layer i)) of iteration $t + 1$ is then

$$\vec{m}_{t+1} = (\rho_1, \rho_2, \dots, h_1, h_2, \dots)_{t+1} = \vec{m}_t + \vec{v}_t \quad (2.6)$$

The search direction \vec{v}_t of each particle consists of a weighted sum of the initial search

direction or search direction of the last iteration, the direction to the individual best solutions of one particle, m_i , as well as the direction to the global optimum solution of the whole swarm, m_g .

$$\vec{v}_t = \omega \vec{v}_{t-1} + c_1 \vec{r}_1 \cdot (\vec{m}_{i,t} - \vec{m}_t) + c_2 \vec{r}_2 \cdot (\vec{m}_g - \vec{m}_t) \quad (2.7)$$

where ω and c_1, c_2 are weighting factor, and \vec{r}_1 and \vec{r}_2 are uniformly distributed random number vectors out of (0,1), that randomize the search direction. The basic particle swarm optimization used here is extended by an option that resets the whole swarm, if stagnation occurs, and a local search algorithm starting at m_g after each swarm movement, following the approach of Wilken and Rabbel (2012). Based on the huge amount of forward calculations done for a particle swarm optimization, an estimate of the probability density function of the model parameters can be determined, enabling to calculate an expected model solution as well as the variance of the model parameters (main diagonal of the covariance matrix). Furthermore, possible trade-offs between model parameters can be investigated (other entries of the covariance matrix) (Wilken and Rabbel, 2012). To apply the method for a geoelectric 2L case, using both setups F and S, we first created 300 random model solutions each consisting of three parameters: the specific resistivity of the first (ρ_1) and second layer (ρ_2) and the depth of the first layer (h_1). The parameter range or search space is defined from the 2L model solution of an exemplary sounding curve recorded from the Eckernförde test profile with setup F using the software IX1D by Interpex. The parameter values are $0.3 \pm 0.29 \Omega\text{m}$ and $80 \pm 79 \Omega\text{m}$ for the resistivity values of the first and second layers, and $0.9 \pm 0.5 \text{m}$ for the depth of the first layer. The method was also applied for a 3L case for setup F and S, for which again 300 random model solutions were created consisting of five parameters: the specific resistivity of the first (ρ_1), second (ρ_2) and third layer (ρ_3), as well as the first and second layer thickness (h_1 and h_2). Here, the parameter range corresponds to that of the 2L case, extended by a third layer. It is defined by $0.3 \pm 0.29 \Omega\text{m}$, $80 \pm 79 \Omega\text{m}$ and $10 \pm 9 \Omega\text{m}$ for the resistivity values of the first, second and third layers respectively, and $0.9 \pm 0.8 \text{m}$ for the layer thicknesses. To enable the swarm to leave local minima, the swarm is randomly redistributed after 25 iterations if the global misfit change is $< 6 \cdot 10^{-5}$. In total, the misfit values of 1800 models of the first six iterations are used to calculate the probability density function. The variance of each model parameter is defined as the square of the covariance matrix. A normalized correlation matrix was calculated from the covariance matrix to identify possible correlations of the subsurface parameters.

2.2.4 Spatial resolution in 2D media

To investigate the spatial resolution of 2D applications below the sea bottom, we applied two approaches:

- Calculate sensitivity kernels for setup F, S under consideration of the water column.

- Perform checkerboard tests for setup **F, S**.

Sensitivity kernels

The sensitivity kernel describes the effect of a single point-shaped resistivity anomaly on the potential or measured potential difference for a given electrode geometry. It depends on the relative positions of the anomalies and electrodes, the resistivity distribution of the background and the anomaly contrast to this background. Loke and Barker (1996) considered the potential of an electric monopole, at which a unit-current (1 A) is fed into a homogeneous half-space. They showed that the change δV of the potential V at an observer position caused by an anomalous resistivity volume Φ can be calculated by:

$$\delta V = \frac{\delta \rho}{\rho^2} \int_{\Phi} \nabla V \cdot \nabla V' d\tau \quad (2.8)$$

where ρ is the background resistivity, $\delta \rho$ is the resistivity difference of the anomalous volume with respect to the background and V' is the “adjoint potential” of an electric monopole placed at the observer position. Considering a 2D medium with electrode and anomaly placement in the x-z-plane, the sensitivity kernel for the monopole potential is:

$$F_C(x, z) = \rho^2 \frac{\delta V}{\delta \rho} \quad (2.9)$$

The sensitivity kernel for the Schlumberger array is then the summation of the four combinations between current electrodes C1 and C2 and the exemplary chosen potential electrodes P1a and P1b:

$$F_{Schlum}(x, z) = F_{C1P1a} - F_{C1P1b} - F_{C2P1a} + F_{C2P1b} \quad (2.10)$$

For electrodes at the surface, the potential V can be calculated by using the half-space formulas (see Appendix 2.7). For submerged electrodes, the full-space formulas for the potential V (see Appendix 2.7) and the mirror source technique have to be used:

$$F_{sub, C1P1a} = F_{C1P1a, full} + F_{C1P1a, mirror} \quad (2.11)$$

Sensitivity kernels were calculated for a water layer of 1 m depth and 0.3 Ωm over a half-space media of 10 Ωm by equation 2.8).

Checkerboard tests

After calculating the 2D sensitivity kernels for our inverse Schlumberger streamer, we used synthetic data to verify the results. In Simyrdanis et al. (2015), numerous investigations on isolated objects in a homogeneous half-space have already been done.

We are particularly interested in the spatial resolution of multiple small-scaled objects, that are aligned in both lateral and vertical direction, and in the resulting limitations of the different measurement setups. For this purpose, a checkerboard test is useful, where numerous objects are located with vertical and lateral distance. We distinguished between three synthetic subsurface models of 30 m length and 4 m depth, approximating both onshore and shallow water scenarios. The checkerboard pattern consists of 1 m×1 m large bodies with alternating resistivity values of 1 Ωm and 10 Ωm in the sub-bottom. These values correspond to typical contrasts in the subsurface, such as wet sand to weathered rock. They are well-resolvable using our inverse Schlumberger streamer in the 1D case, so that the focus can be set on the 2D resolution. An additional water column of 1 m depth and 0.3 Ωm was implemented for the shallow water case. Again, setups **F** and **S** were compared using a 20 m Schlumberger array. As the forward modelling was performed with the software RES2DMOD (Loke, 2002), we used an equal electrode distance of 1 m. Nevertheless, this is comparable to our array due to the same streamer length and a similar minimum electrode spacing. The horizontal and vertical cell spacing was 0.25 m and 0.5 m. Noise of 1% and 2% was added to the data for the measurement setup **S** and **F**. The inversion was done with the software RES2DInv (Loke and Barker, 1996). In cases where the checkerboard test could not provide a spatial separation between the objects, the object arrangement was varied (i.e., using no vertically arranged objects, an increased object size or a larger lateral object spacing) to investigate the possibilities of each measurement setup.

2.3 Results

2.3.1 Repeated field measurements

In the following sections, results of the repeated field measurements are presented. First, the measurement uncertainties are shown before focusing on the reproducibility of 2D inversion results.

Measurement uncertainty

The measurement errors from the 2D repeated measurement profile for setups **S**, **F** and **T** are shown in Figure 2.6 and in Tables 2.2 and 2.3. Figure 2.6a–c show pseudo sections of arithmetically averaged apparent resistivity values from repeated measurements for eight pairs of electrodes (y-axis) and 40 positions along the profile (x-axis). The apparent resistivity values increase with larger electrode spacing, indicating the transition from the water column to the sea-bottom. The pseudo sections of all three setups are compatible, showing apparent resistivity values of 0.5 Ωm–4 Ωm. The apparent resistivity values of setup **S** are slightly higher due to the proximity of the electrodes to the sea floor. The relative (1σ) standard deviations occurring for each electrode layout and profile position are displayed in Figure 2.6d–f. The maximum uncertainties are of the order of 1% for the static measurements and a few percent for the moving system. In particular, we found the stationary setups **S** and **F** showing

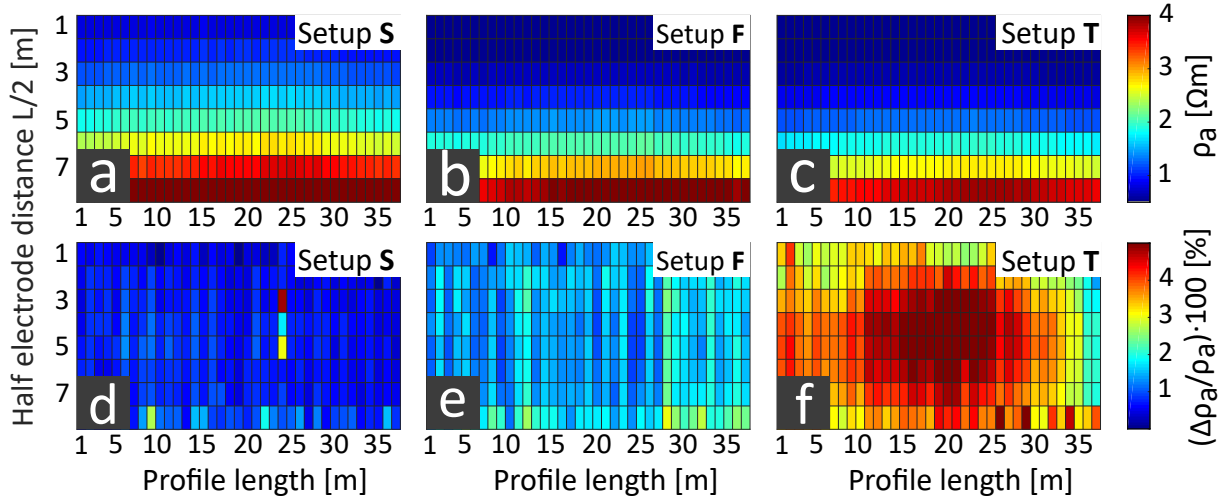


Figure 2.6: Comparison of mean values a)-c) and relative standard deviations d)-f) from repeated measurements for eight electrode pairs (y-axis) along the profile (x-axis). Left column: setup **S** (submerged), centre column: setup **F** (floating), right column: setup **T** (towed).

average uncertainties of $<0.8\%$ and $<1.5\%$ respectively, whereas the moving setup **T** showed uncertainties $<5\%$. The values are given numerically in Table 2.2. The uncertainties increase with depth for stationary measurements. Noticeable are disturbances affecting all electrode pairs at particular profile positions. Setup **T** shows the largest uncertainties for the fourth to sixth electrode pair

in the middle of the measurement profile. Table 2.2 also summarizes further investigations of the setup **T** regarding a possible impact of various measurement cycle lengths of 0.25 s and 0.5 s (see Figure 2.3), of the chosen inline bin sizes of 30 cm and 1 m respectively, and of the towing direction with or against the wind on the measurement uncertainties. None of the aspects have a significant influence on the occurring uncertainties. However, a short measurement cycle of 0.25 s for towed measurements is rather obstructive, whereas setup **F** is not dependent on the measurement cycle (Table 2.3).

In the next step, we investigated possible uncertainty sources. Table 2.4 summarizes three assumed error components for the exemplary electrode pair P7a–P7b, with $L/2 = 7$ m for all measurement setups. The noise was derived from the field measurements, whereas deviations due to streamer deflections and water-level variations were theoretically estimated. With relative uncertainties of approximately 1%, 2% and 5% for setup **S**, **F** and **T**, the noise is equal to the average measurement accuracy for the electrode pair P7a–P7b. Thus, for larger electrode layouts, we assume that other sources of error will only contribute to the maximum recorded uncertainties. For the shortest layouts ($L/2 = 0.75$ m), as an example, the noise for setup **F** is 0.3%, so that other sources of error are more evident here. Figure 2.7 compares measurement uncertainties of setup **F** from field data shown in Figure 2.6 and Table 2.2, with theoretical uncertainty calculations based on estimations made in section 2.2.2,

Measurement Configuration	Rel. stand. Deviation (1σ)
Setup F	0.8% ($L/2 = 10$ m)
Setup S	1.4% ($L/2 = 10$ m)
Setup T, 1 m bins	
With wind, measurement cycle 0.25 s	3.7% ($L/2 = 2.5$ m)
Setup T, 30 cm bins	
With wind, measurement cycle 0.25 s	4.3% ($L/2 = 2.5$ m)
Setup T, 30 cm bins	
With wind, measurement cycle 0.25 s	4.3% ($L/2 = 2.5$ m)
Setup T, 1 m bins	
Against wind, measurement cycle 0.25 s	4.2% ($L/2 = 2.5$ m)
Setup T, 1 m bins	
Both directions, measurement cycle 0.25 s	5.4% ($L/2 = 2.5$ m)
Setup T, 1 m bins	
With wind, measurement cycle 0.5 s	3.1% ($L/2 = 2.5$ m)
Setup T, 1 m bins	
Both directions, measurement cycle 0.5 s	3.5% ($L/2 = 2.5$ m)

Table 2.2: Summary of relative standard deviations for different measurement setups arithmetically averaged from 40 measurement positions for the most affected electrode layout ($L/2$ [m], see Table 2.1). Additional aspects such as the bin size, the towing direction depending on the wind and the measurement cycle length are listed.

Measurement Cycle	Rel. stand. Deviation (1σ)
1 s	2.2%
0.5 s	1.3%
0.25 s	1.4%
0.2 s	1.1%

Table 2.3: Relative standard deviations (1σ) for various measurement cycles of setup F. The values are determined from a single measurement position for an electrode layout of $L/2 = 10$ m.

Setup	Noise and smearing	Streamer deflections	Water level variations	Total error
Setup S	0.03 Ω m (1%)	0.04 Ω m (1%)	0.15 Ω m (5%)	0.22 Ω m (7%)
Setup F	0.07 Ω m (2%)	0.04 Ω m (1%)	0.3 Ω m (11%)	0.41 Ω m (14%)
Setup T	0.12 Ω m (4%)	0.04 Ω m (1%)	0.45 Ω m (16%)	1.61 Ω m (21%)

Table 2.4: Measurement errors resulting from noise, streamer deflections and water-level variations are estimated for an electrode of $L/2 = 7$ m and compared among the measurement setups.

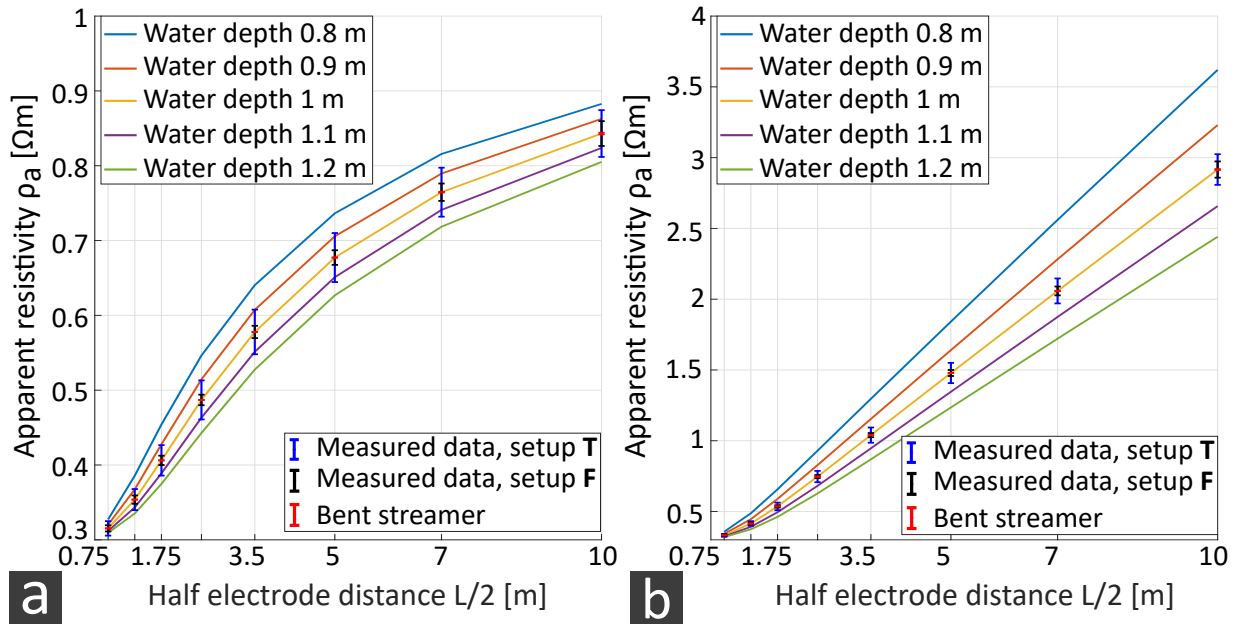


Figure 2.7: Sounding curves of a 2L case for various water depths (coloured curves) and a first layer resistivity of $0.3 \Omega\text{m}$ and a second layer resistivity of a) $1 \Omega\text{m}$ and b) $100 \Omega\text{m}$. Errors of setup T (blue error bars), setup F (red error bars) and streamer deflections (black error bars) from Eckernförde Bay repetition measurements are added.

including water-level variations and streamer deflections. The effective water-level variations are shown by colored vertical electrode sounding (VES) curves and appear to affect the apparent resistivity values more than streamer deflections (Figure 2.7, red error bar, relative errors of 2%). The influence of water-level variations on the apparent resistivity increases with increasing subsurface layer resistivity (compare Figure 2.7a, computed for $1 \Omega\text{m}$, and Figure 2.7b for $100 \Omega\text{m}$). Measurement uncertainties obtained from the repeated profiling with setup T (Figure 2.7, black error bar) are within the range of effective water-level variations of 10 cm for a subsurface resistivity of $1 \Omega\text{m}$, and uncertainties of stationary measurements (Figure 2.7, blue error bar) are even smaller. Compared to the calculated water-level variations on a subsurface resistivity of $100 \Omega\text{m}$, the measured uncertainties are of little weight. Thus, we assume that water-level changes occur locally and do not change the total water column, as considered in the calculation. On the contrary, for resistivity values $\sim 1 \Omega\text{m}$, the height of the water column might be incorrectly determined by ± 10 cm due to measurement uncertainties. Since Table 2.4 includes the maximum possible impact of water-level variations and cable deflections, the estimated measurement uncertainties are significantly higher than the observed uncertainties. As observed with the repeated field measurements, setup T shows the largest uncertainties followed by setup F and setup S.

To conclude the section, the repeatability of profile locations of setup T was evaluated in inline and cross-line directions. The maximum inline position deviation of ± 50 cm

results from “smearing effects” of ± 30 cm and from errors due to streamer deflections of ± 10 cm. A histogram of crossline GNSS coordinate deviations, d , from the mean profile track (see also Figure 2.3) is shown in Figure 2.8. The cross-line profile track error of 50 cm was defined as twice the standard deviation and complemented by cross-line streamer deflection deviations of ± 1 m for the fourth electrode pair of $L/2 = 2.50$ m (see also Figure 2.4). This results in a maximum error of ± 1.50 m within the cross-line direction. Within this range, we expect measurement errors due to water-level variations or smearing of the apparent resistivity caused by a possible 3D distortion of target locations.

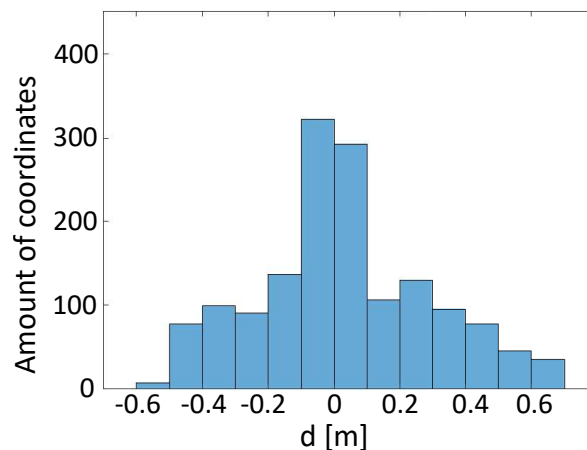


Figure 2.8: Histogram of GNSS (global navigation satellite systems) coordinate deviations d , of all towed profiles from the average measurement profile calculated from a regression curve of the coordinates.

Inversion reproducibility

After investigating the repeatability of measurement values of a profile and possible sources of uncertainties, the reproducibility of 2D inversions of the same profile is considered. In Figure 2.9a–c, the arithmetical average of eight individual inversion results from the repetition profiles are compared for setup **S** (Figure 2.9a), setup **F** (Figure 2.9b) and setup **T** (Figure 2.9c). In general, the average inversion results of setup **S**, **F** and **T** are similar with regard to the water resistivity, water depth and lateral resistivity distribution in the subbottom, showing a lateral trend from low resistivity values of $50 \Omega\text{m}$ at the left profile side to resistivity values of $>150 \Omega\text{m}$ at the right profile side. The water column corresponds to the onsite measurements regarding depth and resistivity. For setup **S**, slightly higher values of the water and subbottom resistivity were observed. In Figure 2.9d–f, the relative standard deviations of the inversion results are compared for the three setups. The water column is well reproduced with all setups, showing deviations $<5\%$. The reproducibility of subsurface resistivity values is almost comparable to those of the water column with deviations $<10\%$ for setup **F**. In comparison, setup **T** shows increased relative standard deviations of $>10\%$ in the subsurface. Setup **S** shows local deviations of $>20\%$.

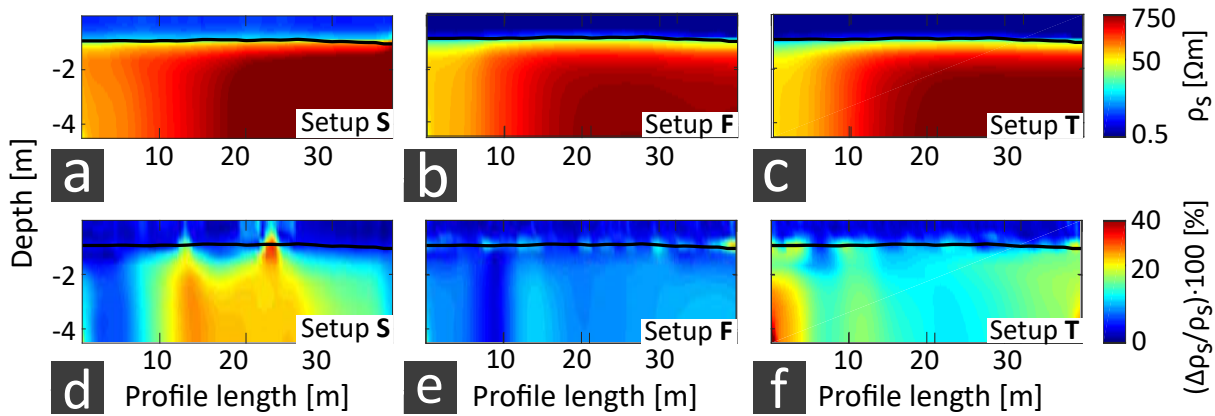


Figure 2.9: Comparative plotting of arithmetical average values (a-c) and relative standard deviations (d-f) of eight 2D inversion results calculated from repetition profiles of Eckernförde Bay with the software RES2DInv. a), d) setup S (submerged), b), e) setup F (floating) and c), f) setup T (towed).

2.3.2 Resolution of layer thickness and resistivity in 1D media

Forward modelling of layered media

We investigated the spatial resolution of our Schlumberger array (largest half electrode distance, $L/2 = 10\text{m}$, see Table 2.1) by comparing the theoretical sounding curves of possible onshore and shallow water environments for different layering of 2L and 3L cases (Figure 2.10). We then focused on a 2L case, where we basically investigated the influence of varying sea-bottom resistivity and water depths for the three setups on the required streamer length. Then, we turned to a 3L/4L case where we investigated the resolution ability of the setups with respect to a layer in a homogenous sea-bottom thought to represent an archaeological feature.

Sounding curves for the 2L and 3L case

As shown in Figure 2.10, for the shallow water 2L scenarios, the variation span of apparent resistivity due to sea-bottom resistivity is reduced by a factor of 100 compared to the variation of “true” sea-bottom resistivity within the observation window of the streamer system (red boxes in Figure 2.9). In a first assumption of the measurement uncertainties, all setups are able to distinguish between sea bottom resistivity values in the range of $1\ \Omega\text{m}$ – $10\ \Omega\text{m}$. However, sea-bottom resistivity values of $>10\ \Omega\text{m}$ appear to be almost undistinguishable. The main difference between the setups S and F is visible for array lengths $<5\text{m}$ and for subsurface resistivity values $<5\ \Omega\text{m}$. In this case, setup S shows apparent resistivity values of a full-space environment. This is different for the onshore case (Figure 2.10c), where the higher resistivity of the surface layer enables a differentiation of bottom-layer resistivity values according to first estimates in the range of $1\ \Omega\text{m}$ – $200\ \Omega\text{m}$, given the same uncertainties and spread lengths as in the shallow water case. Indeed, the ratio of the resistivity of the top layer to the maximum resolvable resistivity of the bottom layer is in both cases about the same (about 0.5%) and approximately equal to the measurement uncertainty. In the 3L case, for

specific resistivity values of the middle layer of $1\ \Omega\text{m}$ – $1000\ \Omega\text{m}$, the resulting range of apparent resistivity values is 70 times higher in the onshore scenario ($4\ \Omega\text{m}$ – $70\ \Omega\text{m}$, Figure 2.10c) than in the shallow water scenario ($2.1\ \Omega\text{m}$ – $3\ \Omega\text{m}$, Figure 2.10a, b) for our streamer length. The maxima of the **3L** sounding curves are far out of the streamer length for the shallow water scenario. Therefore, **2L** and **3L** sounding curves are quite similar, depending on the subsurface. This issue is discussed in detail in the section below. The difference of setup **S** (Figure 2.10e) and setup **F** (Figure 2.10d) in the shallow water scenario is again visible for small array lengths $< 2\ \text{m}$ and low subsurface resistivity values $< 5\ \Omega\text{m}$.

Required streamer length in the 2L case

Figure 2.11 shows the required streamer length to resolve the specific resistivity of the subsurface in a shallow water **2L** case with a tolerance of 100% considering the measurement uncertainty. Variations of the water column from $0.2\ \text{m}$ – $2\ \text{m}$ and the differences of the setups **S**, **F** and **T** were evaluated. There is a significant difference between the shallow water scenario (Figure 2.11a–c) and the onshore scenario (Figure 2.11d). In the onshore scenario, specific resistivity values $> 100\ \Omega\text{m}$ with a surface layer thickness up to $2\ \text{m}$ can be resolved with our electrode array of $20\ \text{m}$ length. In the shallow water scenario, a specific resistivity of about $10\ \Omega\text{m}$ can be well resolved in water depths depending on the measurement setup ($0.4\ \text{m}$ – $2\ \text{m}$). The required streamer length increases with increasing resistivity contrast from the bottom to the top layer. In the onshore scenario, this increase can be observed from a specific resistivity of $10\ \Omega\text{m}$. In contrast, due to the top layer of $10\ \Omega\text{m}$, for specific resistivity values of $1\ \Omega\text{m}$ – $10\ \Omega\text{m}$, there is a little decrease in the required streamer length. Furthermore, for the shallow water scenarios, setup **S** can resolve a specific resistivity that is seven times lower than setup **T** for an equal streamer length and water depth. A duplication of the water depth requires twice the streamer length in order to resolve the same specific resistivity values.

Resolution of a layer in the sea-bottom (3L/4L case)

Figure 2.12 shows the required parameters to differentiate an embedded layer from the surrounding sea-bottom. A brackish water column of $1\ \text{m}$ was used to calculate the maximum depth in which variable layer resistivity values and thicknesses can be resolved due to the measurement uncertainties. For all measurement setups and layer resistivity values, the relation between the layer thickness and its maximum resolvable depth can be described by limited growth functions. For setup **S** and **F**, the maximum layer depth is not reached at any investigated layer resistivity and thickness in a sea-bottom of $1\ \Omega\text{m}$. For setup **T**, this applies to resistivity values larger than $200\ \Omega\text{m}$. The maximum detection threshold of approximately $8\ \text{m}$ depth is reached from a layer thickness of $0.5\ \text{m}$ (Figure 2.12b). Setup **S** shows the lowest measurement uncertainty. Here, resistivity values $> 20\ \Omega\text{m}$ can be resolved for layer thicknesses $> 0.5\ \text{m}$ in more than $10\ \text{m}$ depth below the sea-bottom (Figure 2.12a). For setup **F**, this applies to resistivity values $> 100\ \Omega\text{m}$ (Figure 2.12c). For a sea-bottom of $10\ \Omega\text{m}$, the limited growth curves for specific resistivity values of $50\ \Omega\text{m}$ – $100\ \Omega\text{m}$ and $2\ \Omega\text{m}$ – $5\ \Omega\text{m}$ are in the same range (Figure 2.12d). Here, comparable layer thicknesses and layer depths can be resolved. From all investigations, the lowest depth resolution is reached here,

which is due to the lower contrast of the layer resistivity values to the sea floor.

Calculation of equivalent model solutions by stochastic inversion using particle swarm optimization

In the last section, we have shown that in shallow water environments, the sounding curves of an inverse Schlumberger configuration for both 2L and 3L/4L cases with varying specific resistivity values in the sea-bottom are close to each other. Due to measurement uncertainties for each setup, specific resistivity values in the subsurface cannot be properly differentiated. Consequently, ambiguities will occur during the inversion. In this paragraph, we focus on the question of how significant these ambiguities are. For this purpose, we analyzed two exemplary 2L and 3L models. The 2L model is based on the 1D inversion result of a measurement curve taken from the profile of Eckernförde Bay. There is a water layer of $0.3 \Omega\text{m}$ and 0.9m depth, as well as a sediment resistivity of $80 \Omega\text{m}$. For the 3L case, we have assumed a second layer of 90cm and $80 \Omega\text{m}$, as well as a half-space resistivity of $10 \Omega\text{m}$. The measurement uncertainties of the setups S and T were used to weight the inversion solutions.

Resolution of sediments below the water column (2L case)

In the stochastic inversion, six iteration steps were stored for each model. From the pool of all solutions, those with a relative deviation of $<14\%$ to the reference model were selected to be shown in Figure 2.13a for a better visualization of the inversion ambiguities for setup F. The particular least-square misfit of the model solutions to the true model (black line) is color-coded, and the maximum relative misfit of 14% was normalized to 1. There are slight ambiguities in ρ_1 and h_1 and a wider range of ambiguities in ρ_2 . These observations can also be quantified by statistical analysis. Table 2.5 summarizes the expected model (see also Figure 2.13a, white dashed line) and its variance of the subsurface parameters. It becomes apparent that the method is sensitive to the resolution of the water column. In the sea-bottom, on the other hand, limitations of the method have to be accepted if the array length is not increased. Furthermore, the correlations of the subsurface parameters can be derived from the statistical analysis. Figure 2.13b shows the normalized correlation matrix of the subsurface parameters of the 2L case for setup F. The main diagonal of the pattern shows the correlation of the parameters with themselves (variances). The remaining pattern describes the correlation coefficients between the subsurface parameters. A large correlation coefficient causes a high dependence of a subsurface parameter on another in the inversion result. In the 2L case, the parameters ρ_1 and h_1 show this dependence. The correlations offer chances to improve inversion ambiguities by providing information on a parameter (e.g., the water depth) during the inversion. The unambiguous solution of the other parameter (e.g., the water resistivity) is derived from this. However, it also includes risks in the case that erroneous information is given for a parameter in the inversion. An erroneous specification of the water depth results in an incorrect water resistivity. If incorrect a priori information on both water resistivity and depth is given, this will have an impact on the sea-bottom resistivity. In a 2L case, setup S shows the same results as setup F with regard to both ambiguities and correlation coefficients.

	2L case, setup F	2L case, setup S	3L case, setup F	3L case, setup S
h_1	0.9 ± 0.09 m 10.4%	0.9 ± 0.1 m 10.6%	0.9 ± 0.14 m 14.8%	0.92 ± 0.14 m 14.76%
h_2	-	-	1.8 ± 0.41 m 22.8%	1.88 ± 0.41 m 21.51%
ρ_1	0.3 ± 0.04 Ω m 14.6%	0.3 ± 0.04 Ω m 14.7%	0.3 ± 0.05 Ω m 15%	0.3 ± 0.05 Ω m 15.1%
ρ_2	78.3 ± 25 Ω m 31.9%	83 ± 31.3 Ω m 37.7%	85.1 ± 28.4 Ω m 33.3%	76.9 ± 37.54 Ω m 48.8%
ρ_3	-	-	12.3 ± 3 Ω m 24.5%	11.9 ± 3.9 Ω m 32.8%

Table 2.5: Expected model and variance calculated from all models saved during the stochastic inversion using six iteration steps. The subsurface parameters layer thickness h_i and resistivity ρ_i are distinguished for the 2L and 3L case as well as for setup F and setup S.

Resolution of a layer in the sea-bottom (3L case)

The analysis of inversion ambiguities in the 2L case was also applied to the 3L case for setup S and F (Figure 2.13c, d). The results for the 2L and 3L case show parallels and again, the setups hardly differ. The three additional subsurface parameters enlarge the range of possible inversion solutions, and due to measurement uncertainties, the equivalence principle applies. The water column is also best reproducible with <15% variance. For all sea-bottom parameters, there are the same restrictions as in the 2L case, with >20% variance. In addition to ρ_1 and h_1 , the parameters h_1 and h_2 , as well as ρ_2 and ρ_3 , also correlate with each other. The correlations provide additional options to limit inversion ambiguities. The resistivity of the second layer can also be restricted in case the resistivity of the homogeneous half-space in the area surrounding the prospected objects is known. In contrast to the 2L case, the water depth directly influences the thickness of the second layer. Consequently, erroneous a priori information on the water depth has an increased impact on the sea-bottom.

2.3.3 Spatial resolution in 2D media

In the previous sections, we have investigated the resolution of layer thickness and resistivity for 1D sounding curves by forward modelling and stochastic inversion. The next step is to focus on the resolution of objects with defined lateral dimensions in 2D measurements for the three measurement setups. Therefore, the sensitivity kernels of the streamer configuration were calculated and inversion results from synthetic data approximating numerous objects were evaluated.

Sensitivity kernels

Sensitivity kernels are dependent on the electrode configuration and show a sequence of positive and negative sensitivity areas, from which conclusions can be drawn about the spatial resolution of subsurface targets. The 2D sensitivity kernels of our inverse Schlumberger array in a water column of 1 m depth and $0.3 \Omega\text{m}$ above a seabottom resistivity of $10 \Omega\text{m}$ are compared for setup **F** (Figure 2.14a) and setup **S** (Figure 2.14b). Both setups show a typical Schlumberger sensitivity pattern with its sequence of positive and negative sensitivity values in lateral direction and the change of positive sensitivity values in vertical direction, that describes the good compromise of vertical and lateral resolution of the method. However, for setup **F**, the lateral highly sensitive area of the array (see black frames in Figure 2.12) is found within the water column. At the seafloor, the sensitivity values remain slightly positive for half array lengths $<L/2 = 3.5 \text{ m}$. It is only half array lengths $>L/2 = 5 \text{ m}$ that show low negative sensitivity values in the sea-bottom. For setup **S**, the sensitivity kernels adapt to a full-space environment with a negligible influence from the sea surface boundary. This is noticeable by the pattern around the potential electrodes being minimally orientated towards the sea surface. The sensitivity values of setup **S** are also in accordance with those of setup **F**. However, the sequence of positive and negative sensitivity values can be observed in the water column as well as in the seafloor. In addition, at the seafloor, the width of the positive sensitivity cone in the middle of the array is different for the two setups: It is 2 m for setup **F** and 0.5 m for setup **S**. However, the maximum depth of the positive sensitivity cone in the middle of the streamer for a half array length of $L/2 = 10 \text{ m}$ differs only slightly for the two setups. It is about 4 m from the sea surface and provides a first estimation of the depth penetration of the array. The alternating positive and negative sensitivity areas in the sea-bottom for setup **S** is essential for a sufficient resolution of objects, including their specific resistivity and dimensions. Thus, setup **S** is superior to setup **F**, especially in the resolution of small-scale objects or the differentiation of numerous laterally separated objects. The positive sensitivity area of setup **F** in the sea-bottom ensures that objects of a certain size can be resolved. However, in case of small object dimensions and large resistivity contrast from object to the surrounding seafloor, blurring has to be expected. The smallest width of objects that can be resolved by setup **S** and **F** is estimated to be about 0.5 m and 2 m from the lateral extent of the positive sensitivity cones at the seafloor. Thus, with a brackish water column of 1 m, the difference in the lateral resolution of objects below the seafloor is a factor of four among the setups.

Checkerboard tests

After evaluating the sensitivity of the array, we investigated the spatial resolution of multiple objects laterally and vertically arranged in detail using synthetic data. Figure 2.15 combines the results of the checkerboard tests for an onshore environment (Figure 2.15a) and for a shallow water environment for setup **S** (Figure 2.15b) and setup **F** (Figure 2.15c,d). Looking at Figure 2.15a in detail, the top row of the checkerboard pattern is resolved properly and the subsurface resistivity values of $1 \Omega\text{m}$ and $10 \Omega\text{m}$

are reproduced correctly, whereas the second row's pattern is blurred and a half-space resistivity value of $3 \Omega\text{m}$ is reached. Thus, objects underlying other structures at the surface are hidden, as the second row of the checkerboard pattern can be resolved when the first row is removed. The checkerboard tests approximating a shallow water environment show different results. For setup **S**, the top row of the checkerboard pattern can still be resolved, although the objects become slightly blurred due to the water column. Additionally, the resistivity values are reduced compared to the original pattern. The inversion results show resistivity values of $0.5 \Omega\text{m}$ and $5 \Omega\text{m}$ above a half-space resistivity of $1 \Omega\text{m}$. Setup **F** cannot reproduce the checkerboard pattern but shows a horizontally blurred stripe of increased resistivity of $3 \Omega\text{m}$, which indicates the pattern of the first row. Below that, the resistivity values decrease. Based on the results, we modified the checkerboard pattern for this setup and found that vertically arranged objects generally have a significant negative effect on the results. In this case, a minimum object size of $2 \text{ m} \times 2 \text{ m}$ and a lateral distance of more than 2 m is required for the separation of objects. Figure 2.15d shows an exemplary object of this size with a lateral separation of 4 m . To resolve numerous objects in the sea-bottom, an increased lateral distance between them is required.

2.4 Discussion

Based on the results, we discuss the applicability of our inverse Schlumberger streamer with regard to measurement uncertainty, spatial resolution, depth penetration and inversion ambiguity. We also discuss the most suitable measurement setup.

2.4.1 Repeated Field Measurements

Discussing the measurement uncertainty of different setups, setup **S** shows the highest reproducibility due to its fixed electrode positions on the seafloor, from which they are largely independent of sea surface waves. For setup **F**, wind, swell and short periodical waves are of greater importance. Setup **T** is affected by streamer deflections (Figure 2.4) and possible resulting water-level variations, which cannot be avoided during the continuous walk along the profile. Furthermore, inline "smearing" effects that occur from a towed streamer movement during a measurement cycle result in higher errors of $<5\%$ (1σ) compared to the other setups. A similar measurement error of 3.5% (1σ) was observed in Mansoor and Slater (2007) for a modified Schlumberger streamer, which also had a length of 20 m . Setup **S** and **F** show the highest relative errors for large electrode layouts. This is because the electrodes resolving the heterogeneous sea bottom cause larger errors than the electrodes resolving small resistivity variations of the water column. Additionally, the measured potential decreases with increasing array length, amplifying noise. However, stationary repeated measurements also show deviations equally affecting all electrode pairs at one profile position. This can be explained by waves from passing ships that occur sparsely along the surf zone. A surprising feature is that for setup **T**, the largest measurement errors were recorded

for the middle electrode lengths, which is due to the measurement procedure parallel to the coastline (Figure 2.4). Two persons keep the measurement streamer in track at both ends, whereas the middle of the streamer is hardly manageable and deflects towards the beach, affecting the middle electrode pairs imaging the transition from water column to the sea bottom. As the sea floor slopes down 8.5° towards the sea, the water depth changes, about $15 \frac{\text{cm}}{\text{m}}$ perpendicular to the beach, which results in the largest uncertainties for the middle electrode pairs. The high measurement uncertainties in the middle of the profile are because, at the profile beginnings in forward and backward directions, the streamer was still held straight, which reduces the uncertainties. The application of shorter measurement cycles of 0.25 s instead of 0.5 s for a tighter data coverage with setup T is not appropriate - the resolution limits of the method cannot be improved any more. We can improve the data quality when avoiding streamer deflections and measurements affected by long-period waves in the surf zone. Figure 2.7 and theoretical error estimations for the electrode pair $L/2 = 7 \text{ m}$ in Table 2.4 confirm that measurement uncertainties can hardly be estimated—our approaches provided overestimations of uncertainty sources. This is due to sea-level changes, e.g., long-periodical waves, which occur spatially and do not affect the entire sea surface, as expected for the theoretical estimations. Possible streamer deflections change permanently along the profile, and thus, errors are also smaller. Furthermore, uncertainty sources affect each other. A deflected cable causes water-level variations at the same time, which in turn influences the noise level. In summary, the measurement uncertainties cannot be corrected. Therefore, it is important to pay attention to a tidy measurement procedure and calm water conditions.

2.4.2 Spatial resolution

An inverse Schlumberger streamer applied in shallow water environments shows limitations in the resolution of layers, respectively object dimensions, and resistivity due to the water column. The evaluation of sounding curves of a 2L case shows that only for a specific resistivity up to $1 \Omega\text{m}$ does the apparent resistivity coincide with the specific resistivity of the second layer within our streamer length. Resistivity values up to $10 \Omega\text{m}$ can still be differentiated. Similar restrictions are also known for other geoelectrical configurations from the studies of Orlando (2013) and Kwon et al. (2005), investigating VES curves for Wenner α and Dipole–Dipole configurations. Both studies use a water resistivity of $1 \Omega\text{m}$ and a maximum sea bottom resistivity of $10 \Omega\text{m}$; nevertheless, the limitation of the “conventional” measurement configurations are already apparent in this case. The foremost improvement would be to increase the streamer length and therefore the electrode layout. With regard to the measurement streamer manageability and increased measurement and position uncertainties for large array lengths prospecting a big subsurface volume, this idea is not practical. Furthermore, coast-parallel measurements become more challenging with a long streamer. A study to overcome the limitations is presented by Baumgartner (1996). However, the approach is suitable for water depths of several meters and sufficient space across profile directions. Thus, “classical” measurement configurations should be chosen according

to their sensitivity with regard to the respective issue. Simyrdanis et al. (2015) suggest the Pole–Dipole and Schlumberger configuration in the prospection of archaeological objects. Orlando (2013) found a high sensitivity of the Dipole–Dipole configuration for thin layers below the sea floor. Numerous factors can improve the resolution of each measurement configuration, such as the measurement setup, and thus the measurement uncertainties, as well as a low water column and a low resistivity in the sea bottom. As an example, in a 3L case, with setup **S**, it is possible to differentiate between layer resistivity values that are approximately 5 times larger than for setup **F**, for the same depth and thickness of the layer. A duplication of the water layer allows, under otherwise equal conditions, to resolve resistivity values in the second layer of a 2L case decreased by the factor 2. Simyrdanis et al. (2015) also investigated the influence of the water depth. For instance, a water column of 1 m or 2 m makes a difference as to whether an isolated object of 5 m × 2 m in size can be resolved at a depth of 3 m or not using a 48 m long Pole–Dipole streamer. The resolution of layers in the sea bottom is more affected by the specific resistivity of the half-space than by measurement uncertainties. A specific resistivity of 1 Ωm or 10 Ωm of the half-space defines the resolution of a layer of 50 Ωm and 0.5 m thickness in depths >10 m or <4 m below the sea floor. Previous knowledge on the subsurface material is therefore useful for the success of measurements. In addition to the measurement uncertainty, the sensitivity of measurement setups is important for 2D measurements of lateral-limited objects. Thus, the lateral and vertical sensitivity of setup **S** and **F** in the sea bottom point out their advantages and disadvantages. These differences of the measurement setups are more important for numerous objects than for isolated objects. Simyrdanis et al. (2015) compare synthetic data representing meter-scale, isolated targets for submerged and floating electrodes of different measurement configurations. Their investigations show that submerged and floating electrodes both show good results for a varying target size and target depth for water depths of 1 m. The inversion results show that for submerged electrodes, the targets are located in greater depths than for floating electrodes. Floating electrodes show larger resistivity contrasts for a Schlumberger configuration than submerged electrodes. However, for complicated structures in the subsurface, they recommend using submerged electrodes. This suggestion can be confirmed from our investigations. With numerous objects laterally or vertically arranged, setup **S** provides a significant advantage. This also affects the prospection of objects in an unknown, heterogeneous sea bottom, with possible natural rock deposits. Setup **F** often blurs or does not resolve these structures. Due to the water column, the specific resistivity values of the inversion results do not correspond to the material of the objects for both setups.

2.4.3 Depth of penetration

The depth of penetration of our inverse Schlumberger array cannot be generalized, but depends on many factors: Measurement uncertainty, object or layer dimensions, depth and resistivity, as well as the resistivity of the surrounding material. In this study, we followed two approaches that provide information about the depth penetration in a

brackish water column of 1 m. We calculated sensitivity kernels of our array for floating and submerged electrodes. They define the change in apparent resistivity when the specific resistivity of a small volume in the subsurface is modified. Based on the calculations, our array is sensitive for both submerged and floating electrodes down to a depth of about 4 m. This can provide a first approximation for the planning of measurements. However, layers can also be resolved in larger depths. In our second approach, we have investigated the change in apparent resistivity due to an embedded layer in a homogeneous half-space, below the sea floor. In general, for lower resistivity values of the half-space, a layer can be resolved in greater depth. The approach also shows that there is a maximum depth of penetration regardless of layer thickness and resistivity. The maximum depth penetration was reached with setup **T** for layer thicknesses of 0.5 m and specific resistivity values of 1000 Ωm in depths of approximately 9 m for a half-space resistivity of 1 Ωm . In our investigations, the maximum depth penetration for setups **S** and **F** was not reached here. For a half-space resistivity of 10 Ωm , a layer resistivity of 1000 Ωm and thickness of 2 m, the penetration limit for setup **F** is approximately 8 m. It is essential that the sea bottom above the embedded layer is homogeneous. Our investigations using checkerboard tests show that for numerous objects laterally positioned, underlying layers are blurred. This effect should also be considered when debris has to be expected on the sea floor, for example.

2.4.4 Inversion ambiguity

The results of the stochastic inversion show that the strengths of marine geoelectric measurements are the prospection of the water column. Therefore, the method is suitable to investigate stratifications in the water column (caused by salinity and temperature). Objects in the water column can also be an area of application. Despite this, the method is challenging, as most issues focus stratification or objects in the subsurface. Here, the inversion results of the subsurface layers are ambiguous and therefore limited in interpretation. Simyrdanis et al. (2015) also report artefacts appearing in the inversion results. The correlation of subsurface parameters shows that a priori information in the inversion offers both advantages and disadvantages. As an example, Simyrdanis et al. (2015) confirms that for synthetic data, artefacts in the sea bottom can be reduced by specifying parameters of the water column. However, compared to field measurements, in this study, the specifications of water depth and resistivity are well known. In general, for 2D field investigations on the inversion reproducibility of the measured profile in Eckernförde, the results of the stochastic 1D inversion could be observed. This includes a well reproducible water column, as well as an identical lateral trend in the sea bottom for each measurement setup, showing different reproducibility. The difference in the deviations of setup **F** (<10%) and **T** (>10%) can be explained by measurement uncertainties. Setup **S** shows the lowest inversion reproducibility due to slightly erroneous a priori information on the electrode depth with respect to the water column, which is required here. This result is from the measurement uncertainty for determining the water depth in the Eckernförde Bay of 10 cm. Simyrdanis et al. (2015) and Orlando (2013) had similar experiences, observing these

effects for erroneous a priori information of the water column of 0.5 m. However, the setup is required to resolve numerous meter-scale objects. Therefore, lots of effort should be invested in the measurement of the water depth. Since even a low water column is usually stratified, no a priori information should be provided on this. Due to the ambiguities and a limited spatial resolution, an inline measurement distance of 1 m is more reasonable than that of 0.3 m for setup **T**. An inline measurement distance of 0.3 m can even cause more artefacts in the inversion results. Therefore, less data should be used for the inversion of setup **T** and the measurement setup should be applied for survey profiles only. In summary, measurement uncertainties do not affect average sea bottom structures. However, they can falsify the determination of the subsurface material. Inaccurate a priori information has a much more significant effect than measurement errors. Also, with other setups, only minimum specifications of subsurface parameters should be used.

2.4.5 The preferable measurement setup for prospecting a 2L respectively 3L/4L case

We suggest the following measurement setup for a 20 m long inverse Schlumberger streamer to investigate a layer or objects below a 1 m deep brackish water column: To prospect a 2L case, setup **T** is useful and time saving. A limited resolution of specific resistivity values $> 10 \Omega\text{m}$ has to be considered. Therefore, lateral/vertical changes in the inverted profiles should be interpreted rather than absolute specific resistivity values, so that the larger measurement uncertainties compared to setup **F** are not relevant. The prospection of multiple objects larger than $2 \text{ m} \times 2 \text{ m} \times 2 \text{ m}$ is enabled with setup **F/T**. The setup is easier to handle than setup **S**, area measurements are possible with less effort and there is no precise specification of the electrode depths necessary. An example is provided in Passaro (2010), prospecting a military vessel of 30 m length and 15 m width. The objects' dimensions of $2 \text{ i} \times 2$ in profile direction and into depth correspond to the sensitivity of setup **F**, as shown by the sensitivity kernels and checkerboard tests. The minimum object width of 2 m across the profile is based on possible streamer deflections. Setup **S** is appropriate for objects smaller than $2 \text{ m} \times 2 \text{ m} \times 2 \text{ m}$. However, we first suggest survey profiles in the surrounding area with setup **T** or **F** to collect information on the water stratification, bathymetry and the resistivity of the half-space in the sea bottom. This information can be taken from the inversion results, if any a priori information is given and if the sea bottom is homogeneous and less than $10 \Omega\text{m}$. Based on this, we can estimate for which object resistivity and depth we can expect changes in sounding curve compared to those of a homogenous half-space. In the next step, measurements should be performed with setup **S**. Electrodes submerged to the seafloor provide the lowest measurement and positioning uncertainty. However, the electrode depth has to be measured with centimeter precision and the geometry factor has to be corrected if necessary. If possible, a priori information should be given for the electrode/sea bottom depth, not the water resistivity during the inversion. To decrease the number of equivalent inversion solutions, it can be useful to include information on the half-space resistivity in the inversion. This is useful for 1D and 2D

analyses. Again, due to the water column, specific resistivity values in the inversion result decrease.

2.5 Conclusion

From our investigations regarding measurement uncertainty, spatial resolution, depth penetration and inversion ambiguities of an inverse Schlumberger streamer, we can draw conclusions on possible applications for offshore geoelectric sounding in the littoral zone. For example, marine geoelectric measurements are feasible for mapping archaeological stone settings embedded in sand, due to a sufficient resistivity contrast. However, the material differentiation between low-porosity rock masses is hardly possible for effective rock porosities of <15%. Wood constructions of meter-scale dimensions, such as remains of boats, can be well-distinguished from rocks. A sufficient material contrast to the (sandy) subsurface depends on a low weathering degree. Submarine freshwater lenses and discharges in sandy aquifers can be localized well. However, if the seafloor encounters massive low-porosity rock masses, difficulties in the differentiation may occur. Considering the differentiation between cohesive silty-clayey sediments and sandy sediments, their resistivity contrasts may be equal or even reversed compared to onshore investigations. With regard to the measurement setups, we recommend using submerged electrodes, especially for the prospection of meter-scale objects, e.g., archaeological issues. Littoral geological and hydrogeological mapping is also feasible with floating electrodes in a more time-saving way, accepting a decreased spatial resolution. Thus, geoelectric prospection in shallow water is a feasible complement to other geophysical methods, especially in situations where their use is limited. For high-resolution acoustic/seismic methods, this might be due to the presence of gases in the sediment, whereas magnetic measurements might be limited by nearby ferromagnetic structures or objects.

2.6 Appendix A

2.6.1 Resolution of layer thickness and resistivity from forward modelling of layered media

In horizontally layered media, the potential V , of a single point source at the surface is given by Parasnis (2012):

$$V(x) = \frac{I\rho_0}{2\pi x} \left(1 + \int_0^\infty K(\lambda) J_0(\lambda x) d\lambda \right) \quad (2.12)$$

$$= \frac{I}{2\pi} \int_0^\infty T(\lambda) J_0(\lambda x) d\lambda \quad (2.13)$$

$$\text{with } T(\lambda) = \rho_0(1 + 2K(\lambda)) \quad (2.14)$$

$T(\lambda)$ is the resistivity transform, $K(\lambda)$ is the kernel function, describing the "characteristic function", J_0 is the Bessel function of the zero order, λ is the integration variable, x is the distance between source and potential electrode, ρ_0 is the specific resistivity of the first layer and I is the current. For the Schlumberger configuration, the apparent resistivity ρ_a is obtained by measuring the spatial derivate of the potential of both current electrodes as a function of distance of the potential electrodes L :

$$\rho_a(L) = \frac{\pi L^2 U}{2l I} = \frac{\pi L^2 \Delta V}{I \Delta x} \quad (2.15)$$

$$\approx -\frac{2\pi L^2}{I} \frac{\partial V}{\partial x}_{x=L} \quad (2.16)$$

$$= \rho_1 \left(1 + 2L^2 \int_0^\infty K(\lambda) J_1(\lambda L) \lambda d\lambda \right) \quad (2.17)$$

$$= L^2 \int_0^\infty T(\lambda) J_1(\lambda L) \lambda d\lambda \quad (2.18)$$

J_1 is the Bessel function of first order, and l is the distance between the potential electrodes. The resistivity transform, $T(\lambda)$, for a media with n horizontal layers is described in Lagabrielle (1983); here, T_{fl} for a floating electrode setup differs from T_{sub} for a submerged electrode setup at the bottom of the first layer:

$$T_{fl}(\lambda) = \rho_0 \left(12 \frac{u_0 R_0}{1 - u_0 R_0} \right) \quad (2.19)$$

$$T_{sub}(\lambda) = \rho_1 \frac{1 - k_0}{2} \frac{(1 + u_0)(1 + u_1 R_1)}{1 - u_0 k_0 + u_1 k_0 R_1 - u_0 u_1 R_1} \quad (2.20)$$

with the resistivity values ρ_0 and ρ_1 of the first and second layers. Using the electric reflection coefficient k at the i_{th} layer interface,

$$k_i = \frac{\rho_{i+1} - \rho_i}{\rho_{i+1} + \rho_i} \quad (i = 0 \dots n - 1) \quad (2.21)$$

the depth attenuation of the sub-bottom layer with a thickness of e_i

$$u_i = e^{-2\lambda e_i} \quad (i = 1 \dots n - 1) \text{ (and)} \quad (2.22)$$

the depth attenuation of water layer with the thickness h

$$u_0 = e^{-2\lambda h} \quad (2.23)$$

the electric resistivity function R_i at the i_{th} layer interface below the electrodes can be calculated by the recursion formula:

$$R_i = \frac{k_i + R_{i+1}u_{i+1}}{1 + k_i R_{i+1}u_{i+1}} \quad (i = 0/1 \dots n-2) \quad (2.24)$$

starting at the lower most interface with

$$R_{n-1} = k_{n-1} \quad (2.25)$$

2.7 Appendix B

2.7.1 Sensitivity kernels

We present the formulas in the case of a layer over the half-space, where V_0 is the potential observed in the first layer and V_1 in the half-space. The formulas for the floating case are given by Bhattacharya and Patra (1968):

$$V_0(x_P, z_P; x_C) = \frac{I\rho_0}{2\pi} \int_0^\infty \left(e^{-\lambda z} + \frac{ke^{-2\lambda h}}{1 - ke^{-2\lambda h}} (e^{\lambda z} + e^{-\lambda z}) \right) J_0(\lambda(x_P - x_C)) d\lambda \quad (2.26)$$

$$= \frac{I\rho_0}{2\pi} \left(\frac{1}{\sqrt{((x_P - x_C)^2 + z_P^2)}} + \sum_{n=1}^{\infty} \frac{k^n}{\sqrt{((x_P - x_C)^2 + (2nh - z_P)^2)}} + \sum_{n=1}^{\infty} \frac{k^n}{\sqrt{((x_P - x_C)^2 + (2nh + z_P)^2)}} \right) \quad (2.27)$$

and

$$V_1(x, z; x_C) = \frac{I\rho_0}{2\pi} \int_0^\infty \left(e^{-\lambda z} + \frac{k(1 + e^{-2\lambda h})}{1 - ke^{-2\lambda h}} e^{-\lambda z} \right) J_0(\lambda(x_P - x_C)) d\lambda \quad (2.28)$$

$$= \frac{I\rho_0}{2\pi} \int_0^\infty \frac{k+1}{1 - ke^{-2\lambda h}} e^{-\lambda z} J_0(\lambda(x_P - x_C)) d\lambda \quad (2.29)$$

$$= \frac{I\rho_0}{2\pi} \left(\sum_{n=0}^{\infty} \frac{k^n (k+1)}{\sqrt{((x_P - x_C)^2 + (2nh + z_P)^2)}} \right) \quad (2.30)$$

h is the water depth, ρ_0 is the resistivity of the first layer, k is the reflection coefficient at the water/sea bottom interface, λ is the integration variable, x_C is the position of the current electrode, x_P is the position of the potential electrode, z_P is the depth of the potential electrode and J_0 is the Bessel function of the zero order. For the submerged case, we find:

$$V_0(x_P, z_P; x_C, z_C) = \frac{I\rho_0}{4\pi} \int_0^{\infty} \left(e^{-\lambda(z_P - z_C)} + e^{-\lambda(z_P + z_C)} + \frac{ke^{-2\lambda h}}{1 - ke^{-2\lambda h}} (e^{\lambda(z_P - z_C)} + e^{\lambda(z_P + z_C)} + e^{-\lambda(z_P - z_C)} + e^{-\lambda(z_P + z_C)}) \right) J_0(\lambda(x_P - x_C)) d\lambda \quad (2.31)$$

$$= \frac{I\rho_0}{4\pi} \left(\frac{1}{\sqrt{(x_P - x_C)^2 + (z_P - z_C)^2}} + \frac{1}{\sqrt{(x_P - x_C)^2 + (z_P + z_C)^2}} + \sum_{n=1}^{\infty} \frac{k^n}{\sqrt{((x_P - x_C)^2 + (2nh - (z_P - z_C))^2)}} + \sum_{n=1}^{\infty} \frac{k^n}{\sqrt{((x_P - x_C)^2 + (2nh - (z_P + z_C))^2)}} + \sum_{n=1}^{\infty} \frac{k^n}{\sqrt{((x_P - x_C)^2 + (2nh + (z_P - z_C))^2)}} + \sum_{n=1}^{\infty} \frac{k^n}{\sqrt{((x_P - x_C)^2 + (2nh + (z_P + z_C))^2)}} \right) \quad (2.32)$$

and

$$V_1(x_P, z_P; x_C, z_C) = \frac{I\rho_0}{4\pi} \int_0^{\infty} \left(e^{-\lambda(z_P - z_C)} + e^{-\lambda(z_P + z_C)} + \frac{2k(1 + e^{-2\lambda h})}{1 - ke^{-2\lambda h}} (e^{\lambda(z_P - z_C)} + e^{\lambda(z_P + z_C)}) \right) J_0(\lambda(x_P - x_C)) d\lambda \quad (2.33)$$

$$= \frac{I\rho_0}{4\pi} \left(\frac{1}{\sqrt{(x_P - x_C)^2 + (z_P - z_C)^2}} + \frac{1}{\sqrt{(x_P - x_C)^2 + (z_P + z_C)^2}} + \sum_{n=0}^{\infty} \frac{k^{n+1}}{\sqrt{((x_P - x_C)^2 + (2nh + (z_P - z_C))^2)}} + \sum_{n=0}^{\infty} \frac{k^{n+1}}{\sqrt{((x_P - x_C)^2 + (2nh + (z_P + z_C))^2)}} + \sum_{n=1}^{\infty} \frac{k^n}{\sqrt{((x_P - x_C)^2 + (2nh + (z_P - z_C))^2)}} + \sum_{n=1}^{\infty} \frac{k^n}{\sqrt{((x_P - x_C)^2 + (2nh + (z_P + z_C))^2)}} \right) \quad (2.34)$$

where z_C is the depth of the current electrode.

Author Contributions Conceptualization, A.F., D.W. and W.R.; methodology, A.F., D.W., M.T., T.W., E.E. and W.R.; software, A.F., D.W. and M.T.; validation, D.W., M.T., E.E. and W.R.; formal analysis, A.F.; investigation, A.F.; resources, A.F.; data curation, A.F.; writing—original draft preparation, A.F.; writing—review and editing, D.W., M.T., T.W. and E.E.; visualization, A.F.; supervision, D.W., M.T., E.E., T.W. and W.R.; project administration, W.R.; funding acquisition, D.W., T.W. and W.R. All authors have read and agreed to the published version of the manuscript.

Funding The research leading to these results has received funding by the German Research Foundation (DFG) in a project (RA 496/26-2) situated in the frame of the Priority Program 1630 ‘Harbours from the Roman Period to the Middle Ages’ (of Carnap-Bornheim and Kalmring 2011). We acknowledge financial support by DFG within the funding program “Open Access Publizieren”.

Acknowledgements The authors acknowledge support, especially from Michael Gräber (GeoServe, Kiel) with his equipment and help during the field work. Special thanks are also dedicated to the students who assisted with the field work in Eckernförde. The electric data was processed and analyzed with the software RES2DInv v. 3.71 and IX1D v. 3 by Interpex.

Conflicts of Interest The authors declare no conflict of interest. The funders had no role in the design of the study; in the collection, analyses, or interpretation of data; in the writing of the manuscript, or in the decision to publish the results.

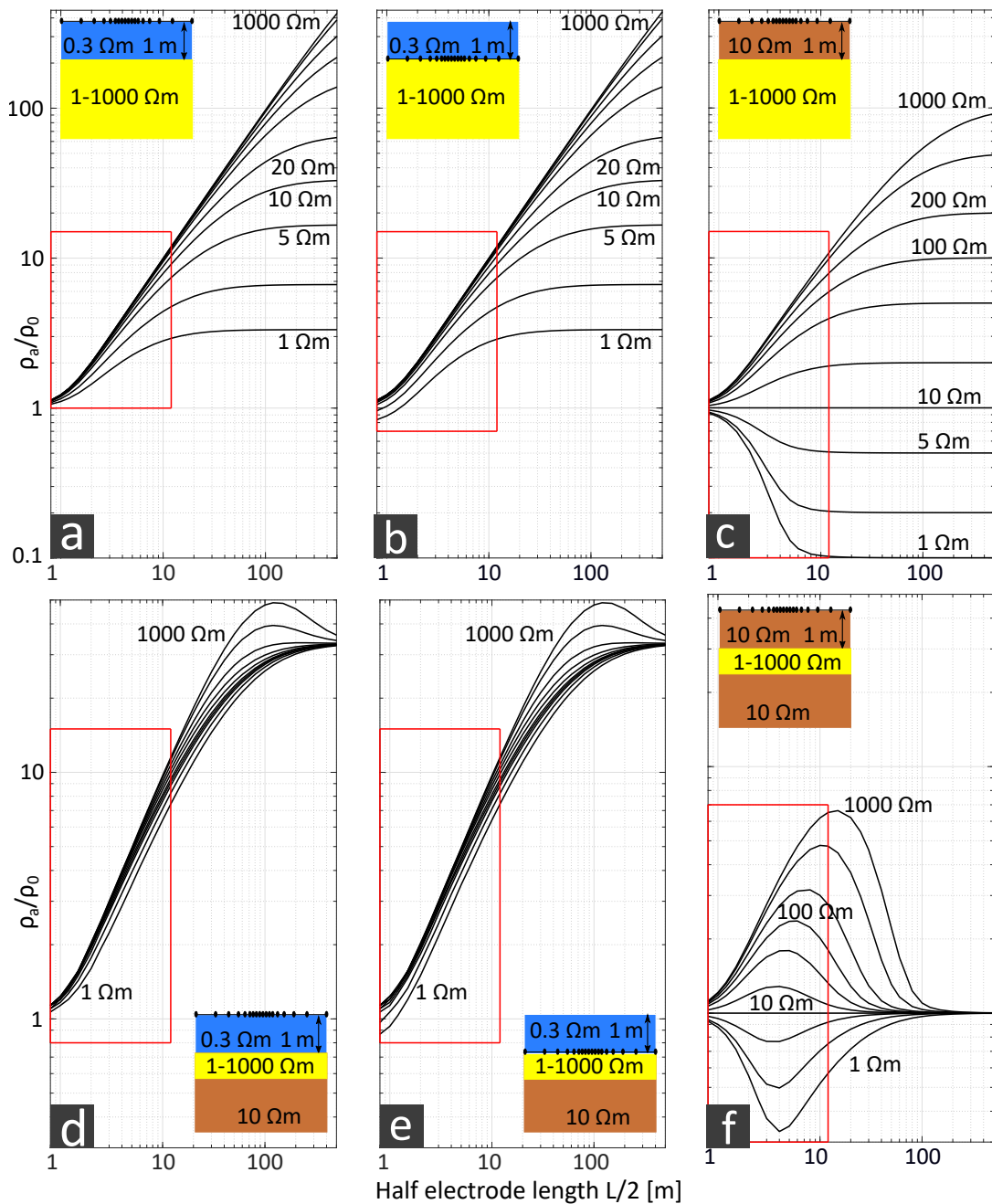


Figure 2.10: Comparison of Schlumberger sounding curves for a 2L case (top row) and a 3L case (bottom row). 2L case: fixed top layer of 1 m depth and 0.3 Ωm for a) setup F, b) setup S and 10 Ωm for c) an onshore scenario. The resistivity of the second layer varies from 1 Ωm –1000 Ωm . 3L case: fixed top layer of 1 m depth and resistivity values of 0.3 Ωm for d) setup F, e) setup S in a shallow water environment and 10 Ωm for e) an onshore scenario. Resistivity values of the second layer (1 m depth) vary from 1 Ωm –1000 Ωm , the third layer is fixed with 10 Ωm . Red box: array length used within the field measurements.

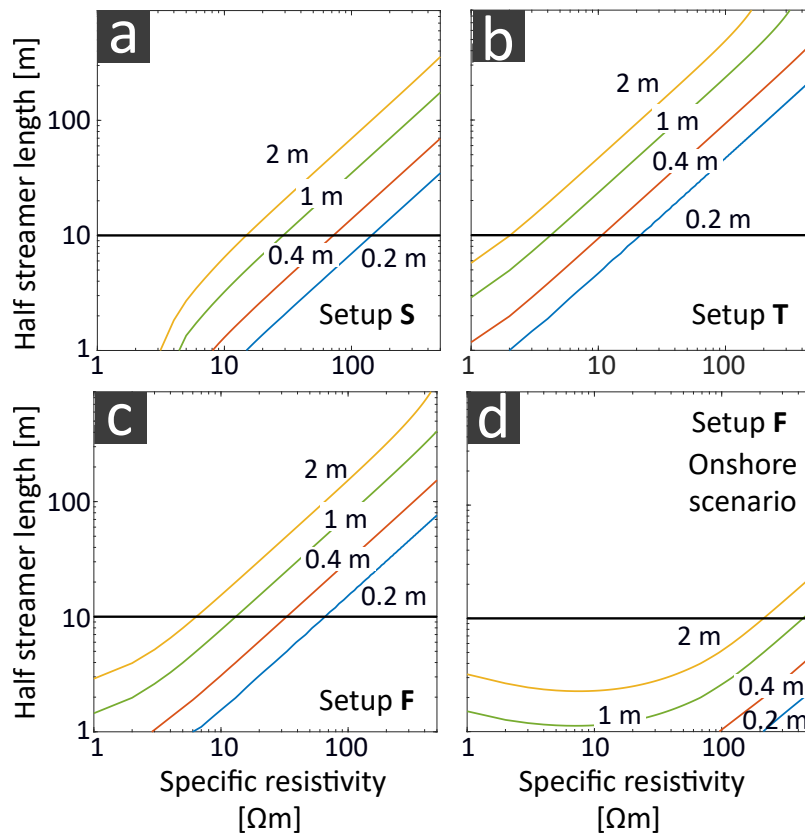


Figure 2.11: Required streamer length (y-axis) to resolve the specific resistivity of the homogeneous half space of a 2L case (x-axis) with a tolerance of 100%. We differentiate between a shallow water (a-c) and an onshore scenario (d) and the measurement setups **S** (submerged, a), **T** (towed, b) and **F** (floating, c-d). We use water depths from 0.2 m–2 m

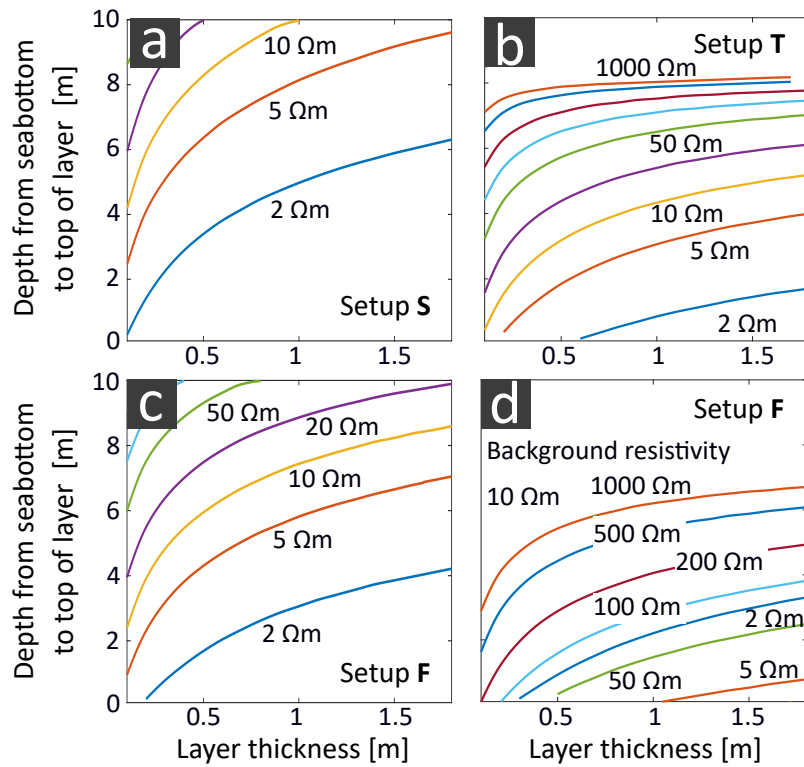


Figure 2.12: Plot of the maximum depth to which a layer of variable thickness and resistivity can be differentiated from the surrounding sea-bottom. The depth is defined as the distance between the sea floor for a brackish water column of 1 m to the upper edge of the layer. The sea-bottom shows resistivity values of 1 Ωm (a-c) and 10 Ωm (d). The measurement uncertainties of setup S (submerged, a), F (floating, c-d) and T (towed, b) are compared.

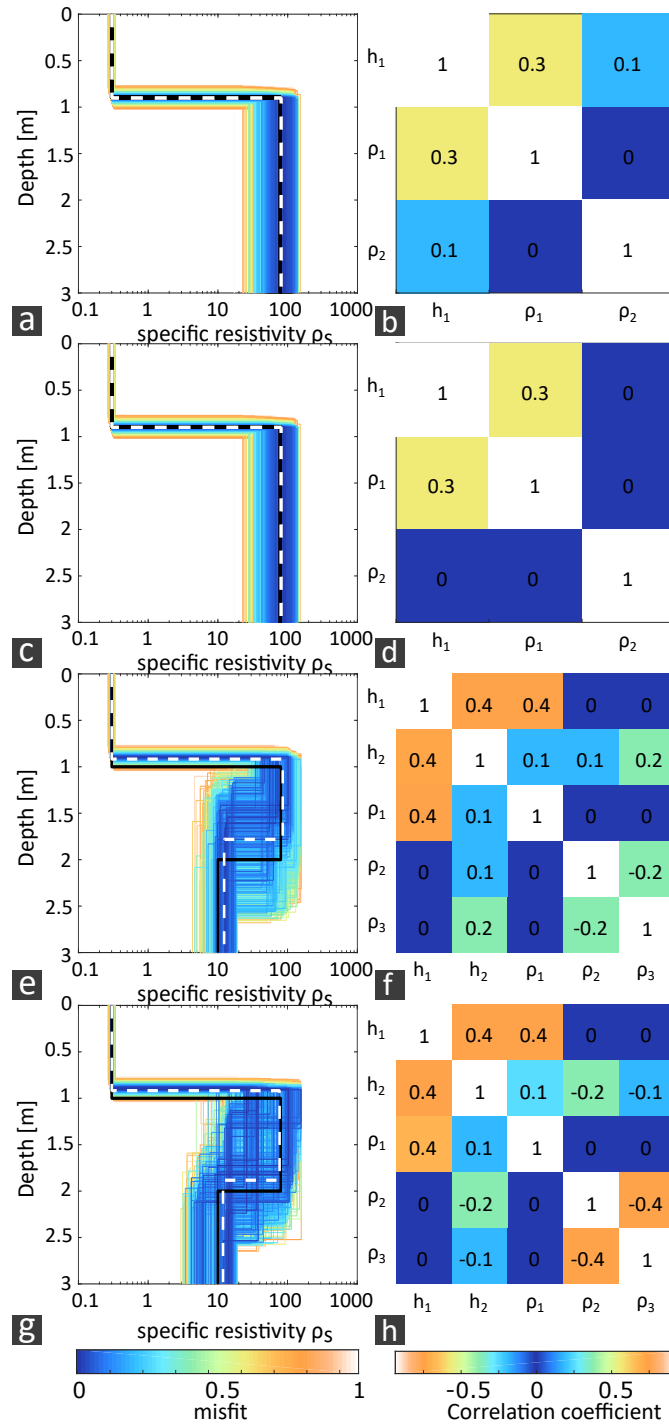


Figure 2.13: Left column: Model results from the stochastic inversion, color-coded by their misfit values and normalized to the relative misfit of 14%. The black line represents the true model; the white dashed line represents the expected model. Right column: normalized correlation matrix of the subsurface parameters. Case 2L and setup F (a-b), case 2L and setup S (c-d), case 3L and setup F (e-f) as well as case 3L and setup S (g-h) are distinguished.

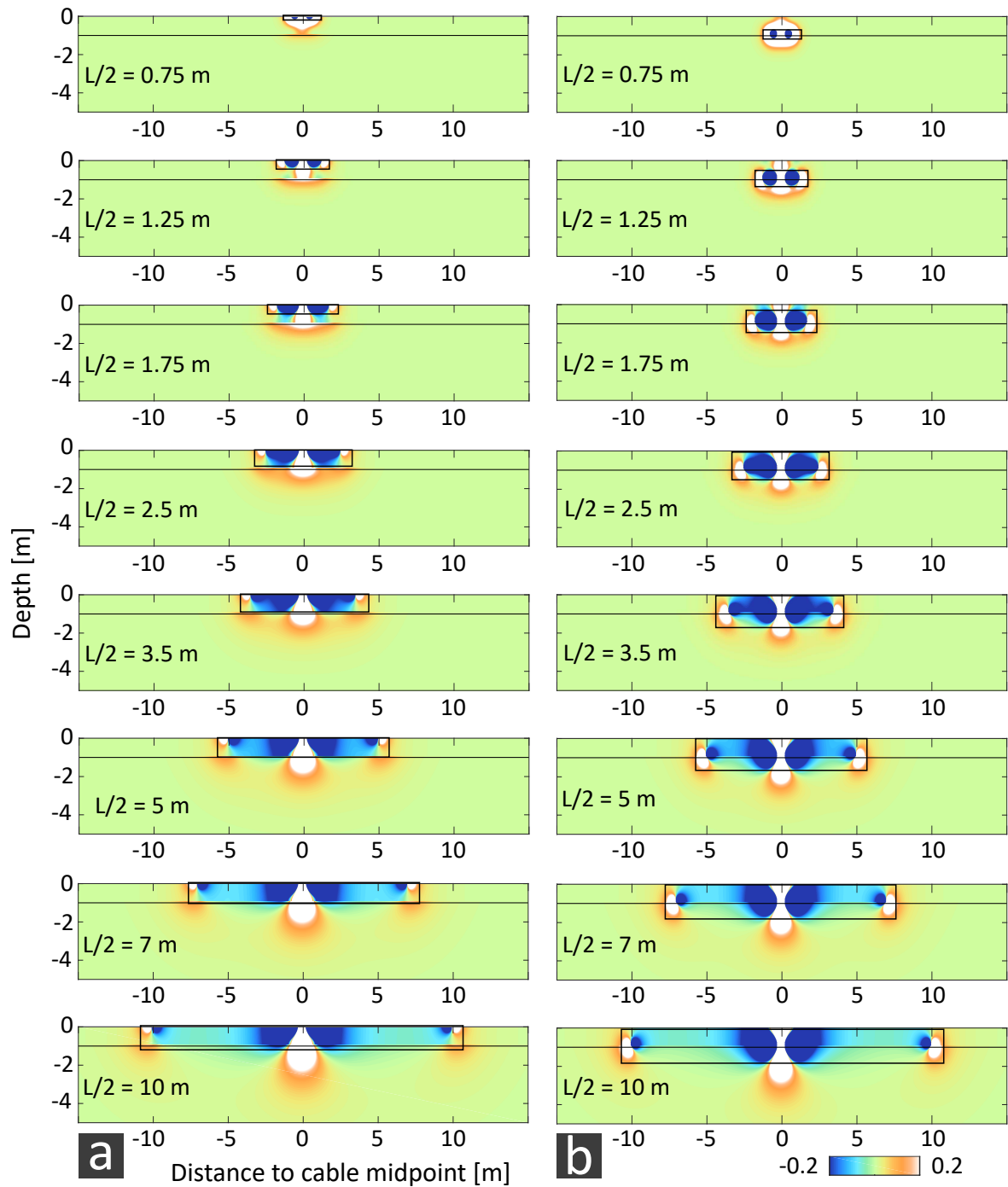


Figure 2.14: Comparison of sensitivity kernels from the inverse Schlumberger array used for repetition measurements in Eckernförde Bay, Germany, consisting of eight electrode pairs (Table 2.1). a) setup F and b) setup S are compared, the lateral highly sensitive area is framed in black.

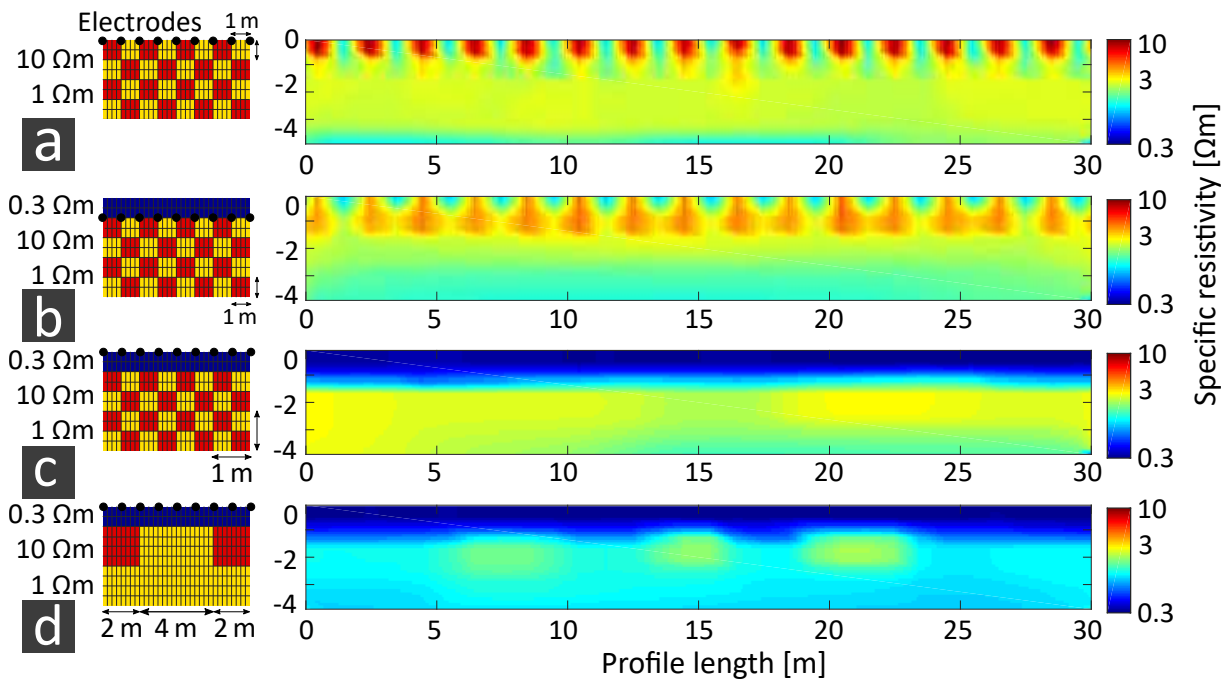


Figure 2.15: Left column: Synthetic checkerboard pattern of 1 m×1 m size with subsurface resistivity values of 1 Ωm and 10 Ωm, an additional water column of 1 m depth and 0.3 Ωm resistivity for shallow water measurements. For d), one row of 2 m×2 m pattern size and a lateral distance of 4 m was chosen. Right column: 2D inversions of synthetic checkerboard data. a) Onshore electrode setup, b) setup S, c) and d) setup F.

3 Ground- Penetrating Radar measurements in shallow water environments- a case study

Abstract In this study, we investigate GPR measurements in freshwater of less than 5 m at four different locations to derive rules of thumb in terms of depth penetration, resolution and material contrasts of the method for 200 MHz and 400 MHz antennas under field conditions. The objective is to improve the attractiveness of the method for archaeological issues in water, as there are hardly any studies on this subject so far. The depth penetration of 2 m–4 m is negligibly influenced by the choice of the 200 MHz or 400 MHz antenna. Organic material in the water column also does not affect the water depth, but offers new fields of applications for mapping and volume estimation of biomass in lakes with GPR. The horizontal resolution in the cm range in the direction of the profile and in the dm range across the profile could not be improved by the narrow antenna radiation pattern of $<30^\circ$ at the 3dB level. In crossline direction, the use of an antenna array would be necessary here. Still, the narrow antenna pattern reduces side reflections. Most common archaeological material contrasts can be resolved with the method. The method shows reflection coefficients >0.1 for materials of $<80\%$ porosity to the water column and for materials of $<25\%$ porosity and of $>45\%$ porosity to water-saturated sand. Large reflection coefficients also show, for example, granite to sand and gyttia to wood. The water column has a considerable effect on the data quality of the 400 MHz antenna from a depth of 2 m due to the antenna ringing. Furthermore, multiples must be expected in a water column <0.5 m. The method can especially complement the common geophysical methods seismics and geoelectrics to exclude material ambiguities. The major advantage is the simple setting of the land equipment in the water.

3.1 Introduction

Ground-penetrating radar has been successfully applied for archaeological prospection of objects on land since the 1970s (Vickers and Dolphin, 1975; Kenyon and Bevan, 1977; Bevan, 1977). Although interest in submerged anthropogenic constructions, such as ancient harbour facilities, has gained much archaeological interest, the method has been used only rarely for archaeological prospection in the shallow water zones. The common geophysical approach in marine and lacustrine archaeological investigations is seismic/acoustic measurements, providing a spatial resolution in the cm

range and a depth of penetration of more than 20 m (Fediuk et al., 2019; Bull et al., 2005; Gutowski et al., 2008). In recent years, geoelectric investigations were also used for the detection of archaeological objects in shallow water (Seeliger et al., 2014; Kritikakis et al., 2015; Simyrdanis et al., 2016). Here, an average spatial resolution in the dm-to-m range is achieved. Still, there are some situations where the usability of the common seismic and geoelectric methods is limited, and the application of GPR measurements in water appears to be advantageous.

These advantages are as follows:

- a) Seismic measurements may not be possible due to an extremely shallow water column (Ruffell, 2006; Delaney et al., 1992), may be affected by multiples, or may be attenuated by a gassy subsurface (Whiticar et al., 1986). In particular, Delaney et al. (1992) as well as Lin et al. (2010) suggested a joint application of the methods GPR and seismics in shallow water.
- b) In the presence of organic material in the water column, Kovacs (1991) and Shields et al. (2004) were able to investigate the underlying bathymetry more accurately with GPR than with seismic surveys.
- c) A variety of material contrasts from submerged archaeological structures can be better resolved with GPR than with seismics. An example is the reflection coefficient of oak wood to wet sand (Fediuk et al., 2020b).
- d) Special equipment is necessary for marine seismics and geoelectrics (Wilken et al., 2019; Fediuk et al., 2020a), whereas standard GPR antennas can be used in the water without much additional time and financial effort. In contrast, for GPR, only an appropriately watertight box is required, in addition to a small boat (Jol and Albrecht, 2004; Abramov and Vasiliev, 2004).

The main factor limiting the regular application of GPR in water is the high attenuation of electromagnetic waves with increasing salinity of the water (Annan, 2003). Thus, there are only few examples investigating marine archaeological targets with GPR. Leckebusch (1998) was able to detect the archaeological layer of the bronze-age settlement "Greifensee-Böschen", Switzerland, on a prospection area of 11 m × 18 m. Fuchs et al. (2004) contribute to the landscape reconstruction around a submerged archaeological site, distinguishing between beach and glaciolacustrine clay deposits. Abramov and Vasiliev (2004) developed a submerged GPR equipment for archaeological investigations of submerged stonewalls in 2 m depth below a 1 m saltwater column. Some other studies focus on the detection of sunken objects in freshwater and below the bottom, for example, logs (Jol and Albrecht, 2004), jet skis (Ruffell, 2006), and munition (Arcone et al., 2010), usually using 200 MHz and 400 MHz GPR antennas for a centimetre - to decimetre-scale resolution. In other areas of application, several studies using offshore GPR measurements were carried out, for example, in the prospection of ice shields and geological issues. The first GPR measurements on ice took place since the 1960s (Waite and Schmidt, 1962) and were investigating arctic regions, for the determination of ice thicknesses (Annan and Davis, 1977). Other offshore appli-

cations of GPR have been the detection of groundwater (Arcone et al., 1992) and of thermal boundaries (Stevens et al., 2008). Powers et al. (1999), Buynevich and Fitzgerald (2003) and Moorman and Michel (1997) present investigations on the morphology, stratigraphy, and bathymetry in coastal ponds. Further applications are presented by Gorin and Haeni (1989), focussing on riverbed scour and Costa et al. (2006), monitoring stream discharge. To improve the depth penetration, Park et al. (2004) used a 5 m submerged 400 MHz antenna to prospect riverbed scour in 8 m depth. There are different studies determining the sedimentary type, for example, from diffraction hyperbola velocities presented by Sambuelli and Bava (2012), and from determining reflection coefficients based on the ratios of reflected signal strengths from sediments and a reference aluminium plate (Lin et al., 2010).

Within the context of geological and ice shield investigations, extensive research has been carried out on the physical impact of the water column on GPR measurements for antenna frequencies of 60 MHz–150 MHz and water depths of more than 5 m (Kovacs, 1991; Schwamborn et al., 2002; Arcone, 1995; Sellmann et al., 1992). Within these studies, parameters such as the spatial resolution, depth of penetration, and antenna pattern, as well as specific effects such as a frequency reduction and an antenna impedance loading, are discussed. Effects that occur specifically in water, such as the “ringing” (horizontal stripes in the water column as a consequence of the high dielectric contrast between air and water), are regularly described. A more detailed overview will be given in the following sections.

In the rare archaeological case studies using limnic GPR, there is no rule of thumb for practical considerations with respect to, for example, penetration depth or resolution. Moreover, if there would be such a rule, would it hold true for very different measurement locations with respect to water depth, water conductivity, and organic matter content in the water column? To answer these questions, we present four datasets using offshore GPR in different limnic environments and using two typical antenna frequencies (200 MHz and 400 MHz). With the help of these datasets we focus on three thematic issues.

- i) The depth of penetration of GPR measurements depends on numerous factors, such as subsurface material and antenna properties. Is it still possible to determine basic rules of thumb for field applications? How do organic materials, such as leaves in the water column, affect the depth of penetration?
- ii) Up to which degree can archaeological constructions be spatially resolved within the possible depth range? Which aspects have to be considered regarding the resolution along and across profile directions?
- iii) For which archaeological material contrasts is the GPR method particularly suitable compared to seismics and electrics? Which additional areas of application arise?

To answer the three questions, we compare the results of previous studies and of theoretical considerations with our data measured under field conditions. For the third

aspect, we determine theoretical archaeological material contrasts from both common sub-bottom and archaeological construction materials and compare these to our field data.

3.2 Measurement locations

To answer the three issues of penetration depth, spatial resolution, and material contrasts of water-based GPR measurements under field conditions, we surveyed GPR profiles with both 400 MHz and 200 MHz antennas from GSSI and an SIR 4000 registration unit at four different locations. The measurement locations differ in terms of water depth, water conductivity, and subsurface materials, as well as movement and stratification of the water column.

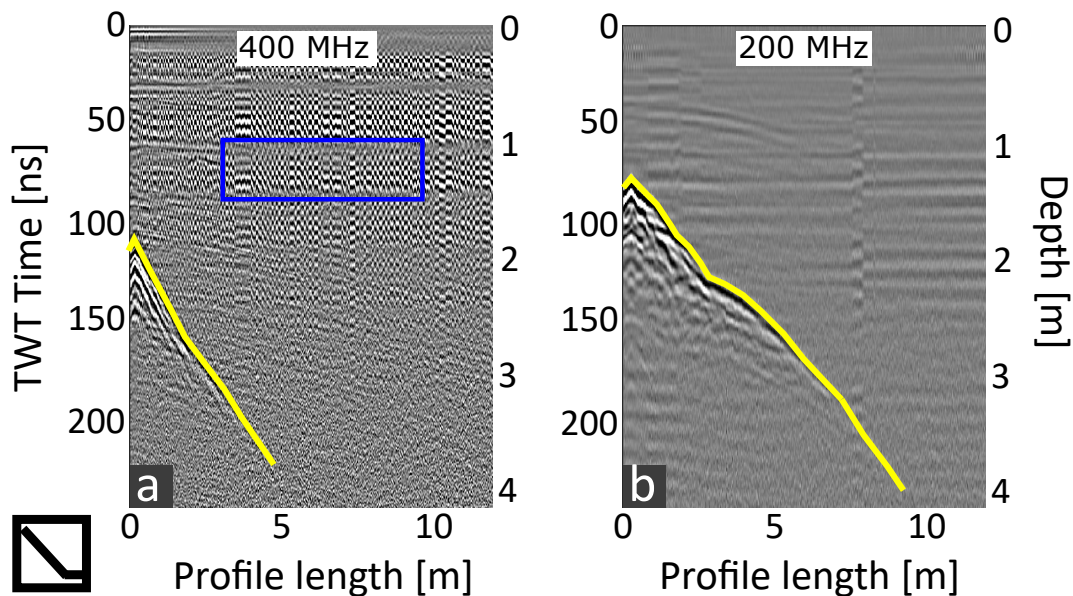


Figure 3.1: GPR profiles comparing the 400 MHz and 200 MHz antenna from GSSI using a SIR-4000 registration unit at the measurement location “Flooded gravel pit”. The data was processed with t_0 correction, bandpass filter, fk-filter, background removal and trace normalizing. The lake bottom is highlighted yellow; remarkable noise in the water column is framed blue.

The first chosen measurement location (“Flooded gravel pit”) is situated near Wörth at Rhine, Rhineland-Palatinate, Germany (Figure 3.1). Here, the gravelly shoreline slopes steeply to the centre of the lake (yellow line), and we find the largest water depths >4 m at all locations. Figure 3.1 shows exemplary measurement profiles of the 200 MHz and 400 MHz antennas at slightly different locations in the “flooded gravel pit”. This feature is useful for answering the question of the penetration depth as a function of the antenna frequency and the attenuation coefficient due to the water column. The noticeably high noise content in the water column, especially for the

400 MHz antenna (blue frame), invites us to analyse the data quality in relation to the water depth and the antenna frequency.

The second location chosen for GPR measurements, "Swimming pool" (Figure 3.2), is weather protected and can be used for repeated measurements under constant conditions (water temperature, water conductivity). The sloping ground (yellow dashed line) is tiled. The question of the penetration depth for different antenna frequencies can be also investigated here. In addition, it was possible to lower a pipe of 7 cm diameter (red circle) in a controlled setting. From this, as well as from steps leading into the pool (blue frame), it was possible to address the issue of the spatial resolution under field conditions here.

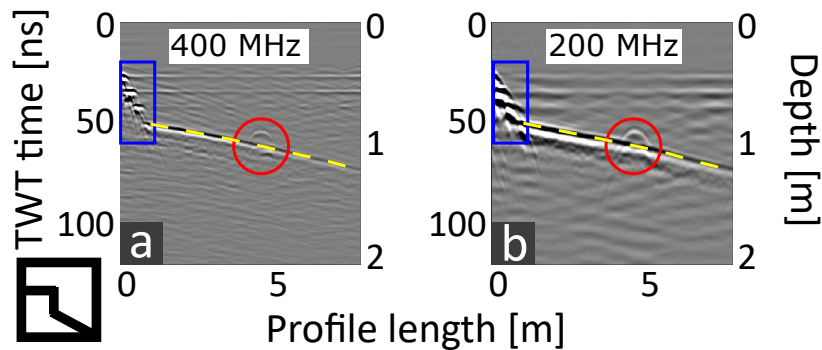


Figure 3.2: GPR profiles comparing the 400 MHz and 200 MHz antenna from GSSI using a SIR-4000 registration unit at the measurement location "Swimming Pool". The data was processed with t_0 correction, bandpass filter, fk-filter, background removal, and trace normalizing. The pool bottom is highlighted with a yellow dashed line, steps to the pool are framed blue and a lowered piped is marked with a red circle.

The third location "River", a section of the Altmühl River, Bavaria, Germany (Figure 3.3), is the only measurement location with flowing water. Its subsurface (yellow line) mostly consists of sand or sandbars (Figure 3.3b). At some spots, larger boulders appear in clusters (Figure 3.3a) or fish pass below the antenna. The resulting diffraction hyperbolas (red circles) are again well suited for analysing the spatial resolution under field conditions. In addition, especially in very shallow water <30 cm, further measurement effects are visible in form of multiples (Figure 3.3b, green dotted lines), which must be considered when planning GPR measurements in water.

The last measurement location ("Pond") near Graben, Bavaria, Germany (Figure 3.4) is the flooded remnant of a collapsed trench. Its moderately sloping subsoil (yellow line) consists of mud, (i.e. silty sediments and gyttja), due to leaves and wood from surrounding trees. According to Corradini et al. (2020), gyttja is a combination of organic and inorganic materials precipitated from a lake water column via biogeochemical processes. Larger branches or tree trunks also cause diffraction hyperbolas (red circles). These conditions are again suitable for investigating the questions of depth penetration and spatial resolution. The most striking feature, however, is that different amounts of organic material can be found in the water column at various parts of

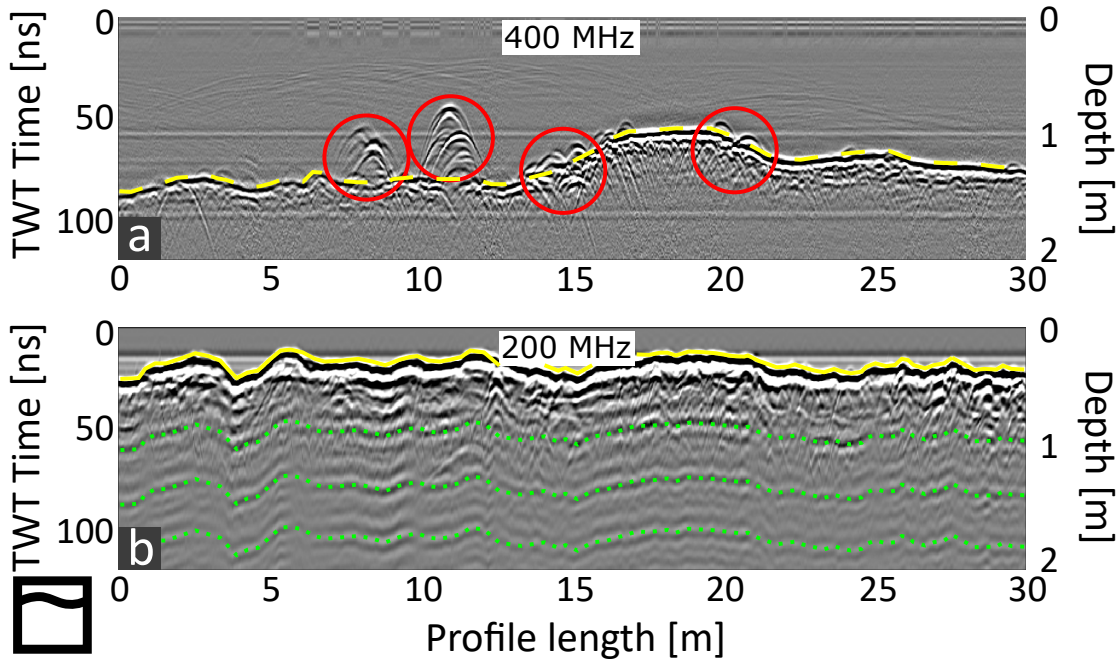


Figure 3.3: GPR profiles comparing the 400 MHz and 200 MHz antenna from GSSI using a SIR-4000 registration unit at the measurement location “River”. The two antenna frequencies were used to prospect different sections of the river with varying water depths. The data was processed with t_0 correction, bandpass filter, fk-filter, background removal, and trace normalizing. The river bottom is highlighted with a yellow (dashed) line, diffraction hyperbolas are marked with a red circle; multiples are emphasized via green dotted lines.

the pond. There are parts with no organic material in the water column (Figure 3.4b, blue frame) as well as parts where no boat engine could be used due to the organic material in the water column (Figure 3.4b, green frame). From the direct comparison of lake bottom amplitudes, we can determine how much organic material in the water column scatters the GPR measurements and thus reduces the measured amplitudes in the radargram.

In addition, the subsurface materials sand, gravel, mud and tiles of all four measurement locations were used to investigate the issue of expected material contrasts. The most important environmental and measurement parameters of all locations are summarized in Table 3.1.

3.3 Methods

This section first introduces the field equipment of the 200 MHz and 400 MHz antenna from GSSI and the standard processing applied to the data. In the second step, we focus on the study procedure. Sections 3.3.2 and 3.3.2 discuss the depth penetration,





	"Flooded gravel pit"	"Swimming Pool"	"River"	"Pond"
				
Water column	Stagnant	Stagnant, Vertical stratified	Flowing	Stagnant
Ground material	Gravel	Tiles	Sand	Mud
Water depth	1.2-5 m	0.8-4 m	0.2-0.4 m	0.6- 1.5 m
Water resistivity	24.9 Ωm	11.2 Ωm	17 Ωm	Unknown
Antenna	400& 200 MHz	400& 200 MHz	400& 200 MHz	400 MHz
Stacking	16	16	16	16
Range	240 ns	120 ns	120 ns	120 ns
Number of Samples	822	411	411	411
dt	0.292 ns	0.292 ns	0.292 ns	0.292 ns
Average wave velocity (according to diffraction hyperbolas in the water column)	3.3 $\frac{\text{cm}}{\text{ns}}$	3 $\frac{\text{cm}}{\text{ns}}$	3 $\frac{\text{cm}}{\text{ns}}$	3.3 $\frac{\text{cm}}{\text{ns}}$

Table 3.1: Comparison of water and soil properties and of the measurement setup for the GPR investigations at four different measurement locations: Swimming pool, Pond, River system and Flooded gravel pit.

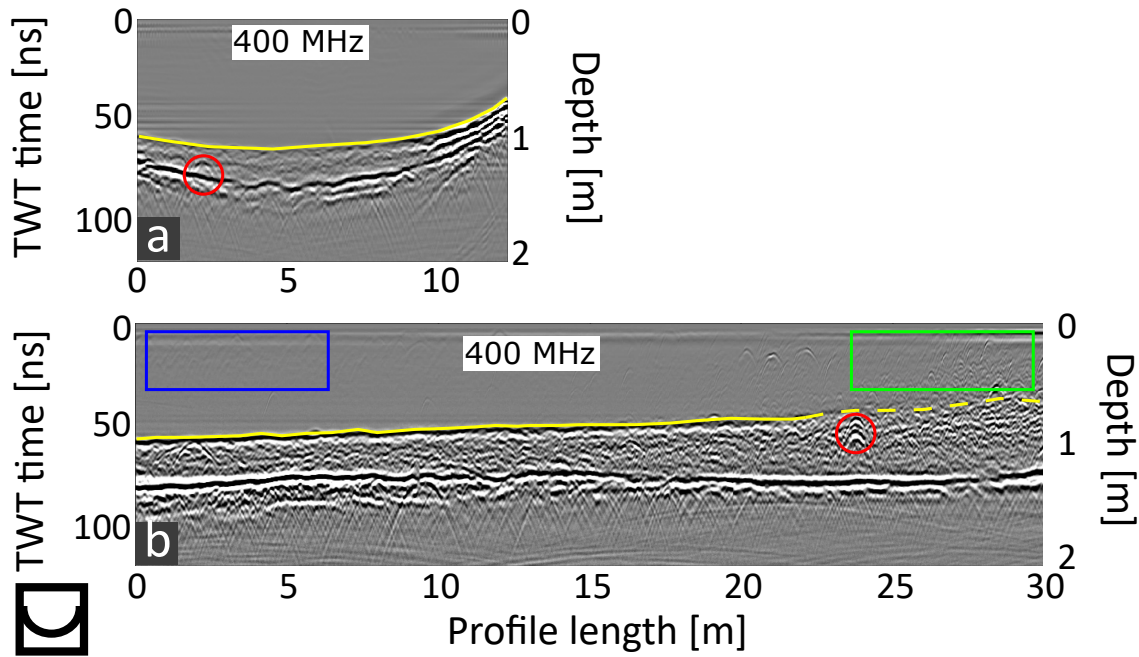


Figure 3.4: GPR profiles using a 400 MHz antenna with a SIR-4000 registration unit at the measurement location “Pond”. The data was processed with t_0 correction, bandpass filter, fk-filter, background removal, and trace normalizing. The bottom is highlighted with a yellow (dashed) line, diffraction hyperbolas are marked with red circles. Parts of much and no organic material in the water column are emphasized via green and blue frames.

while in section 3.3.2, the preliminary considerations on attenuation are made. Sections 3.3.2 and 3.3.2 address the issue of spatial resolution and of material contrasts, respectively.

3.3.1 GPR data acquisition and standard processing

Field Equipment

For the field measurements, 200 MHz and 400 MHz antennas from GSSI were used in combination with the SIR 4000 registration unit from GSSI. One measurement system (Figure 3.5a) included a small inflatable boat with an inflatable catamaran attached to the front. The antenna was fixed in a floating box, which was installed in the catamaran. The system was moved by an electric engine or manual rowing. The positioning for the measurement locations pond and river was realized using a total station with automatic target tracking. Thus, a coordinate was collected averagely each 30 cm. As an additional option, an RTK-DGPS (real-time kinematic differential global positioning system) was used for the measurements at the flooded gravel pit. In another setup for measurements in the swimming pool, only the floating box was used (Figure 3.5b). It could be towed inline in forward and backward directions with ropes. The ropes were marked each metre and used for manual positioning of the antenna with the help

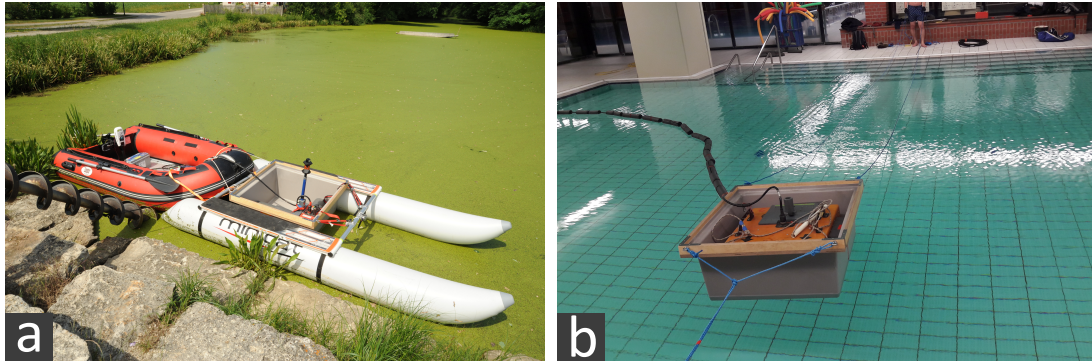


Figure 3.5: a) Standard GPR acquisition system that consists of a floating box containing the GPR antenna, which is attached to a catamaran, which in turn is navigated by an inflatable boat using an electric motor. The positioning is realized with a total station. b) Measurement setup of a 200 MHz antenna in the swimming pool, using a floatable box. The position was set by hand each metre, based on rope markers.

of measuring tapes on the edge of the pool.

Standard processing

Unless specified otherwise, the following standard processing with optional steps was applied to all data:

- Set coordinates;
- Interpolation to a constant trace interval (2 cm);
- Zero-time correction;
- Geometric spreading correction;
- Band pass filtering (50-100-800-850 MHz for the 400 MHz antenna and 25-50-400-425 MHz for the 200 MHz antenna);
- K-High pass (cutoff wavenumber $k = 0.1 \frac{1}{m}$);
- Background removal (subtracting the mean trace);
- Amplitude normalization with respect to the maximum amplitude for a better visualization;
- Optional: Attenuation correction;
- Optional: Kirchhoff migration - The average water wave velocities listed in Table 3.1 were determined using diffraction hyperbolae. Thus, the travel times could

be converted to depth using the following equation:

$$depth = water\ velocity \cdot \frac{two-way-traveltime}{2} \quad (3.35)$$

3.3.2 Study procedure

Attenuation effects

Before addressing the question of maximum sounding depths of waterborne GPR measurements, we compile the equations summarizing the major effects causing amplitude decay during wave propagation. We assume that the water column is almost homogeneous and that the lake bottom can be approximated by a local plane interface. In this case, the following equation applies to the amplitude A of the sea bottom reflection for near-vertical incidence angles (Annan, 2005).

$$A(s) = A_0 R \frac{s_0}{s} e^{-\alpha(s-s_0)} \quad (3.36)$$

where s is the length of the reflected ray path; $A_0 = A(s_0)$ is a reference amplitude measured at near distance s_0 from the source, including all instrumental effects; R is the reflection coefficient at the lake bottom; and α is the water attenuation coefficient. The amplitude decay along the ray is described by the geometrical spreading term $1/s$ and the attenuation term $e^{-\alpha s}$, with the latter combining both intrinsic absorption and scattering losses. If the lake bottom is variable in depth and its reflexion coefficient R is constant, α can be determined from lake bottom reflection amplitudes $A_j (j = 1, 2, \dots)$ picked along the radar section. Rearranging Equation 3.36 for each picked amplitude value enables computing α through the slope of the regression line fitting

$$\log(s_j A_j) = [\log(s_0 A_0 R) + \alpha s_0] - \alpha s_j \quad (3.37)$$

where $s_j A_j = s_j A(s_j) (j = 1, 2, \dots)$ are the spreading-corrected picked amplitude values. Ray length $s_j = v t_j$ is computed from the two-way-traveltime t_j of the reflection and the radar wave velocity v . The square-bracket term on the right-hand side we define as the constant b , which is the impact of the reflexion coefficient and the antenna parameters on the depth penetration, defined in Section 3.3.2.

The amplitudes of electromagnetic waves can be attenuated not only intrinsically (i.e., by electric conduction and dielectric relaxation), but also by scattering (Annan, 2005). This may occur especially in lacustrine environments showing an increased density of floating organic particles of diameters much smaller than the wavelength. To account for these different attenuation effects we express the attenuation coefficient via Wunderlich and Rabbel (2013):

$$\alpha = \frac{\pi}{Q\lambda} \quad (3.38)$$

where λ is the wavelength, and Q is the quality factor, which is defined by

$$\frac{1}{Q} = \frac{\text{lost energy}}{2\pi \cdot \text{maximum stored energy per cycle}} = \frac{1}{Q_{int}} + \frac{1}{Q_{sc}} \quad (3.39)$$

where $1/Q_{int}$ and $1/Q_{sc}$ represent the intrinsic and scattering portions of energy loss per cycle (Annan, 2005).

For a signal of angular frequency ω , the intrinsic quality factor Q_{int} can be determined via Wunderlich and Rabbel (2013)

$$Q_{int} = \frac{\omega\epsilon'}{\sigma + \omega\epsilon''} \quad (3.40)$$

where σ is the electric conductivity, and ϵ' and ϵ'' are the real and imaginary parts of complex dielectric permittivity.

For applying these equations to the interpretation of field measurements, σ has to be determined, for example, by a conductivity meter. For our frequency range from 200 MHz to 400 MHz, ϵ' corresponds to the value of the static permittivity ϵ_s in water and is temperature dependent (Schwan et al., 1976). At a water temperature of 10 °C it is $\epsilon_s = 84$, while at a water temperature of 25 °C the value is $\epsilon_s = 78$. In water, ϵ'' can be determined via the Debye relaxation model (Schön, 1983):

$$\epsilon'' = \frac{(\epsilon_s - \epsilon_\infty) \cdot \omega\tau}{1 + \omega^2 \cdot \tau^2} \quad (3.41)$$

where ϵ_s is again the static permittivity, τ is the relaxation time of the water molecules, and ϵ_∞ is the high-frequency permittivity. The parameters τ and ϵ_∞ are also dependent on temperature and have been determined empirically in laboratory experiments (Kaatze, 1989). For a water temperature of 10 °C they are $\epsilon_\infty = 5.5$ and $\tau = 12.68 \cdot 10^{-12}$. For a water temperature of 25 °C they are $\epsilon_\infty = 5.2$ and $\tau = 8.27 \cdot 10^{-12}$. Unlike many other studies, we investigate and consider the impact of ϵ'' .

Once the attenuation coefficient α and intrinsic quality factor Q_{int} have been determined and we assume a constant reflection coefficient in the subsurface, we suppose that we can quantify the scattering portion of energy attenuation by inserting and rearranging Equations 3.38 to 3.40 into

$$\frac{1}{Q_{sc}} = \frac{\lambda\alpha}{\pi} - \frac{\sigma + \omega\epsilon''}{\omega\epsilon'} \quad (3.42)$$

The application of Equation 3.37 to the field examples will provide us insight into the actual signal attenuation in waterborne GPR measurements. Therefore, we investigate the measurement locations “Flooded gravel pit”, “Swimming pool” and “Pond”. Furthermore, we investigate whether Equation 3.42 can be used under field conditions to differentiate between the ratios of the intrinsic and scattering attenuation. We test this using a profile at the measurement location “Pond”, where the organic content in the water column due to leaves and branches of surrounding trees is increasing. For this purpose, the GPR data is spreading- and attenuation-corrected with the intrinsic attenuation coefficient. Then, the amplitudes of the lake bottom are picked and divided by A_0 along the profile to analyse the reflection coefficient of the lake bottom. Changes in the reflection coefficient should indicate the influence of scattering attenuation.

Maximum sounding depth

For estimating the maximum sounding depth, we need to relate the site-specific attenuation and spreading effects to the actual noise levels. An inspection of the field data shows that we find two sorts of noise in offshore GPR data: First, a coherent ringing occurring at all travel times that probably results from coupling the GPR antenna to a very low permittivity medium or from interaction between antenna and water vehicle or both (Type 1, water ringing, NC). Second, this is common, mostly random, electronic and environmental noise that increasingly dominates the record towards increasing travel times (Type 2, common noise, NR). However, the first factor in particular can be significantly reduced through appropriate processing (e.g. band pass filtering and background removal according to Section 3.3.1). For quantifying the mean achievable signal-to-noise ratios $(S/N)_{Mean}$, we compute the envelopes of the processed radargrams and from that form the quotient of the mean amplitude of a selected time window to the reference amplitude A_0 from Equation 3.36. Representative amplitudes N_C of the coherent noise (Type 1) are determined in a time window between the direct wave and lake bottom reflection, which is considered free of reflections, except in cases where scattering from floating organic particles is visible. Representative amplitudes N_R of the random noise (Type 2) are determined in a time window at the very end of the envelope traces. Then, the mean observed S/N ratio is

$$(S/N)_{Mean} = \frac{A_0^2}{N_{Mean}^2} \quad (3.43)$$

where $N_{mean} = mean\{N_C, N_R\}$.

The maximum ratio S/N_{Max} can be calculated analogously by N_{min} with $N_{min} = min\{N_C, N_R\}$. For estimating the maximum sounding depth z_{Max} , we assume vertical wave propagation, so $s = 2z$; and we define a threshold S/N ratio of 1 to be reached for reliable signal identification

$$(S/N)_{THR} = \frac{A^2(s = 2z_{Max})}{N_{Min}^2} = 1 \quad (3.44)$$

The maximum sounding depth can be estimated using the logarithmic expression 3.37 and considering

$$s_j = 2 \cdot z_{Max} \quad (3.45)$$

and

$$A = 1 \cdot N_{Min} \quad (3.46)$$

It follows that

$$\log(2 \cdot 1 \cdot z_{Max} N_{Min}) = [\log(s_0 A_0 R) + \alpha s_0] - 2\alpha z_{Max} \quad (3.47)$$

by solving it numerically or graphically for a reflection coefficient of $R = 1$. For the field examples the solution is found as the crossing point of the regression line from Equation 3.37, (right-hand side), and the function on the left-hand side of Equation 3.47. Since reflection coefficients may be $\ll 1$ we take a closer look at them in Section 3.4.4 and then reconsider the penetration depth issue in Section 3.5.1. The approach is applied at the measurement locations “Flooded gravel pit”, “Swimming pool” and “Pond” with different soil and water parameters.

The spatial resolution in field applications

To evaluate the spatial resolution of GPR measurements in water, we start by considering the common half-wavelength concept defining the subsurface volume, from which back-scattered signals would interfere constructively at the receiver. For the present GPR case, it has to be specified that the transmitter and receiver positions coincide (“zero-offset” case) and that “wavelength” may be understood as “wavelength at center-frequency”. This volume has a thickness of a quarter wavelength and a diameter of the 1st Fresnel zone. The radius l of the 1st Fresnel zone is given by

$$l = \sqrt{\frac{z\lambda}{2} + \frac{\lambda^2}{16}} \approx \frac{v}{2} \sqrt{\frac{t}{f}} \quad (3.48)$$

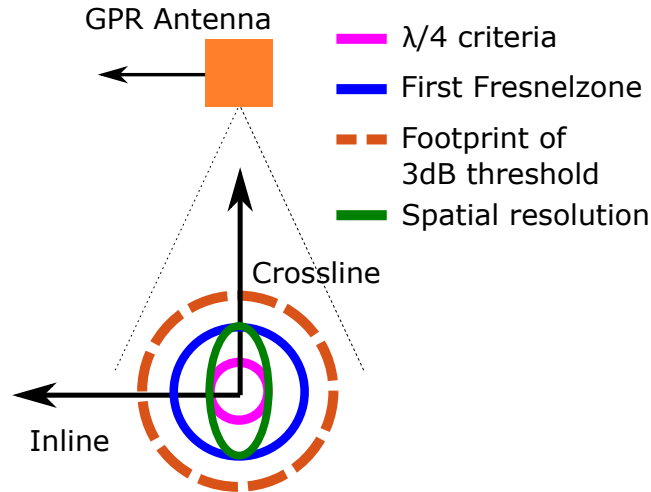


Figure 3.6: Schematic drawing of the resolvable areas (horizontal resolution) following from different criteria: 2D/3D survey without migration (1st Fresnel zone, blue), 3D survey after 3D migration (the $\frac{\lambda}{4}$ criterion, pink), 2D survey with inline migration only (green). In addition, the footprint estimated from the 3 dB threshold of the inline antenna radiation pattern is shown for water depths > 1 m (red dashed line).

where z is target depth, v is radar wave velocity, f is the center frequency of the signal, $\lambda = v/f$ is wavelength, and $t = 2z/v$ the two-way travel time (TWT) (e.g., (Schwamborn et al., 2002)).

Equation 3.48 does not include the effects of radiation patterns of the GPR antennae and possible improvement through digital processing, which we will address below. Still, it can be applied for basic estimates of resolution. However, for applying the equation to water surveys, one must take into account that the center frequency of the signal may be significantly reduced compared to the nominal antenna frequency due to the process of impedance loading (Kovacs, 1991). The reduction of center frequency may be 25% or more (Kovacs, 1991). For the antennae used in the present study, we found a center frequency reduction of 400 MHz to 300 MHz and of 200 MHz to 150 MHz. According to Equation 3.48, this effect leads to an increase of the radius of the 1st Fresnel zone and a reduction of resolution compared to measurements on land, where we have no frequency reduction. However, this shortcoming is overcompensated by the strong reduction of radar wave velocity in water ($\sim 3.4 \frac{\text{cm}}{\text{ns}}$) compared to soils on land (typically $\geq 7 \frac{\text{cm}}{\text{ns}}$ for sandy soils). Therefore, despite the frequency reduction, Fresnel zones can be expected to be about 1/3 or more smaller in water than on land, and the resolution accordingly better.

The Fresnel zone consideration applies to non-migrated zero-offset sections. Through digital migration (i.e., downward continuation of the receiver plain to $z = 0$), the resolution of GPR records can be improved up to the theoretical limit of $\lambda/4$ in both horizontal and vertical directions (Equation 3.48 for $z = 0$). However, for field conditions, $\lambda/3$ to $\lambda/2$ are more realistic estimates (Schwamborn et al., 2002). This is in

water 8 cm–11 cm for the 200 MHz antenna and 3 cm–6 cm for the 400 MHz antenna. As $\lambda = v/f$, the decrease of velocity and frequency in water compared to land act in the same way as outlined above.

If GPR data are acquired only along profile lines (“2D measurements”), migration can be performed only inline, too. In this case, the resolvable area is smaller inline than crossline. This situation is sketched in Figure 3.6 (green line) in comparison to the 1st Fresnel zone (blue line, no migration) and $\lambda/4$ criterion (pink line applying to 3D data after 3D migration). Areal 3D measurements, which would allow a 3D migration, can hardly be realized with a single antenna and DGPS positioning. For this, a fixed antenna grid would have to be built as described by Annan and Davis (1977).

So far, we have not considered changes of the width of the radiation pattern of the antenna when comparing land and water applications. The width of the downward directed radiation cone is strongly affected by the critical refraction angle at the air–water or air–soil interface at the antenna bottom. It is given by

$$\Psi = \sin^{-1} \left(\frac{1}{\epsilon_r^{\frac{1}{2}}} \right) \quad (3.49)$$

and changes from 6.5° for air–water to $>15^\circ$ for air–soil interfaces. Therefore, the application of GPR antennae at the water surface leads to a considerable focusing of the downward directed beam. In the context of this article, we want to investigate whether this smaller footprint of the antenna radiation pattern could improve the resolution. This would be the case if the downward directed coil was narrower than the cone of the 1st Fresnel zone.

Antenna radiation patterns are strongly dependent on the details of antenna construction. Therefore, we performed exemplary measurements under lab and field conditions and compared them to the subsurface far field solution for a dipole antenna placed on top of a dielectric half space. After (Smith, 1984), this radiation pattern is given by

$$E(\theta) = \omega^2 \mu_0 k_{12} p \cos(\theta) e^{-jk_2 h \sqrt{1 - k_{12}^2 \sin^2 \theta}} \times T_{\parallel} \frac{e^{-jk_1 r}}{4\pi r} \quad (3.50)$$

with

$$T_{\parallel} = T_{(12)} = \frac{2k_{21} \sqrt{k_{21}^2 - \sin^2 \theta}}{k_{21}^2 \cos \theta + \sqrt{k_{21}^2 - \sin^2 \theta}} \quad (3.51)$$

where ω is the radian frequency, μ_0 the magnetic permeability of the vacuum, k_1 is the wavenumber in water, k_2 is the wavenumber in air, $k_{21} = k_2/k_1$, $p = I \cdot dl$ (where I is

the current amplitude and dl the infinitesimal dipole element length). h is the electric dipole height above half-space and T_{\parallel} is the TM dielectric-air transmission coefficient, r is the distance from antenna to object, and θ is the angular offset.

For the calculation of the footprint l_2 , we use the angular aperture θ_{3dB} at which the radiated energy has decreased by half compared to the centre point, which is at the 3db threshold.

$$l_2 = \tan(\theta_{3dB}) \cdot h \quad (3.52)$$

where h is the water depth, and θ_{3dB} is the angular aperture at the 3dB threshold.

For measuring exemplary antenna radiation patterns, we sounded under water objects under varying radiation angles using a GSSI 400 MHz antenna. A lab-type experiment was conducted with an aluminum pipe lowered at the measurement location "Swimming pool". In a field experiment, we analyzed random objects found in the water column of the measurement location "Pond", most likely fishes. The processing applied consisted of spreading and attenuation correction. Then, the corrected amplitudes of the diffraction hyperbolas were picked and plotted versus the angular distance. The resulting E-field antenna patterns were then compared to the theoretical values from Equations 3.49 and 3.50. Coming back to the goal of evaluating the achievable spatial resolution, we determined the width of the amplitude spots resulting from migrated diffraction hyperbolas recorded with the 200 and 400 MHz antennas of GSSI. The "width" refers to the range where $amplitudes > \frac{maximum\ amplitudes}{e}$. We used diffraction hyperbolas of all measurement locations in different (water) depths. These values were then compared to the width of the footprints resulting from the antenna radiation pattern.

Material contrasts in field applications

To theoretically determine material contrasts, which can be expected during geophysical prospection of archaeological objects in water, we chose two reference materials: fresh water and water-saturated sand. For these two materials, we define their relative dielectric permittivities ϵ_{ref_water} and ϵ_{ref_sand} in Table 3.2 according to literature values.

For these reference materials, the reflection coefficients to

- a) Inorganic materials;
- b) Organic materials;
- c) Specific archaeological materials;

Material	Relative dielectric permittivity	Volumetric water content [vol%]
Fresh water	81	-
Saturated Sand	20	45

Table 3.2: Physical parameters of dielectric permittivity and volumetric water content of the reference materials freshwater and saturated sand based on data from Schön (1983) and Annan (2003).

are determined. We assume full water saturation for all materials and neglect effects of a varying water saturation of 60-100% in the lake bottom, which was determined in studies by Menounos (1997) and Avnimelech et al. (2001). In step a), we focus on clay-free, water-saturated rocks and determine their physical parameters ϵ_{rock} as a function of their volumetric water content θ instead of porosity Φ , because above a certain degree of porosity a suspension, rather than a porous solid, is obtained.

The CRIM equation of saturated state (Wyllie et al., 1956) applies here

$$\epsilon_{rock} = [(1 - \Phi) \cdot \sqrt{\epsilon_{matrix}} + \Phi \cdot \sqrt{\epsilon_{ref_water}}]^2 \quad (3.53)$$

where ϵ_{matrix} is the permittivity of the rock matrix, and ϵ_{ref_water} is that of the pore water. For the rock matrix material, quartz was chosen. Its physical parameters are defined based on literature values, as shown in Table 3.2.

From that, the TE reflection coefficients r_{ϵ_r} , neglecting the influence of the magnetic permeability and the electric resistivity on GPR reflectivity, are determined according to Schön (1983).

$$r_{\epsilon_r} = \frac{\sqrt{\epsilon_{ref}} - \sqrt{\epsilon_{mat}}}{\sqrt{\epsilon_{ref}} + \sqrt{\epsilon_{mat}}} \quad (3.54)$$

where ϵ_{ref} are the reference materials, and ϵ_{mat} are the target materials.

The determination of the relative dielectric permittivity of the inorganic material clay (as well as for step b), the organic materials peat and gyttia) is complex and not subject to the well-defined correlations as for clay-free rocks. Therefore, reference works usually refer to studies in which the material parameters are determined empirically based on in situ field measurements. Depending on their composition, the physical parameters of the materials can cover wide ranges of values. All values taken can be found in Table 3.3. In the last step c), two specific archaeological materials were chosen: wood and granite. Their material parameters are again taken from literature and can be found in Table 3.3.

Material	Relative dielectric permittivity	Volumetric water content [vol%]
Rock matrix (quartz)	4.2	<1
Clay	10-40	50-85
Peat	40-60	70-95
Gyttia	60-70	90-95
Wood	20-40	50-60
Granite	8-11	<2

Table 3.3: Physical parameters dielectric permittivity and volumetric water content of the reference materials of different target materials. The values are based on data from Schön (1983), Annan (2003), Corradini et al. (2020), Fediuk et al. (2020b) and Knödel et al. (2013).

3.4 Results

3.4.1 Attenuation effects

Table 3.4 shows the attenuation coefficients α determined from field data at three measurement locations using Equation 3.37. For two locations, the attenuation coefficients were also calculated using Equation 3.38 to 3.40 and are presented in Table 3.4. The direct comparison of the measured attenuation coefficients shows that there is a difference of a factor two for the attenuation coefficient between the “Pond”, which is the most conductive, and the “Flooded gravel pit”, which is the least conductive measurement location. Thus, noticeable differences in attenuation must also be considered in fresh water environments. The theoretical attenuation coefficients (Equations 3.38 to 3.40) agree quite well with the measured values (Equation 3.37). Possible deviations can be explained, for example, by measurement inaccuracies that affect Equation 3.37. However, it is noticeable that the frequency dependence given by Equations 3.38 to 3.40 (approx. 25% between the 200 MHz and the 400 MHz antenna) is not relevant for the field data.

For a better comparison of the theoretical frequency-dependent attenuation coefficient with the values from field data, the swimming pool measurement location was investigated in more detail, as shown in Figure 3.7. The theoretical attenuation coefficient with and without considering ϵ'' (blue and red line, respectively) was plotted against the measurement frequency. The values determined from measured data are shown in yellow bar graphs and are almost identical for both frequencies. The theoretical values considering ϵ'' are slightly below the measured values in the case of the 200 MHz and slightly above in the case of the 400 MHz antenna. Neglecting ϵ'' , however, has effects both for the 200 MHz and especially the 400 MHz antenna. On the one hand, the attenuation coefficient is not varying with frequency anymore. In addition, the theoretical attenuation coefficient is significantly lower: about 25% compared to the measured




Location		Attenuation	Attenuation	Attenuation	Attenuation
		(eq. 3.37) 400 MHz	(eq. 3.38-3.40) 400 MHz	(eq. 3.37) 200 MHz	(eq. 3.38-3.40) 200 MHz
Flooded gravel pit		1.75	1.9	2.02	1.1
Swimming pool		2.43	2.6	2.42	2.1
Pond		3.71	-	-	-

Table 3.4: Comparison of the attenuation coefficients for the measurement locations “Flooded gravel pit”, “Swimming pool” and “Pond”. They were determined based on field data using Equation 3.37 and additionally calculated with Equations 3.38 and 3.40.

data. A possible explanation for this could be that the temperature and conductivity measured at the surface of the swimming pool do not correspond to the average values of the water column.

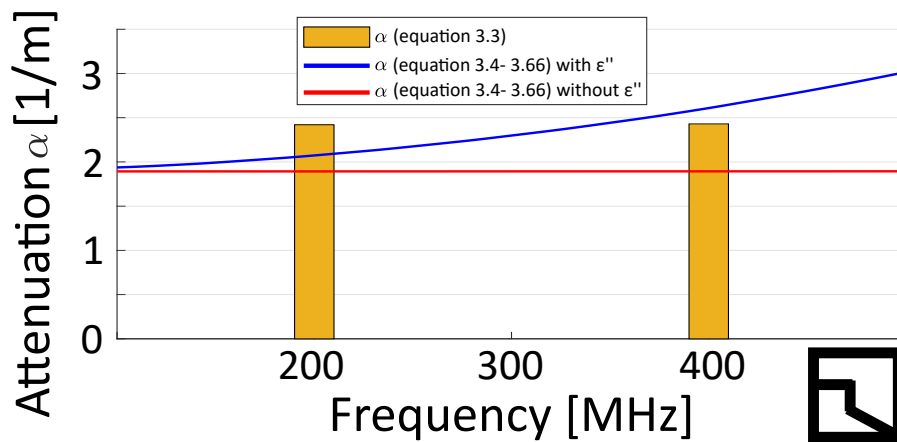


Figure 3.7: Comparison of the measured (yellow bar) and calculated attenuation coefficients (blue and red line) at the measurement location swimming pool (approx. 25 °C) for the 400 MHz and 200 MHz antennas. For the calculated attenuation coefficients, the imaginary part of permittivity is taken into account in one case (blue line) and neglected in the other (red line).

Now that the intrinsic attenuation has been determined, we move on to the contribution of scattering attenuation in the water column to GPR data and whether it can be determined from a radargram. For this purpose, we analyse a profile of the measurement location "Pond" with increasing organic material in the water column due to forest intrusion (see Section 3.2). Figure 3.8a shows, based on GPR data, the increasing organic material in the water column with profile length. For this purpose, the abso-

lute reflection amplitude was summed up from the water surface to the lake bottom (blue lines). This was repeated every 5 m along the profile. The proportion of reflection amplitudes in the water column increases significantly towards the end of the profile, where the greatest amount of organic material is also seen in the radargrams. Therefore, we establish here a relationship between the radar amplitude and the organic material. We neglect noise effects here, which would affect all traces equally..

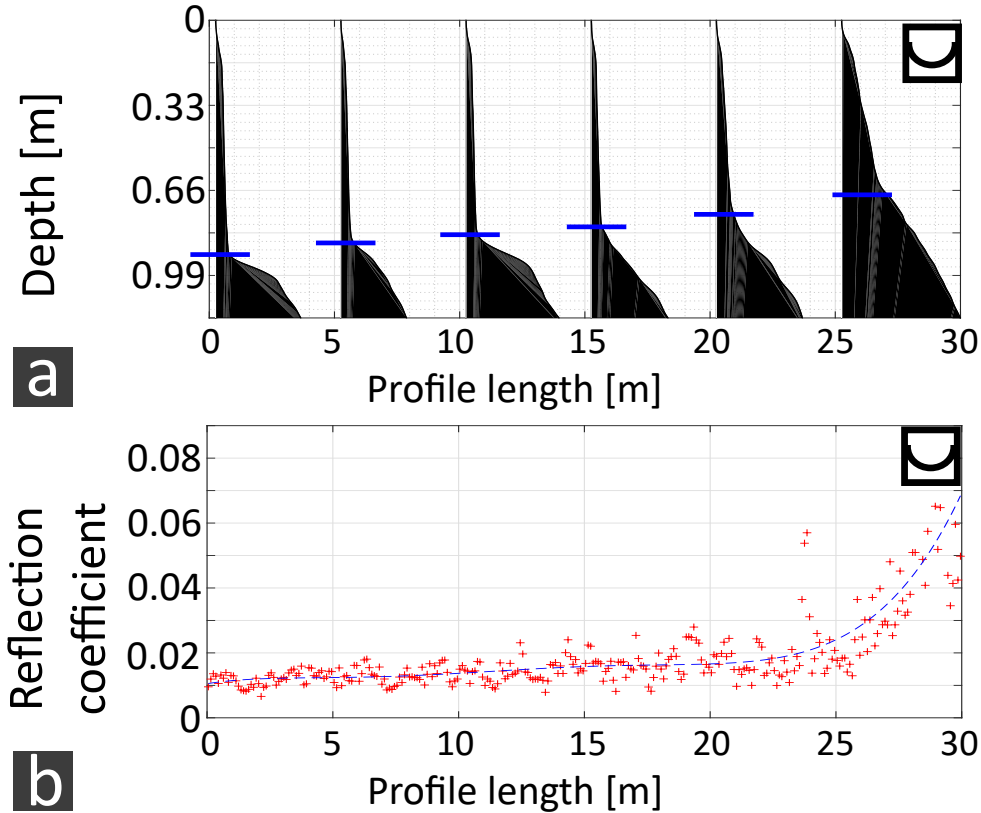


Figure 3.8: a) Amount of absolute reflection amplitude (summed up from the water surface to just below the lake bottom) at 5 m intervals along the profile at the measurement location "Pond", recorded with a 400 MHz antenna from GSSI. b) Plot of the reflection coefficient of the lake bottom along the profile.

For the evaluation of the lake bottom material, the reflection coefficient R along the profile is shown in Figure 3.8b. A significant amount of organic material in the water column, and thus of scattering attenuation, should reduce the reflection coefficient of the lake bottom, especially towards the end of the profile. In the first part of the profile, however, it scarcely changes, which indicates a homogeneous substrate, which might be gyttia due to the low reflection coefficient of 0.01 (compare with Section 3.4.4). Towards the end of the profile, R becomes more dispersive and increases up to 0.08. This indicates a material change, probably an increased amount of foliage/wood on the lake bottom (see Section 3.4.4), presumably in a weathered state. Consequently, even small changes in the reflection coefficient are more relevant than the negligible scattering





Location		S/N ratio	S/N ratio	S/N ratio	S/N ratio
		Type 1 400 MHz	Type 2 400 MHz	Type 1 200 MHz	Type 2 200 MHz
Flooded gravel pit		13 dB	38 dB	19 dB	27 dB
Swimming pool		17 dB	38 dB	20 dB	35 dB
River		33 dB	68 dB	39 dB	60 dB
Pond		33 dB	-	-	-

Table 3.5: Comparison of the mean GPR signal/noise ratio type 1 (water ringing) and type 2 (common noise) of processed data at the measurement locations “Pond”, “Swimming Pool”, “River” and “Flooded gravel pit” and the antenna frequencies 200 MHz and 400 MHz. The values are given in dB ($10 \cdot \log(S/N_{Mean})$).

attenuation. Thus, we can only differentiate intrinsic and scattering attenuation under optimal, e.g. laboratory conditions.

3.4.2 Maximum sounding depth

The mean signal/noise (S/N) ratio of type 1 (water ringing) and type 2 (common noise) at each location and for both antenna frequencies are summarized in Table 3.5. The following rule of thumb applies to both types of noise: The deeper the water column and the more turbulent the water (e.g. in the flooded gravel pit or due to swimming pool pumps, the lower the average S/N ratio of the water column. The “River” shows the best S/N ratio. The difference between the S/N ratio of type 1 in the water column and the S/N ratio of type 2 at the end of the trace is apparent at all measurement locations. Their difference ranges from a factor of 10 to 100. The S/N ratio type 1 is characterised by the “ringing” of both antennas in the water column. This affects the 400 MHz antenna more than the 200 MHz antenna. The S/N ratio type 2 (common noise) at the end of the radar traces, however, is slightly higher for the 400 MHz antenna than for the 200 MHz antenna. Thus, the penetration depth will be about the same for both antenna frequencies, but in particular the data quality will be worse in the water column for the 400 MHz antenna than for the 200 MHz antenna. The conclusions are consistent with the observations from the radargrams.

For the maximum S/N ratio, the tendencies of the average S/N ratio are mostly confirmed. The order of magnitude is 10^7 for type 1 and 10^8 for type 2. This is used to determine the maximum penetration depth in the second step. For this purpose, the left term of Equation 3.47 is used, in which the penetration depth is taken into account in addition to the maximum S/N ratio of types 1 and 2. To avoid confusion

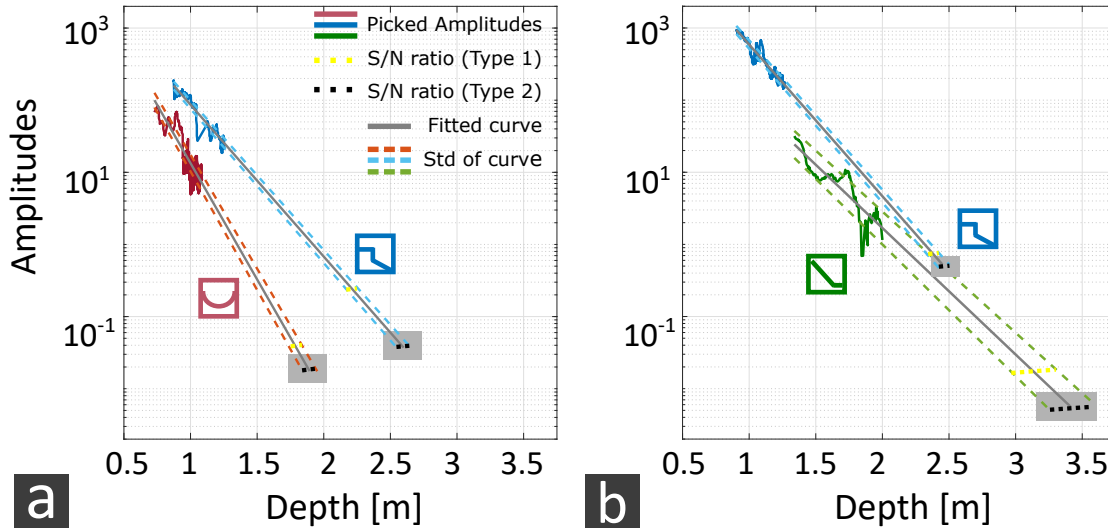


Figure 3.9: Determination of the maximum penetration depth and its standard deviation (grey shading) for three measurement locations. The maximum penetration depth is defined as the intersection of the exponential fitted curve (grey solid line) through picked amplitude values with depth (coloured solid lines) and of the maximum noise level for type 1 and 2 (dotted lines). The “Swimming pool” (blue line), “Pond” (red line) and “Flooded gravel pit” (green line) are distinguished. The standard deviation of the maximum penetration depth is defined as the intersection of the deviation of the fitted exponential curve (dashed lines) and of the respective noise level. A distinction is made between a) the 400 MHz antenna and b) the 200 MHz antenna from GSSI.

with the S/N ratio from Table 3.5, we use the term "noise level" for the left term of Equation 3.47. The results can be seen in Figure 3.9, where the spreading-corrected and picked amplitudes from the horizons are plotted against the depth. Results are available for the measurement locations “Pond” (red), “Swimming pool” (blue) and “Flooded gravel pit” (green). The 400 MHz (Figure 3.9a) and the 200 MHz antennas (Figure 3.9b) are differentiated. The penetration depth is defined as the intersection of the fitted curve with the dotted lines of the respective noise level. The noise level type 1 is coloured yellow, the noise level type 2 is coloured black. The highest penetration depth is achieved for type 2. The dashed lines mark the standard deviation of the fitted exponential curves. The standard deviation of the maximum depth penetration is defined as the difference of the intersections of the noise level with both dashed lines. Both the maximum depth penetration and its standard deviation are shaded grey in the image. The parameters of the fitted curves $[\log(s_0 A_0 R) + \alpha s_0]$ and $-\alpha \cdot 2$, as well as the maximum achieved depth penetration and its standard deviation, are listed in Table 3.6.

The approach worked especially well for the "Pond" and the "Swimming pool", as only very small standard deviations of 0.06 m were obtained for the depth penetration. The





Location		$\log(s_0 A_0 R) + \alpha s_0$	$-\alpha \cdot 2$	Max. depth penetration [m]	Std. of depth penetration [m]
400 MHz					
Pond		10	-7.4	1.9	0.06
Swimming pool		9.3	-4.8	2.6	0.05
200 MHz					
Swimming pool		11.2	-4.8	2.5	0.06
Flooded gravel pit		8.6	-4	3.5	0.18

Table 3.6: Comparison of the constant parameter $[\log(s_0 A_0 R) + \alpha s_0]$ (impact of the reflection coefficient and the antenna parameters on the depth penetration) and of the attenuation α , as well as of the maximum depth penetration and its standard deviation, for the 200 MHz and 400 MHz antennas from GSSI calculated from GPR profiles at three measurement locations.

flooded gravel pit, however, shows larger deviations of 0.18 m. This might be due to an increased noise level or a change of the reflection coefficient at the sub-bottom. All in all, penetration depths of 1.8 m–3.5 m, determined from the maximum S/N ratio of Type 2, were achieved, depending on the measurement site for the 200 MHz and 400 MHz antenna. In a visual comparison with the radargrams of Section 3.2, the results agree quite well, since both antenna frequencies of 200 MHz and 400 MHz show penetration depths of 2 m–4 m, depending on the type of reflectors. At the measurement location "Pond", reflections can be seen up to approx. 1.6 m, which is slightly less than determined in Figure 3.9 (1.8 m). This may be due to changing parameters below the lake bottom, which additionally decrease the depth of penetration. For the measurement location "Flooded gravel pit", reflections can be optically tracked up to 4 m, which is slightly further than the penetration depth of 3.5 m determined in Figure 3.9. In the case of measurement location "River", multiples due to the very shallow water depth and the strong bottom reflector affect the radargrams.

The results show that the attenuation has the highest influence on the penetration depth. A γ factor of 2 in the conductivity of freshwater at the measurement locations "Pond" and "Flooded gravel pit" show a difference in the penetration depth by a factor of 1.5. The measurement location "Swimming pool" demonstrates that the antenna frequency has negligible influence on the penetration depth. The attenuation coefficients are almost the same for both frequencies in this example. The S/N ratio is slightly better for the 400 MHz at the end of the trace than for the 200 MHz antenna. On the other hand, the constant b , consisting of the specific antenna parameters as well as the reflection coefficients and depths, which are the same for both frequencies, is slightly

better for the 200 MHz antenna than for the 400 MHz antenna. Thus, in this particular situation, the penetration depth is not crucial in the choice of antenna frequency. Rather, attention must be paid to the data quality in the water column, since ringing effects, especially with the 400 MHz antenna, must be expected at water depths >2 m. The spatial resolution also has an important impact on antenna choice, which will be investigated in the next Section.

3.4.3 Spatial resolution

In Figure 3.10, we first compare the theoretical spatial resolution using the Fresnel zone width (blue line) and the 3 dB threshold of the antenna radiation pattern (red line). It is noticeable that at shallow water depths <1 m, the footprint of the antenna radiation pattern is smaller than that of the Fresnel zone. Here, an improvement of the horizontal resolution would be possible due to the antenna radiation pattern. At larger water depths >1 m, the distribution is reversed.

The horizontal resolution values determined from the width of migrated diffraction hyperbolas are shown as black points in Figure 3.10, too. Regardless of the measurement location and the antenna frequency, this data can be fitted through the following relation (green line):

$$l_{measured} = \sqrt{target\ depth \cdot \lambda} \quad (3.55)$$

The fitting curve (green) is parallel to the line showing the width of the Fresnel zone (blue), so the horizontal resolution obtained in the field is lower than expected from the Fresnel-zone-based estimate. In addition, it seems to be independent from the footprint of the antenna radiation pattern. The intersection point between this curve and the 3dB threshold of the antenna radiation pattern is at a water depth of 1.10 m for the 400 MHz antenna.

A comparison of the theoretical antenna radiation pattern with the radiation pattern of the 400 MHz from GSSI measured at locations "Pond" and "Swimming pool" is shown in Figure 3.11. The antenna pattern and the radiation angle at the 3dB threshold are almost identical to those of the far field solution for a dipole (Equations 3.50 and 3.51). Only the critical angle cannot be defined with certainty, so it must be assumed that near- and far-field components are superimposed.

Figure 3.12 shows, for the 400 MHz antenna, how the 30 cm wide pool steps (green circle) of the "Swimming pool" were used to determine the horizontal resolution in inline direction under field conditions shown in Figure 3.10. For this purpose, the width of the envelope of the migrated and unmigrated measurement data was compared. Figure 3.12 (a,c) shows the radargrams, and Figure 3.12(b,c) the envelopes of the data. The data from Figure 3.12(a-b) is unmigrated, while that of Figure 3.12(c-d) migrated. In our example, the width of the lowest step is 33 cm for the migrated data and 40 cm for the unmigrated data. For the migrated data, the deviation is therefore 3 cm from

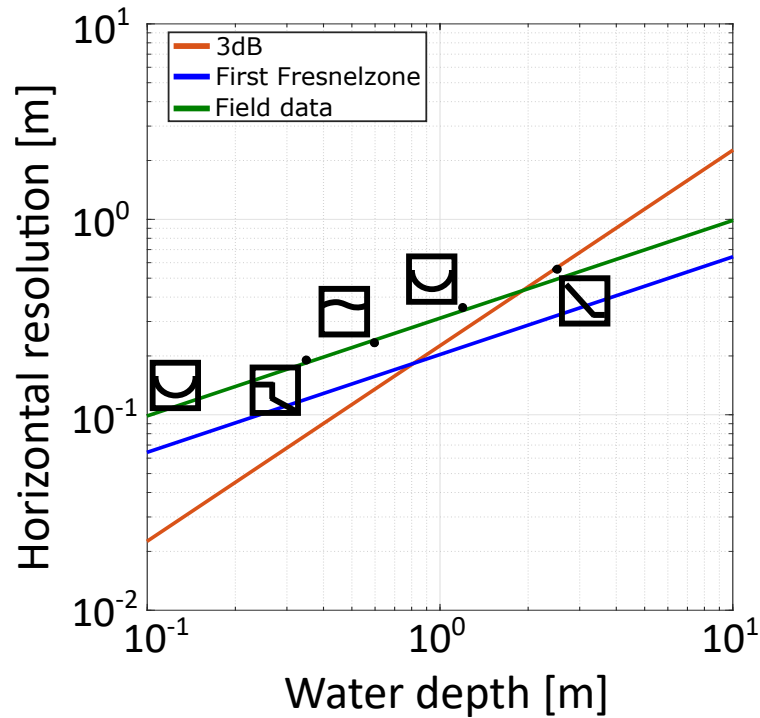


Figure 3.10: Comparison of the horizontal resolution vs. the water depth based on the footprints of the first Fresnel zone (blue) and of the 3dB threshold of the antenna radiation pattern (red). Furthermore, the horizontal resolution under field conditions was determined (black dots) and fitted (green) based on the width of migrated diffraction hyperbolas in different water depths.

the steps and thus within the vertical resolution ($\frac{\lambda}{3}$). For the non-migrated data, the deviation is 10 cm to the steps and thus slightly better than the resolution according to the Fresnel criterion (see Figure 3.10).

From our results, we can conclude that the Fresnel zone width is a robust estimate resolution under field conditions. The predicted effect of the narrowing of the antenna radiation pattern for water applications could be verified, but it does not seem to lead to an improvement of the spatial resolution of the reflection images at shallow target depth <1 m. This might be caused by the near-field component of the antenna radiation pattern, which we did not consider in our investigations

To further improve the horizontal resolution to that of the vertical resolution in the centimeter range, a 3D radar survey would have to be conducted using antenna arrays. This is because the precise positioning of single antennas with a cruising boat is difficult for larger survey areas but a precondition for gaining resolution increase through 3D migration. Another option would be to build a fixed coordinate system, as done by Leckebusch (1998), with ropes and wooden slats in the water.

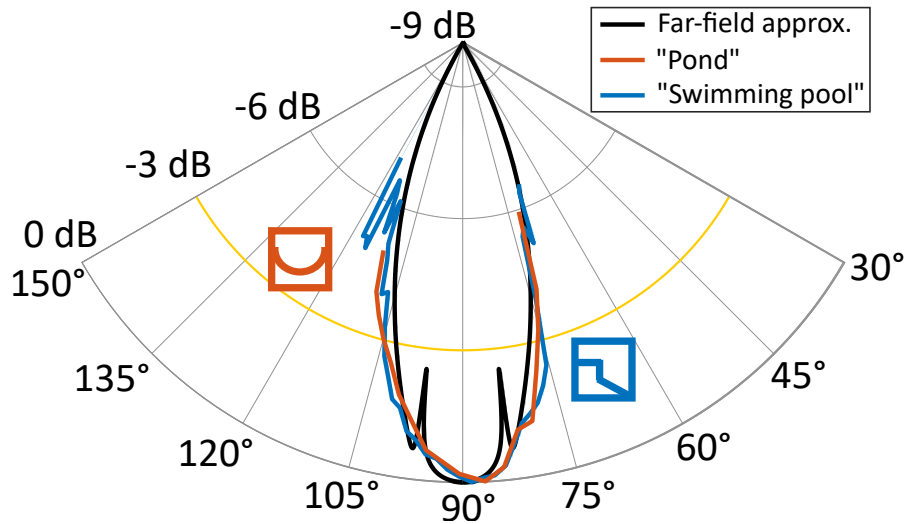


Figure 3.11: Comparison of directivity functions from far-field approximations, E-plane, air-water interface (black line), as well as from the experimental estimate at the measurement locations “Pool” (blue line) and “Pond” (red line). The 400 MHz antenna from GSSI was used.

3.4.4 Material contrasts in field applications

Figure 3.13 shows the physical parameter relative permittivity as a function of the volumetric water content. Note that 0 vol% volumetric water content represents the rock matrix, and 100 vol% volumetric water content the fresh water (assuming full saturation). At the bottom of lakes, a layer of mud (that is, a layer of suspended organic or non-organic material) may form, which may show a gradual increase or a stratification in density with depth. Suspensions show a volumetric water content larger than a critical value that causes material fragments or grains to be completely surrounded by fluid such that they lose their mechanical stiffness (e.g., Mavko et al. (2020)). A typical order of magnitude of critical water content is 50% for sandy grain size (e.g., Mavko et al. (2020)). At the lake bottom, a stratification of different stages of the suspension could possibly occur. The curve of the relative permittivity (Figure 3.13) increases with increasing volumetric water content from the value of the rock matrix to the value of the freshwater. Figure 13 is required for the determination of the reflection coefficients in the next section.

Figure 3.14a shows the GPR reflection coefficients R from the reference material freshwater to various other subsurface materials, calculated according to Tables 3.2-3.3. Figure 3.14b analogously shows the reflection coefficients of the reference material water-saturated sand to other subsurface materials. The lines show the material contrasts of the reference materials to clay-free rocks depending on their volumetric water content. The dashed line corresponds to a negative reflection coefficient, the solid lines to a positive reflection coefficient. In Figure 3.14a, the reflection coefficients approach zero with increasing volumetric water content. In general, the method provides useful contrasts, which we define as $R > 0.1$, between freshwater and the materials granite,

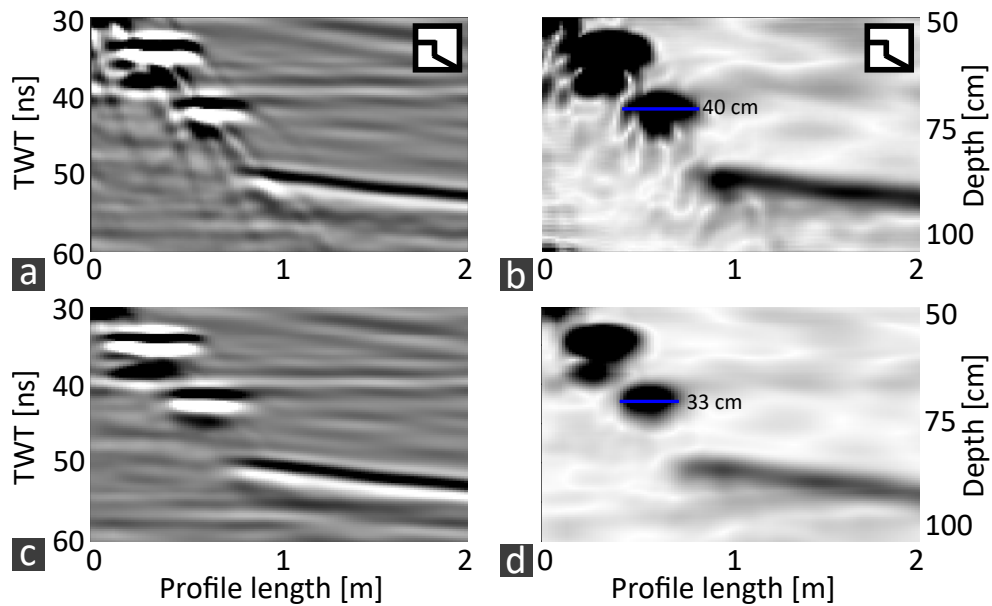


Figure 3.12: a)-b) Unmigrated and c)-d) migrated GPR signal (a,c) and envelope (b,d) of steps from the measurement location “Swimming pool”. The 400 MHz from GSSI with the registration unit SIR 4000 was used.

sand, clay, and wood. However, the reflection coefficients of the organic materials peat and gytija are low, especially for gytija R is smaller than 0.1, and slightly better for peat. For the reference material water-saturated sand (Figure 3.14b), the method generally shows large reflection coefficients again. The contrasts to clay-free rocks decrease for medium porosities and increase for low and high porosities. The zero transition then corresponds to the physical parameters of our defined water-saturated sand. The contrasts of water-saturated sand with the materials gytija and granite are >0.1 . In addition to the detectability due to a high enough contrast, another aspect is the differentiation between different materials, such as wood, clay, and peat, which can be difficult with GPR.

Table 3.7 summarises the results of the reflection coefficients between all materials shown in Figure 3.14. Here, material contrasts with absolute values of the reflection coefficient $|R| > 0.1$ show a check mark. Parenthesized checkmarks indicate the material contrasts whose absolute value of R is possibly <0.1 . Methods whose absolute value of R is always <0.1 show a cross in the table. The table shows that most material contrasts can be sufficiently resolved with GPR (e.g., sand, peat, wood, and gytija to granite, as well as wood and sand to gytija). GPR shows its largest deficits in the differentiation of peat, gytija, and wood, that is, all organic materials.

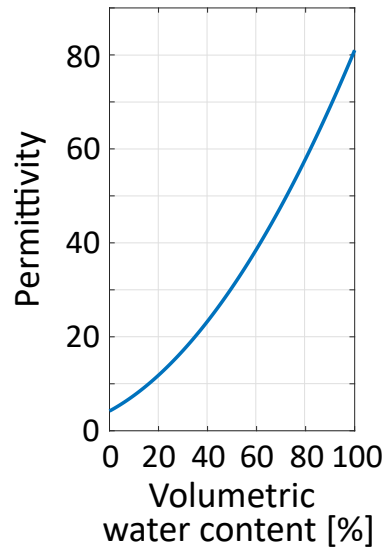


Figure 3.13: The physical parameter of relative permittivity (based on the CRIM formula) is shown as a function of the volumetric water content.

3.5 Discussion

3.5.1 Maximum Sounding Depth

The average depth penetration we determined from all measurement locations was 2 m–2.6 m for the 400 MHz antenna and 2.5 m–3.5 m for the 200 MHz antenna for water conductivities of $0.04 \frac{\text{S}}{\text{m}}$ – $0.09 \frac{\text{S}}{\text{m}}$. Our results are in good agreement with previous GPR studies in freshwater. For the 200 MHz antenna, Ruffell (2006) achieved a penetration depth of 4 m, Shields et al. (2004) a penetration depth of 4 m–5 m and Jol and Albrecht (2004) a penetration depth of 3 m, while Park et al. (2004) achieved a penetration depth of 4 m with the 400 MHz antenna before lowering it to the bottom to prospect even deeper targets. In all studies, no specific conductivity data was provided. Arcone et al. (2010) achieved a remarkable high depth penetration of 6 m–8 m with a very low conductivity of $0.004 \frac{\text{S}}{\text{m}}$ when using a 200 MHz antenna. Finally, lowering the antenna to the bottom can increase the depth penetration to the values above plus the thickness of the water column. Studies of Park et al. (2004) demonstrated this successfully.

In our study, we found that if only the conductivity but not the imaginary part of the permittivity ϵ'' is considered, the theoretical attenuation coefficient is reduced by approx. 25% compared to measured values. In other studies, which also calculated the attenuation coefficient based on reflection amplitudes as well as on conductivity measurements, excluding ϵ'' , different results were found. For example, Sambuelli et al. (2009) observed a very small error of 2% between the fitted and the calculated attenuation coefficient. In a study by Lin et al. (2010), the value of the fitted attenuation coefficient was even lower than the calculated value. The various results show that punctual conductivity measurements in the water column may not indicate its

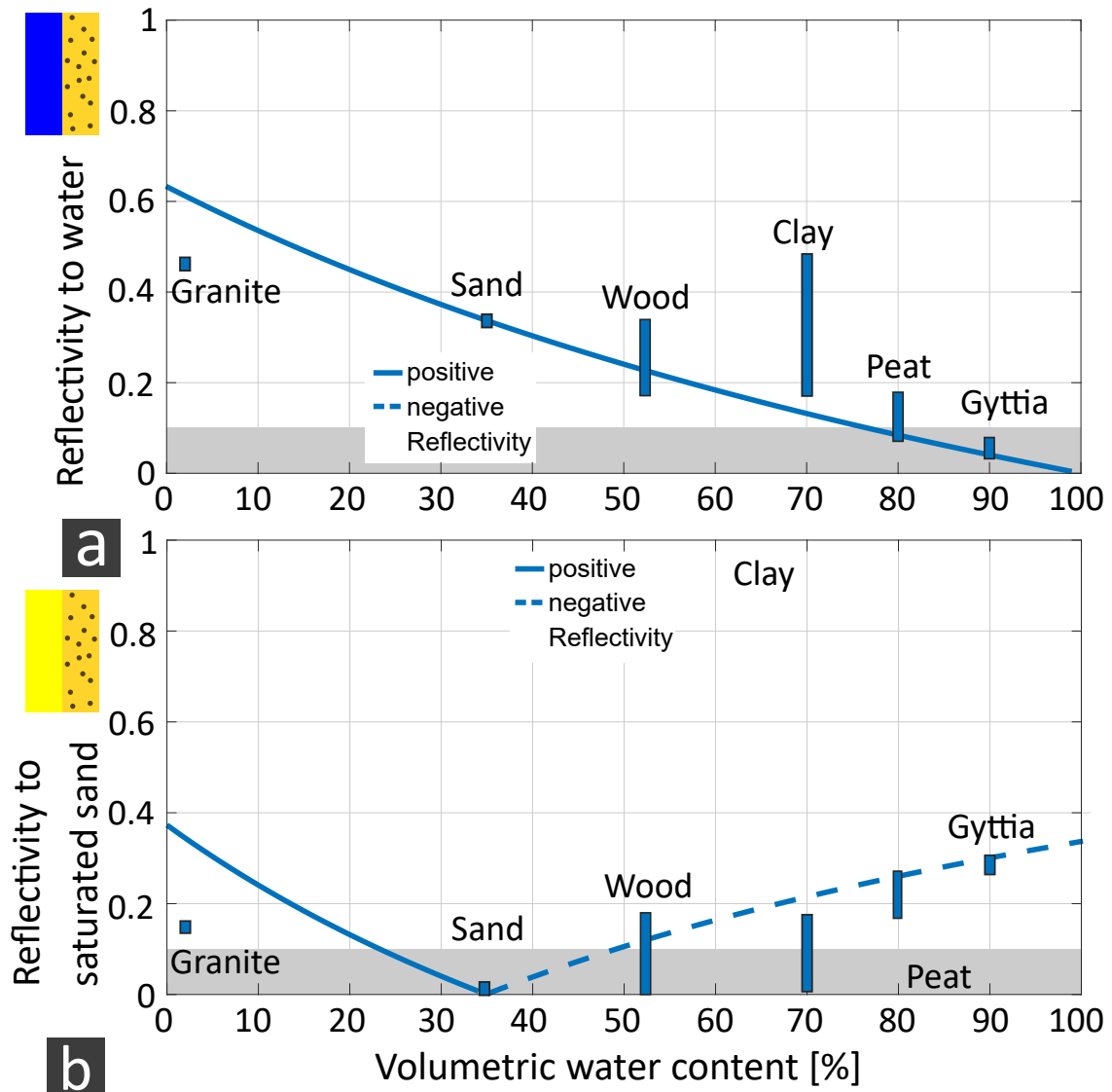


Figure 3.14: Absolute values of negative (dashed line) and positive (solid line) GPR reflection coefficients. The reference materials a) freshwater and b) water-saturated sand are distinguished. Their material contrast to clay-free rocks of various porosities is shown in the form of lines. In addition, their contrast with various other (in)organic and archaeological materials such as clay, granite, wood, sand, bricks, peat and gyttia is presented as bars. The values are calculated according to Tables 3.2-3.3.

average.

Our approach assumed a reflection coefficient of $R = 1$. As shown in Sections 3.4.2 and 3.4.4, however, many reflection coefficients are significantly lower and range between $|R| = 0.1$ and $|R| = 0.5$. For a well-resolvable reflection coefficient of $R = 0.1$, the penetration depth would be reduced by 16% and 18%, which is 0.3 m and 0.45 m for the 400 MHz and 200 MHz antennas, respectively.

	Fresh water	Sand	Clay	Peat	Gyttia	Wood	Granite
Fresh water		✓	✓	(✓)	×	✓	✓
Sand			(✓)	✓	✓	(✓)	✓
Clay				(✓)	✓	(✓)	(✓)
Peat					(✓)	(✓)	✓
Gyttia						✓	✓
Wood							✓

Table 3.7: The suitability of GPR for resolving contrasts between the materials fresh-water, sand, clay, peat, gyttja, wood and granite. Material contrasts of $|R| > 0.1$ labeled with a check mark. When it might be that $|R| < 0.1$, the checkmarks are parenthesised. Material contrasts of $|R| < 0.1$ show a cross.

In our chosen method for determining the penetration depth, the various soil, antenna, and water parameters do not have to be known. In addition, this is the only approach that takes into account the noise level and thus the field conditions. A very similar approach was applied by Annan et al. (1977) by using the radar range equation. In this case, all antenna and target parameters were known. An alternative concept has been found by Sellmann et al. (1992), in which for unknown target and system parameters, the maximum possible relative amplitude decrease is estimated. The value is determined from a recorded trace in the field and its maximum depth penetration. The number of attenuation components in this range (geometrical spreading, water and sediment conductivity, and layer thickness, as well as reflection coefficients from the water-sediment interface) are estimated and added up. This maximum amplitude decrease can now be used to determine the depth penetration in other subsurface scenarios. In contrast to our study, this approach also takes into account the parameters of the lake bottom and not only the water column up to the lake bottom and not only the water column up to the lake bottom.

Our study shows that the choice of antenna frequency of 200 MHz or 400 MHz does not affect the depth penetration much. In critical conditions, the choice of a 200 MHz antenna is certainly appropriate, but the antenna ringing and thus the noise level and the data quality in the water column also play an important role. Our experience is that for water depths of 2 m and more, the data quality of the 400 MHz antenna becomes very poor, and the 200 MHz antenna provides much more reliable values. Similar experiences were reported by Ruffell (2006), who found that for water depths deeper than 6 m, and for all antenna frequencies (100 MHz–400 MHz), the antenna ringing was too large for successful investigations. He did not use the 400 MHz antenna at all because, as in our case, the ringing for the 400 MHz antenna became large at a water depth of 2 m and more, but the data information content was hardly better than with

the 200 MHz antenna. Here, we had different experiences, especially in the resolution of objects (see Sections 3.3.2 and 3.4.3). At shallow water depths, the reflection amplitudes are significantly sharper with the 400 MHz antenna than with the 200 MHz antenna. Moreover, other studies were able to perform GPR measurements in water depths of more than 6 m (Arcone et al., 2010). However, the study of [53] observed antenna ringing with both 200 MHz and 500 MHz antennas. We have also made good experiences in reducing antenna ringing with trace averaging and low pass filtering (see Section 3.3.1), which has also been confirmed by Moorman and Michel (1997) and Porsani et al. (2005). Another improvement in data quality that we also noticed in our study was the stacking of GPR traces (16 times). Positive experiences were also reported by Moorman and Michel (1997) and Porsani et al. (2005) with 32 times stacking.

Regarding organic material in the water column, Kovacs (1991) and Shields et al. (2004) have also found that it has little or no effect on the penetration depth of GPR in the water.

3.5.2 Spatial resolution and antenna directivity

In our study, we were able to achieve spatial resolution in the centimeter range in the horizontal and vertical directions and to resolve branches and fish. It basically follows the curve of the 1st Fresnel zone width. We could verify the theoretically predicted radiation pattern and its narrowing in water compared to land applications. However, a corresponding positive effect on the resolution could not be recognized. Due to the narrow beam, however, fewer side reflections might be expected. Similar experiences were made in other studies when resolving objects. Among other things, Leckebusch (1998) was able to resolve reeds and dirt particles, while Ruffell (2014) was able to resolve a beverage can with the 200 MHz antenna, Jol and Albrecht (2004) found tree trunks of various diameters, and Arcone et al. (2010), achieved a vertical resolution of <20 cm for the 400 MHz antenna and of <30 cm for the 200 MHz.

The question on how exactly the depth of the lake bottom can be determined was answered by Moorman and Michel (1997). The bathymetry was determined with 3% and the sediment thickness with 15% precision. In each case, errors in the velocity assumption of the radar waves in the water column and the lake bottom were considered. Kovacs (1991) discussed the antenna beam footprint due to the critical angle regardless of the antenna frequency. He made a rule of thumb for water depths <5 m, for which a footprint diameter of $0.2 \cdot \text{water depth}$ can be assumed. To achieve a minimal footprint, the antenna would have to be raised above the water, but this would significantly reduce the energy transmitted into the water.

First Sellmann et al. (1992) and a little later Arcone (1995) presented a detailed investigation of the antenna radiation characteristics in water. Here, the the steady-state, subsurface far field solution for an interfacial infinitesimal dipole of Smith (1984), was used. It was compared to those of a transient, finite-size, resistively loaded array (50 MHz). Their experience was that the second approach was more accurate and

resulted in an even narrower antenna radiation pattern. They also calculated the footprints in different water depths for a 50 MHz antenna. In addition, a comparison was made between a theoretically calculated and a practically determined antenna radiation characteristic of a 200 MHz antenna. These were in good agreement. In addition, Wensink et al. (1990) investigated, both theoretically and practically, the antenna radiation characteristics of a 200 MHz antenna in tank experiments at different depths up to 2.5 m. The height of the antenna above the water column was also varied. Their outcome was that far-field conditions have not fully developed at a depth of about 2.5 m, which also agrees with our experience. Our measurements do not confirm the observation of Wensink et al. (1990) that better agreements between theory and practice could be achieved by raising the antenna to higher levels above the water surface.

3.5.3 Material contrasts

Our results show that a range of archaeological material contrasts can be resolved with GPR (e.g. stone and wood). This is also confirmed by numerous other studies. Abramov and Vasiliev (2004) were able to detect wall foundations, partly of stone and partly of clay, in the sandy subsoil of the Black Sea. Leckebusch (1998) detected the archaeological layer of a former settlement, while Jol and Albrecht (2004) and Arcone et al. (2010) found logs in sandy and gravelly soil. High contrasts between sand and metal were also detected by Arcone et al. (2010). However, some material contrasts, although apparently sufficient, cannot be resolved. With Leckebusch (1998), the dielectric permittivities of an archaeological layer, wooden poles, and lacustrine chalk were determined using TDR measurements. Although there was a sufficient difference in permittivity between the lacustrine chalk and wooden beams, this material contrast could not be resolved. This was justified by the possible influence of magnetic permeability.

A direct address of the material is hardly possible with the method. Sambuelli et al. (2009) attempted to calibrate reflected bottom amplitudes using samples and TDR measurements. However, this did not succeed and was explained by the size of the subsoil materials (e.g. pebbles). Their size is approximately in the range of the wavelength of the GPR antenna, so that Mie scattering rather than Rayleigh scattering is to be expected here. Mie scattering is hardly correctable and changes the reflection amplitudes. A better result was achieved by Lin et al. (2010), who compared reflection amplitudes of unknown sub-bottom materials to known metal plates using both GPR and seismic methods. They were able to determine reflection coefficients and to draw conclusions on the sediment porosity. Finally, a material identification was successful using a joint inversion of the two methods. Other techniques were used by Arcone et al. (2010) to obtain information on the subsurface materials. To distinguish wood from metal, their wavelet shape was intensively compared. In addition, the permittivity of the materials was calculated from diffraction hyperbolas in the subsurface. In addition, TDR measurements (Arcone et al., 2008) were compared with the CRIM equation (Wyllie et al., 1956) and studies on the water content of lake sediments (Menounos, 1997).

In general, GPR measurements should be verified with the help of samples, drillings, TDR measurements, and, for example, the comparison of trace signatures. To exclude ambiguities, a second geophysical method can also be used, as with Lin et al. (2010). GPR measurements, on the other hand, can also be used to exclude ambiguities in seismic and geoelectric measurements. Furthermore, for critical material contrasts such as water-clay, wood-clay and sand-peat, they may even achieve better results than the other two methods. Our experiences from the study also show that GPR in water offers several more fields of application. The exemplary location "Pond" shows that GPR could be used to determine the biomass and thus the siltation of lakes and rivers. For this, the next step would be to quantify the organic mass in the water and calibrate the results with the radargrams. Possible scattering effects would have to be considered.

3.6 Conclusion

In our study, we gained experience with GPR measurements at four different survey locations in order to generate rules of thumb for the further application of GPR for archaeological prospection in terms of penetration depth, resolution and material contrasts. Due to the limitations of depth penetration, with 200 MHz and 400 MHz antennas floating on the water surface, GPR is only suitable for <3 m–6 m shallow freshwater, but can complement the common geophysical methods in water (i.e. seismics and geoelectrics), especially in order to exclude ambiguities. The advantage compared to the traditional methods is the easy application of the onshore equipment in water, for which, in the simplest case, only a waterproof box is needed. The high resolution is in the cm range in the direction of the profile and in the dm range across the profile. The narrow antenna radiation pattern in water cannot further improve the resolution across the profile, but we expect fewer side reflections than on land. Many archaeologically relevant material contrasts can be resolved, including sand/stone and gyttia/wood. The material contrasts sand/clay and water/gyttia are possibly not distinguishable. The depth penetration is hardly influenced by the choice of the antenna frequency of 200 MHz or 400 MHz. Organic material in the water column also has no significant effect on penetration depth. Instead, this offers a new field of application for the method, which can potentially be used to study the siltation of lakes. The influence of the water column on the GPR antenna designed for onshore measurements appears especially in the form of antenna ringing for the 400 MHz antenna in water depths >2 m, reducing its data quality. In addition, multiples must be expected in water depths of <0.5 m. A stable GPR signal was mostly only achieved by 32 times stacking. To reduce the depth penetration limitations of the water column, the antenna could be lowered. However, the effort of lowering the antenna removes the advantage of the simple application of the land equipment in the water compared to other methods.

Author Contributions Conceptualization, A.F. and W.R.; methodology, A.F., T.W., D.W., W.R.; software, A.F., T.W.; validation, T.W., D.W. and W.R.; formal analysis, A.F.; investigation, A.F.; resources, A.F.; data curation, A.F.; writing—original draft prepara-

tion, A.F.; writing—review and editing, T.W., D.W., W.R.; visualization, A.F.; supervision, T.W., D.W., W.R.; project administration, W.R.; funding acquisition, T.W., D.W., W.R. All authors have read and agreed to the published version of the manuscript.

Funding The research leading to these results has received funding by the German Research Foundation (DFG) in a project (RA 496/26-2) situated in the frame of the Priority Program 1630 ‘Harbours from the Roman Period to the Middle Ages’ (of Carnap-Bornheim and Kalmring 2011).

Acknowledgements Special thanks are dedicated to the Karlsgraben survey team from 2017 and the team joining the swimming pool experiments. The authors also acknowledge support from Detlef Wolters from the swimming hall of the Christian-Albrechts-University of Kiel. We gratefully acknowledge Clemens Mohr for his work on the GPR acquisition system. The GPR data was processed and analysed with the program Matlab.

Conflicts of Interest The authors declare no conflict of interest. The funders had no role in the design of the study; in the collection, analyses, or interpretation of data; in the writing of the manuscript, or in the de-cision to publish the results.

4 Physical Parameters and Contrasts of Wooden Objects in Lacustrine Environment: Ground Penetrating Radar and Geoelectrics

Abstract We investigate how suitable ground penetrating radar (GPR) and geoelectrics are to prospect the remains of submerged wooden archaeological constructions in the water column. For this purpose, we determined the contrasts of electric resistivity and dielectric permittivity from measurements on present-day wood samples, serving as simplified approximations of water saturated and undegraded archaeological wood. As common substitutes of hard and soft construction wood, we investigated oak and spruce wood. The electric resistivity and dielectric permittivity were determined with increasing moisture content from small-scale electric and GPR measurements using a Wenner α array and a 2 GHz Palm antenna in a watering experiment. In a water-saturated state, resistivity values of $<270 \Omega\text{m}$ and relative dielectric permittivity values of >20 were observed. The anisotropy effects and deviations of the wood species were seen to be up to 30%. On the basis of this, the relative material contrasts of wood with respect to fresh water, sand, and clay were calculated and compared to values found in the literature for seismic contrasts. Geoelectric, GPR, and seismic measurements show contrasts of 0.3 to 0.8, -0.4 to 0.2, and -0.24 to 0.35, depending on the surrounding material and structural orientation of the wood. The highest contrasts were found for wood in fresh water, followed by clayey and sandy subsoils. On the basis of the determined contrasts, analytical calculations were performed showing that an object of 0.5 m diameter can be detected at depths between 0.5 m and 1.5 m with geoelectrics (Schlumberger) and at depths between 0.5 m and 3 m with ground penetrating radar measurements (400 MHz).

4.1 Introduction

In recent years, the geophysical prospection of archaeological targets has been extended to amphibious terrains and shallow water environments. Current research issues include prospecting anthropogenic harbor installations (Müller et al., 2009; Woelz et al., 2009; Fediuk et al., 2019) and geoarchaeological indications of harbor environments (Seeliger et al., 2014; Wunderlich et al., 2018), as well as archaeological objects submerged due to sea-level variations or river relocations (Simyrdanis et al., 2015). A

major construction material used in the past was wood, which was used for building ships, buildings, jetties, etc. Using locally available wood species, wooden buildings in Central Europe were often made of oak. Conifers were used in Scandinavia. The properties of individual wood species were used for specific components, e.g., of ships. Thus, ship wrecks often consist of a variety of hard and soft woods (McGrail, 2014; Diener, 2012; Crumlin-Pedersen, 2004). In onshore archaeological prospection, five geophysical methods are well established: magnetics, seismics, electromagnetic induction (EMI), geoelectrics (mostly electric resistivity tomography (ERT)), and ground penetrating radar (GPR). In offshore environments, mostly hydro-acoustic/seismic methods are used (Wilken et al., 2019). Here, the contrasts of woods have been intensively studied. In Arnott et al. (2005), the seismic reflection coefficients of wood in different weathering grades were calculated. They show large differences in the reflection coefficients, caused by the weathering degree and the subsoil. Therefore, with seismic methods, wooden archaeological remains can sometimes be detected excellently, sometimes not. As an example, it is hard to prospect moderately degraded oak in clay. However, seismic methods can be complemented or replaced by ERT and GPR measurements. We recognized the potential of lacustrine GPR to image small-scale wooden structures from a sample profile showing multiple reflections that come from trunks and branches in the water column. Similar experiences were noted in Jol and Albrecht (2004) while searching for submerged lumber with GPR. They recognized diffraction hyperbolas caused by lumber both above and below the lake bottom within organic sediment. ERT and GPR become especially attractive in cases of extremely shallow water and gassy environments. For addressing the material or the degree of preservation of objects, the methods can be used as they are sensitive to lateral and vertical changes in the subsurface electric resistivity and dielectric permittivity. However, the high conductivity of the water column results in a limited depth penetration. In Simyrdanis et al. (2015) and Kritikakis et al. (2015), ERT studies are presented, and in Arcone et al. (2010) and Ruffell (2006), GPR studies are presented investigating submerged nonwooden objects. Their results show that both marine ERT and GPR are suitable methods to resolve objects within the meter scale, e.g., wall fundamentals and bombs. In Lin et al. (2010), the authors offer an approach to determine subsurface material contrasts based on the GPR signal strengths from sediments and a reference aluminum plate. However, there is no study investigating wooden material contrasts for marine and lacustrine ERT and GPR measurements.

Several studies, summarized in Niemz and Sonderegger (2017), Kollmann (1968) and Skaar (2012), investigated the electric resistivity and dielectric permittivity of wood with increasing wood moisture content. In Stamm (1927); Lin et al. (1965) among others, it is observed that there is a decrease in the electric resistivity with increasing wood moisture. In Kuroda and Tsutsumi (1982), the effects of fiber orientation are considered. However, most studies focus on wood moisture contents of 0–30 %, which do not represent the higher moisture content expected in archaeological wood (Peyskens et al., 1984). An increase in permittivity is noted, for example, in Trapp and Pungs (1956). They investigated spruce wood for different measurement frequencies (in both the MHz and GHz range) and wood-moisture contents. In James (1975), they carried

out similar investigations for Douglas fir. In Kröner and Pungs (1952), they considered the influence of fiber direction on the dielectric permittivity of dry wood. However, especially for fully water-saturated wood, which is comparable to archaeological wood, the studies do not cover all aspects regarding the influence of structural orientation and the distinction between oak as a hardwood and spruce as a softwood. In addition, the electrical resistivity of wood is usually determined using a resistance meter with two electrodes (Skaar, 2012). The dielectric permittivity is determined using plate capacitors (Niemz and Sonderegger, 2017). Thus far, none of the studies have used small-scale geophysical methods such as geoelectric four electrode arrays and GPR antennas for that purpose. Therefore, in this study, we bridge this gap and investigate to what extent ERT and GPR are suitable to prospect the remains of submerged or wooden constructions in the water column with respect to physical material parameter contrast. We follow the approach asking whether wood can be detected based on the assumption that modern water-saturated wood is comparable to unweathered archaeological wood. Using this assumption, we can neglect the manifold properties of archaeological wood, including degradation, which are often unknown during field prospecting. For further simplification, we consider oak and spruce wood, two typical representatives of hard and soft wood, showing fundamental structural differences.

Regarding the aforementioned background, our study has three aims:

- i) Investigating electric resistivity and dielectric permittivity of modern oak and spruce wood with increasing water moisture contents considering three directions of anisotropy in a long-term experiment. For this purpose, we used small-scale geophysical equipment and compared the results to previous laboratory studies;
- ii) Calculating the physical material contrasts of wood compared to different embedding materials, such as water, clayey subsoil, and sandy subsoil, for ERT and GPR measurements and comparing them to seismic material contrasts based on the work of Arnott et al. (2005);
- iii) On the basis of the determined contrasts, we performed analytical calculations to investigate the depth penetration and applicability of the ERT and GPR methods for the prospecting of wooden objects in water.

4.2 Materials and Methods

4.2.1 Preliminary Considerations to Determine Wooden Material Properties

For the determination of material contrasts of wood in different subsurfaces in the field, certain preliminary considerations are required regarding the variations of water-saturated wood. Therefore, we consider the parameters that influence the electric resistivity and dielectric permittivity which can be observed in the experiment. Wood

is an inhomogeneous, anisotropic, and capillary porous composite material of macro-, micro-, and submicron structure (Niemz and Sonderegger, 2017; Kollmann, 1968; Skaar, 2012). Inhomogeneities result from differences in the raw density, irregular water absorption of wood during the experiment, and anisotropic axes because of different structural orientations, among other things. Differences in the raw density are due to various wood species and due to irregular early and late growth rates in the microstructure. The average kiln-dry density for spruce wood is $0.43 \frac{\text{g}}{\text{cm}^3}$, whereas for oak wood an average value of $0.63 \frac{\text{g}}{\text{cm}^3}$ is defined in Niemz and Sonderegger (2017). Three anisotropy axes define the macrostructure: (1) in fiber direction; (2) radial; and (3) tangential to the annual rings across the fiber direction (Figure 4.1). Anisotropy affects both the water absorption process and the investigated physical parameters. Therefore, in the context of the study, integral values of electric resistivity and dielectric permittivity were determined along each of the three main structural directions and for both hard and softwood. Thus, different types of cutting and orientations of objects in the subsurface are taken into account. The wood moisture absorption can be divided into three different states (Niemz and Sonderegger, 2017; Kollmann, 1968). The kiln-dry state of wood has a 0% wood moisture content. In the fiber saturation state, the microstructure and submicron structure are fully saturated with bound water, showing a wood moisture content between 22% and 35%. We focus on the third state, in which the macrostructure becomes water saturated with free water. The expected maximum wood moisture content of 200% for spruce and of 111% for oak depends on the kiln-dry density and the maximum weight of the fiber-saturated state (Niemz and Sonderegger, 2017). The wood moisture content u is the relation of the mass from wet wood m_u to the mass from kiln-dry wood m_d :

$$u = \frac{m_u - m_d}{m_d} \cdot 100\% \quad (4.56)$$

Furthermore, we have to expect a faster moisturization of spruce wood than oak wood during the watering process and an irregular expansion of the wooden cell walls until maximum fiber saturation is reached. In the fiber direction, the swelling rate is $<0.5\%$ and in the direction across the fiber, the swelling rate is $>5\%$ for both wood species (Niemz and Sonderegger, 2017).

4.2.2 Experimental Setup

In the first step, the physical parameters electric resistivity ρ_s and dielectric permittivity ϵ_r were determined as a function of the wood moisture content u in a nine-month watering experiment. We applied the geophysical methods geoelectrics, using Wenner α resistivity measurements (WA), and GPR, using a 2 GHz antenna in a suitable small-scale setup. The measurements were performed on two $10 \text{ cm} \times 10 \text{ cm} \times 10 \text{ cm}$ cubes of oak and spruce wood. The measurements were performed on three side surfaces of the cubes corresponding to the main directions of anisotropy along the fiber as well as radially and tangentially to the annual rings across the fiber direction (see Figure 4.2). The size of the cubes was chosen to fit the geometric demands of the 2 GHz

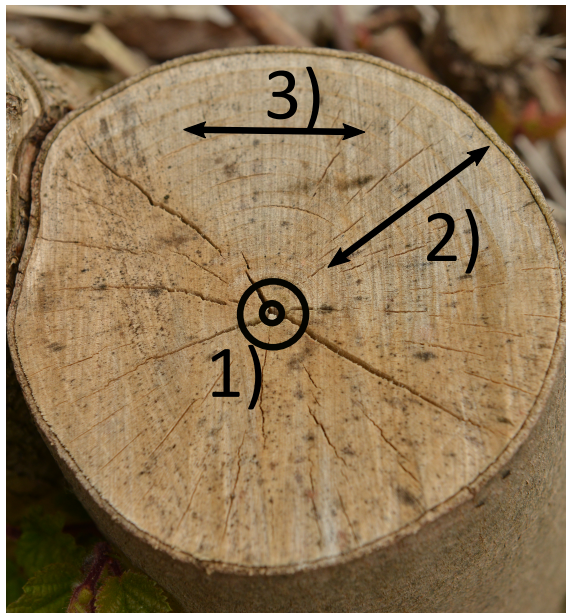


Figure 4.1: Anisotropy axes of wood: (1) in the fiber direction; (2) in the direction across the fiber, radial to the annual rings; (3) in the direction across the fiber, tangential to the annual rings

GPR antenna ($9.2\text{ cm} \times 9.2\text{ cm}$), whereas larger cubes would not be suitable because of the longer moisture saturation time. At the beginning of the experiment, the kilning method described in Niemz and Sonderegger (2017) was used to dry the wood to mass constancy at $103 \pm 2^\circ\text{C}$. The wood cubes were then placed into a tank of fresh water with an average electric resistivity of $19 \pm 0.4\ \Omega\text{m}$ and a temperature of $17 \pm 0.7^\circ\text{C}$ so that thermal conductivity effects could be ignored. At regular intervals, the wooden cubes were weighed and the wood moisture content was determined using the reference mass. This was done first daily, and then weekly, after the gradient of each curve significantly decreased. Additionally, the wooden cubes were measured with a caliper to document the swelling α , which is the expansion of each side of the moisturized cube in relation to those in the kiln-dry state. The cube expansion is required to calculate the dielectric permittivity from GPR measurements. Each measurement was repeated ten times and the Gaussian law of error propagation (Bartsch, 1982) was used to calculate the statistical error of the wood moisture content u for the first measurement of our experiment in a dry state, for the fiber-saturated state and for the maximum saturated state. In the dry state, the measurement error of the mass from wood results from inaccuracies in the electronic scale of $\Delta m_d = 0.5\text{ g}$. For the fiber-saturated as well as for the maximum saturated state, measurement errors result from the drying process of the wood during the one hour (approximately) measuring procedure. The arithmetical average weight difference between the beginning and ending of the measurement was $\Delta m_u = 3\text{ g}$ in fiber-saturated state and $\Delta m_u = 9\text{ g}$ in the saturated state. The time series of the wood moisture content u , the swelling α , the density d , as well as the electric resistivity and permittivity were fitted with mathe-

mathematical functions and compared to previous laboratory studies (Niemz and Sonderegger, 2017; Kollmann, 1968; Skaar, 2012). Obvious options were low-order polynomial functions and (limited) exponential growth, respectively, decay functions, and the sum of an exponential and a polynomial function. After some trials, the increasing wood moisture content u with time t was fitted by the sum of a limited exponential growth and a polynomial function of first order $a + b \cdot t - c \cdot e^{-\frac{t}{d}}$. The swelling α depending on the wood moisture content u was fitted by a limited growth curve of type $a - b \cdot e^{-\frac{u}{c}}$. The correlation coefficients of the fits are of the order of 0.98 in all cases. From the mass of the moisturized wood and the wood cube volumes, the density d was determined and fitted by a linear curve $a \cdot x + b$. Then, the electric resistivity and dielectric permittivity of the woods were examined. As a result of the internal wood structure of the spruce cube, the radial and tangential components in the direction across the fiber could not be clearly distinguished, which is why we expect to obtain average values of anisotropy for the two orthogonal sounding directions for this wood type.

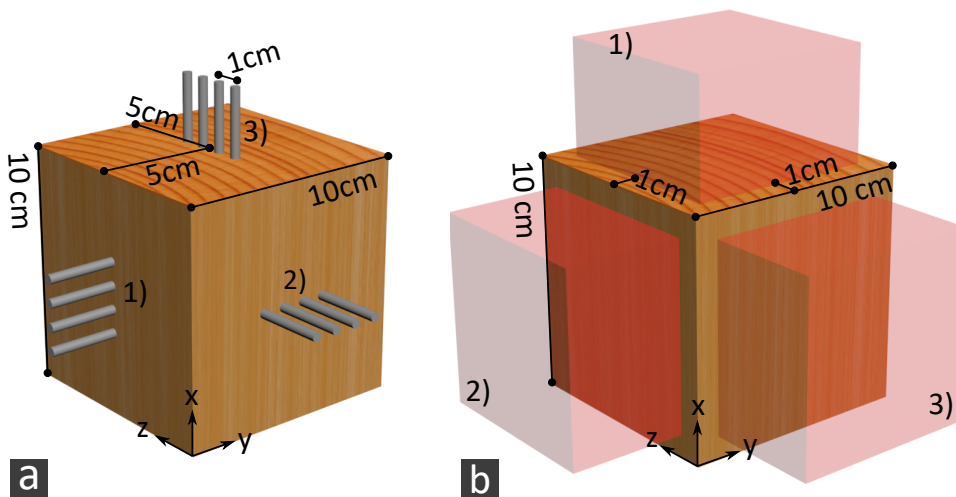


Figure 4.2: Schematic drawing of: (a) the setup for electric resistivity measurements of wood using a Wenner α configuration; (b) 2 GHz Palm antenna used for dielectric permittivity measurements of wood. Anisotropy axes of wood are highlighted: (1) in the fiber direction; (2) in the direction across the fiber, radial to annual rings, (3) in the direction across the fiber, tangential to annual rings.

4.2.3 Determination of the Electric Resistivity

For investigating the electric resistivity of the wood cubes, a four-electrode array made from screws (diameter 1 mm) with a Wenner α configuration of 1 cm electrode distance was centered on three sides of the cube corresponding to the main directions of anisotropy (Figure 4.2a). The current I and the voltage U were measured with a C.A. 6470 unit (manufactured by Chauvin Arnoux), arithmetically averaging ten repetition measurements. Assuming a homogeneous electric resistivity distribution

throughout the block (in the current anisotropy direction), the specific electric resistivity was then defined by Ohm's law (Telford et al., 1990). To estimate statistical errors in the dry state, fiber-saturated state, and maximally saturated state (exemplarily for spruce wood in the fiber direction), the Gaussian error law was again applied. Therefore, errors of the geometry factor $k = 2\pi a = 0.0628$ with an electrode spacing a of 1 cm can be estimated by electrode spacing inaccuracies of 0.1 mm, resulting in an error of $\Delta k = 6.3 \cdot 10^{-4}$. Measurement errors for the current I [A] and the voltage U [V] were defined as standard deviations from the ten measurement repetitions, and were caused by the resolution accuracy of the registration unit and by errors of the electrode coupling. The measurements could be fitted by a limited exponential decay curve of type $a + b \cdot e^{-\frac{u}{c}}$. To ensure that the measurements were not affected by the boundary surfaces of the 10 cm \times 10 cm \times 10 cm wood cubes, we used the program pyGIMLi (Rücker et al., 2016) to calculate the geometry factor of the Wenner α array for the special situation of a cube, considering the six free surfaces of the probe. This was compared with the geometry factor calculated for the common half-space. To quantify the anisotropy effects in and across the fiber direction, we calculated the relative standard deviations of the arithmetic average of all the measurement directions for each wood moisture content.

4.2.4 Determination of the Dielectric Permittivity

The relative dielectric permittivity ϵ_r was determined using a 2 GHz Palm GPR antenna (GSSI) connected to the registration unit SIR 30 (GSSI). The device setup uses two antennas in one housing which cannot be used for transmission but for reflection measurements. The relative dielectric permittivity ϵ_r is defined by the ratio of the permittivity of a material ϵ to the permittivity in free space ϵ_0 . It is inversely proportional to the square of the GPR velocity v (Butler, 2005). We determined ϵ_r via the radar wave velocity $v = \frac{2s}{t}$, where s is the side length of the cube and t is the two-way travel time of the radar wave reflected from the cube surface opposed to the side of the antenna (Figure 4.2 b); t corresponds to the travel time difference between the signal amplitudes of the direct and reflected waves. To enhance the reflection amplitude, we mounted a metal sheet at the bottom of the wooden cube. The metal sheet has a reflection coefficient of -1, which is much stronger than the reflection coefficients of possible internal wood interfaces. Figure 4.3a shows that for moisture contents $<20\%$ the travel times of the direct wave and the reflection from the base of the cube are so small that the signals interfere. Consequently, the standard use of first breaks to pick the direct wave (i.e., interference of air and ground wave) and the reflection of the metal sheet is not possible, wherefore we chose to pick the maximum signal amplitude. To estimate the measurement accuracy in this low moisture range, the experiment was also conducted with a 50 cm long spruce piece of the same log as the 10 cm long piece (Figure 4.3b). Additionally, this longer piece was used to estimate the inaccuracy that results from picking the first maxima of the wavelets (Figure 4.3b, option 1, green line) instead of the first breaks (Figure 4.3b, option 2, yellow line). The measurement uncertainties of the GPR measurements were again estimated via the Gaussian error propagation

law, considering deviations of the travel time and of the dimensions of the wood. The travel time error $\Delta t = 0.01$ ns is defined as the standard deviation of the picked time difference between the signal amplitudes from ten repetition measurements. Errors of the dimensions of the wood cubes $\Delta s = 0.05$ cm are caused by inaccuracies using the caliper and an irregular expansion of the wood during the watering process. The calculated dielectric permittivity values could be fitted by an exponential curve of type $a + b \cdot e^{\frac{t}{c}}$. Anisotropy effects were also considered, using the same approach as for the electric resistivity.

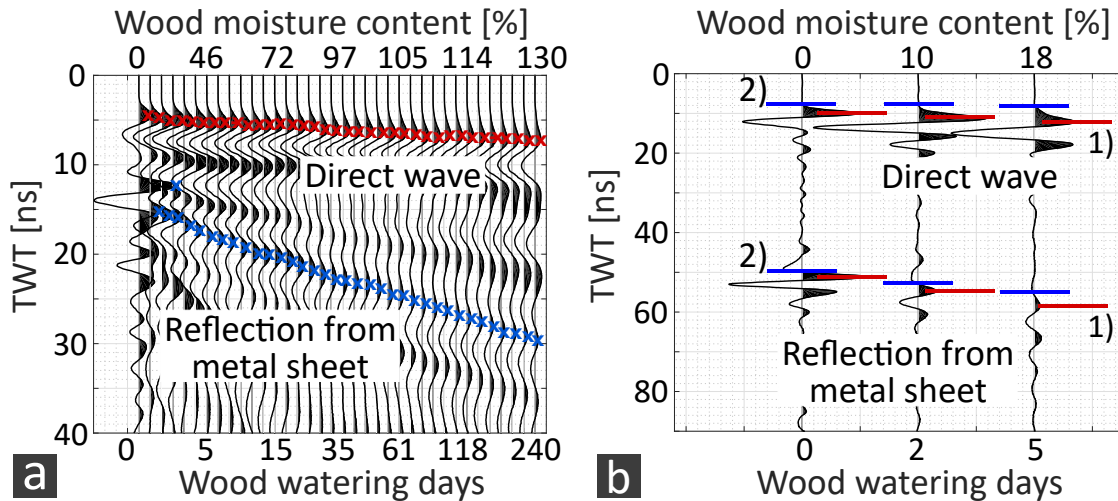


Figure 4.3: Wiggle plot of spreading corrected radar signals that change with increasing wood moisture content for: (a) spruce wood cube of size 10 cm \times 10 cm \times 10 cm in the fiber direction (red and blue marks highlight the picked amplitudes); and (b) spruce wood cube of size 10 cm \times 10 cm \times 50 cm in the fiber direction. Here, two possible definitions of the travel time through the wood cubes for kiln-dry and moisturized wood are compared: (1) the maximum signal amplitude from the direct wave respectively wood–metal interface (green); and (2) the zero position before the respective signal amplitude (yellow).

4.2.5 Determination of Relative Material Parameter Contrasts

In the next step, relative contrasts of the electric resistivity and dielectric permittivity from the submerged wood in three different subsurface materials were determined. Following Arnott et al. (2005), we selected fresh water, sandy subsoil, and clayey subsoil as the hypothetical embedding materials for the wooden objects. The parameters for water-saturated oak and spruce wood for three anisotropy directions were taken from the experiment. However, the maximum wood moisture content was not reached by the end of the experiment. Therefore, the values of the electric resistivity and the dielectric permittivity were extrapolated to the expected maximum wood moisture content using the fitted curves. The parameters of the embedding material were taken

Embedding Material	Electric Resistivity	Dielectric Permittivity
Freshwater	21 Ωm (Schön, 1983)	81 (Schön, 1983)
Saturated sand	75 Ωm (Schön, 1983; Archie et al., 1942)	20 (Annan, 2003)
Saturated clay	40 Ωm (Knödel et al., 2013)	40 (Annan, 2003)

Table 4.1: Reference values of the electric resistivity and dielectric permittivity for the embedding materials freshwater, saturated sand, and saturated clay.

from literature and are summarized in 4.1. Especially, saturated sands and clays show a large possible value range, so that exemplary values were chosen for our investigations. In order to determine the specific resistivity of a sandy subsoil, Archie's law (Archie et al., 1942) was used assuming a water resistivity of 21 Ωm . The relative material contrast for the geoelectric measurements depends on the specific electric resistivity of the wood ρ_{sw} and of the subsurface ρ_{ss} (Telford et al., 1990).

$$r_{\rho_s} = \frac{\rho_{ss} - \rho_{sw}}{\rho_{ss} + \rho_{sw}} \quad (4.57)$$

Neglecting the influence of the magnetic permeability and the electric resistivity on GPR reflectivity, the effective GPR material contrasts correspond to the reflection coefficients depending on the relative dielectric permittivity of the wood ϵ_{rw} and of the subsurface ϵ_{rs} (Butler, 2005).

$$r_{\epsilon_r} = \frac{\sqrt{\epsilon_{rs}} - \sqrt{\epsilon_{rw}}}{\sqrt{\epsilon_{rs}} + \sqrt{\epsilon_{rw}}} \quad (4.58)$$

The relative seismic material contrasts are also equal to the seismic reflection coefficient, depending on the seismic velocity (v_w) and density of the water layer (d_w) and of the subsurface layer (v_s and d_s) (Telford et al., 1990).

$$r_s = \frac{d_s \cdot v_s - d_w \cdot v_w}{d_s \cdot v_s + d_w \cdot v_w} \quad (4.59)$$

4.2.6 Geophysical Detection Swell of Wooden Targets in Lacustrine Environment

On the basis of the parameter contrasts of wood embedded in soils and freshwater, we finally discuss the implications of the depth range, in which wooden objects can be detected through geoelectric and GPR measurements. This depth detection swell does not only depend on the parameter contrasts but also on the instrumental sensitivity, the ambient noise level, the shape of the objects, and in case of GPR, the attenuation of the up- and downward travelling waves. For this estimate, we assume: (1) that

the shape of the wooden objects can be approximated by spheres or long horizontal cylinders oriented orthogonally to the sounding profile; and (2) that the wooden objects are embedded in a homogeneous half space. In these cases, the geoelectrical and GPR ground responses can be estimated analytically. The formulae given below can be derived by simple algebra for GPR from equations provided in Davis and ANNAN (1989) and Hilterman (1975) and the geoelectric sounding in Schlumberger configuration were provided in Töpfer (1969). Ideal measuring conditions are assumed. For the geoelectrical detection swell of spheres and horizontal cylinders, we obtained

$$r_{electric_sphere} = \left(M \cdot \frac{\rho_0 + 2\rho_1}{\rho_0 - \rho_1} \right)^{\frac{1}{3}} \cdot h_0 \quad (4.60)$$

and

$$r_{electric_cylinder} = \left(M \cdot \frac{\rho_0 + \rho_1}{\rho_0 - \rho_1} \right)^{\frac{1}{3}} \cdot h_0 \quad (4.61)$$

where $r_{electric_sphere}$ is the radius of the sphere, $r_{electric_cylinder}$ is the radius of the cylinder, ρ_0 is the specific resistivity of the half-space, and ρ_1 is the specific resistivity of the sphere/cylinder. h_0 is the midpoint depth of the sphere/cylinder and $z_{TOP} = h_0 - r_{electric_sphere/cylinder}$ is the depth to the top of the object. $M = \frac{2(\Delta\rho_a)}{\rho_0}$ is the measurement accuracy within 95% bounds, $\frac{\Delta\rho_a}{\rho_0}$ is the relative standard deviation of the measurements, and ρ_a is the apparent resistivity. The GPR detection swell of spheres and horizontal cylinders is

$$r_{GPR_sphere} = \left(P e^{-2\alpha z_{top}} \frac{R}{2z_{top}} - 1 \right)^{-1} z_{top} \quad (4.62)$$

and

$$r_{GPR_cylinder} = \left(P e^{-2\alpha z_{top}} \frac{R^2}{4z_{top}^2} - 1 \right)^{-1} z_{top} \quad (4.63)$$

where r_{GPR_sphere} is the radius of the sphere, $r_{GPR_cylinder}$ is the radius of the cylinder, z_{TOP} is the depth to the top of the object, P is the GPR system performance, R is the reflection coefficient, and a is the absorption coefficient. We estimated the GPR detection swell for a 400 MHz antenna, which can be used to prospect targets a few meters below the subsurface and is regularly used in the geophysical prospection of archaeological objects. In contrast, the 2 GHz antenna used in the experiment has a depth penetration within the decimeter range and is usually not used during field measurements. However, the experiment could only be carried out using a 2 GHz antenna due to the

Geoelectric	Freshwater	Saturated sand	Saturated clay
ρ_s of half space	21 Ωm	40 Ωm	75 Ωm
ρ_s of wood		250 Ωm	
GPR	Freshwater	Saturated sand	Saturated clay
GPR velocity of half space	3.3 $\frac{\text{cm}}{\text{ns}}$	7 $\frac{\text{cm}}{\text{ns}}$	5 $\frac{\text{cm}}{\text{ns}}$
Attenuation of half space	0.1 $\frac{\text{dB}}{\text{m}}$	0.17 $\frac{\text{dB}}{\text{m}}$	10 $\frac{\text{dB}}{\text{m}}$
Reflection coefficient wood/embedding material	-0.34	-0.06	-0.17

Table 4.2: Summary of the material parameters assumed for the wood and the embedding material, freshwater, saturated clay, and sand to discuss the implications for the depth range.

antenna and wood dimensions. As discussed in section 4.4.3, dielectric permittivity values increase with lower measurement frequencies. Comparing the frequencies of 400 MHz and 2 GHz, this effect does not significantly change the detection swell. Therefore, we used the measured dielectric permittivity values of the experiment. The material parameters assumed for the wood and the embedding material, i.e., freshwater, saturated clay, and sand, are listed in 4.2. The technical resolution limits of the field units (electronic noise) and the ambient noise level are critical. For these, we assumed that the geoelectric response of the embedded objects is detectable if it exceeds the background by 2%. For the GPR, we assumed a practical system performance of 96dB.

4.3 Results

4.3.1 Water Absorption, Swelling, and Density Increase of Moisturized Wood during the Experiment

Figure 4.4a shows the development of the wood moisture content for oak u_o (blue) and spruce wood u_s (red) depending on the watering time t of the wood cubes. During the measuring period, none of the wooden cubes reached their maximum wood moisture content. The experiment was terminated at a final wood moisture content of 100% for oak and of 130% for spruce wood. The increasing wood moisture content for oak wood u_o and spruce wood u_s with time t was approximated by the functions summarized in Table 4.3. The wood density d shows a linear increase (Figure 4.4b; for the fitting function see Table 4.3; for the mean values see Table 4.4). The swelling of oak and spruce as due to an increasing wood moisture content u is shown in Figure 4.5 across the fiber in radial (a) and tangential directions (b), and in the fiber direction (c). It can be fitted by limited growth curves (Table 4.3). Directional differences in the swelling are especially apparent in and across the fiber directions. In the fiber direction (Figure

4.5c), there are only minimal changes of less than 0.5%. In the direction across the fiber, an increase of $> 4\%$ was found for oak and spruce wood in the direction across the fiber (radial, Figure 4.5a; tangential, Figure 4.5b). The experimentally determined masses, density values, dimensions, and volumes of the wood cubes in kiln-dry and in their maximally saturated state are listed in Table 4.4. The measurement uncertainties of the wood moisture content u are $<1\%$ in the dry and fiber-saturated state, and $<3\%$ in the maximum saturated state.

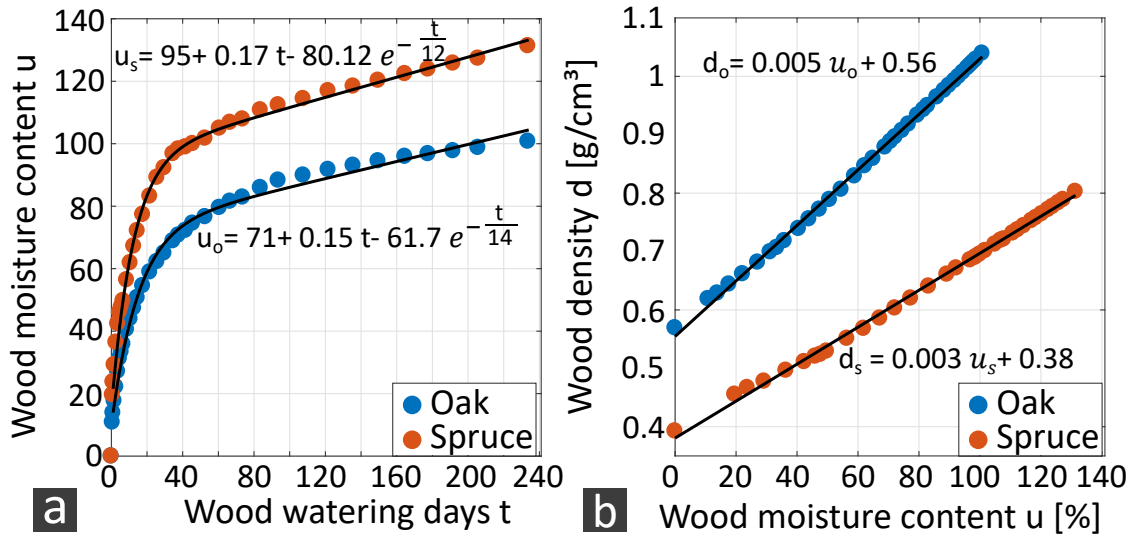


Figure 4.4: (a) Wood moisture content of oak (blue) and spruce wood (red) plotted against the wood watering time in days. (b) Development of wood density depending on the wood moisture content for oak (blue) and spruce (red).

4.3.2 Electric Resistivity

The results of the measurements of electric resistivity for oak and spruce wood with increasing wood moisture content are presented in Figure 4.6 and in Table 4.5. There is a limited exponential decay of the specific resistivity with increasing wood moisture content, for which the fitting functions are given in Table 4.6. The two wood types and the three main anisotropy directions show distinctly different values. The specific resistivity of oak wood converges to a minimum value of about $250 \Omega\text{m}$, which is also approximated by the asymptotes of the fitted curves. The spruce wood also converges to a minimum resistivity value of about $1 \Omega\text{m}$. For the uncertainties of the derived electric resistivity values, we obtained an almost constant value of $<3.5\%$ for all investigated states. The possible effects of the cube surface boundaries on the geometry factor and thus on the measurements are within the range of the measurement errors and can be neglected. The anisotropy of electric resistivity is largest in the dry state. Measurements in the fiber direction are slightly less resistant compared to the measurements from the direction across the fiber. At higher wood moisture content, the

	Fitted u Curve	Corr. Coeff.	Fitted α Curve	Corr. Coeff.	Fitted d Curve	Corr. Coeff.
Oak, Fiber			$10 - 0.05 \cdot e^{\frac{-u_o}{14.5}}$	0.98		
\perp Fiber, radial to annual rings	$71.04 + 0.15 \cdot t - 61.68 \cdot e^{\frac{-t}{14.12}}$	1	$10.05 - 0.47 \cdot e^{\frac{-u_o}{30.4}}$	0.98	$0.0047u_o + 0.56$	1
\perp Fiber, tangential to annual rings			$10.14 - 0.52 \cdot e^{\frac{-u_o}{26.4}}$	0.99		
Spruce, Fiber			$10.07 - 0.03 \cdot e^{\frac{-u_s}{42.9}}$	0.96		
\perp Fiber, radial to annual rings	$94.99 + 0.17 \cdot t - 80.12 \cdot e^{\frac{-t}{11.91}}$	1	$10.36 - 0.71 \cdot e^{\frac{-u_s}{35.5}}$	0.98	$0.0031u_s + 0.38$	1
\perp Fiber, tangential to annual rings			$10.45 - 0.7 \cdot e^{\frac{-u_s}{40.6}}$	0.97		

Table 4.3: Summary of curve parameters fitting the wood moisture content u , swelling α , and density d for oak and spruce wood in three measurement directions.

	Spruce Kiln-Dry ($u = 0\%$)	Spruce Moisturized ($u = 200\%$)	Oak Kiln-Dry ($u = 0\%$)	Oak Moisturized ($u = 111\%$)
Mass [g]	375.0	867.5	525.5	1055
Density [$\frac{\text{g}}{\text{cm}^3}$]	0.39	0.80	0.57	1.04
Volume [cm^3]	955.38	1080.79	923.21	1014.02
Length fiber [cm]	10.04	10.07	9.95	10.00
Length \perp fiber, radial [cm]	9.70	10.32	9.63	10.02
Length \perp fiber, tangential [cm]	9.81	10.40	9.63	10.12

Table 4.4: Summary of physical wood properties for oak and spruce wood in the kiln-dry and in the saturated state.

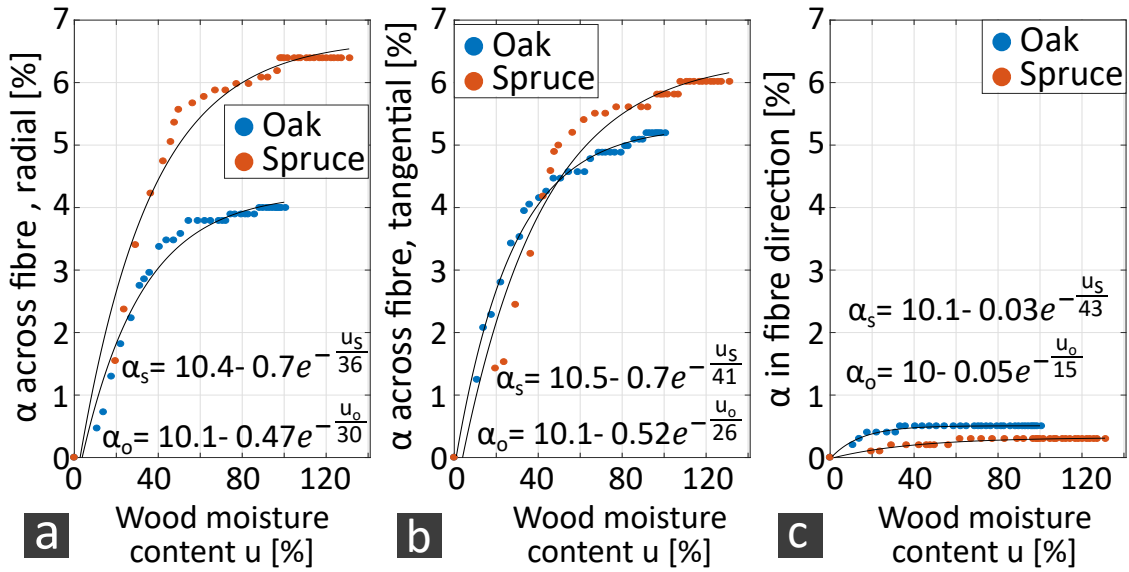


Figure 4.5: Swelling α of oak (blue) and spruce wood (red) depending on the wood moisture content (a) in the direction across the fiber, radial to annual rings, (b) in the direction across the fiber, tangential to annual rings, and (c) in the fiber direction.

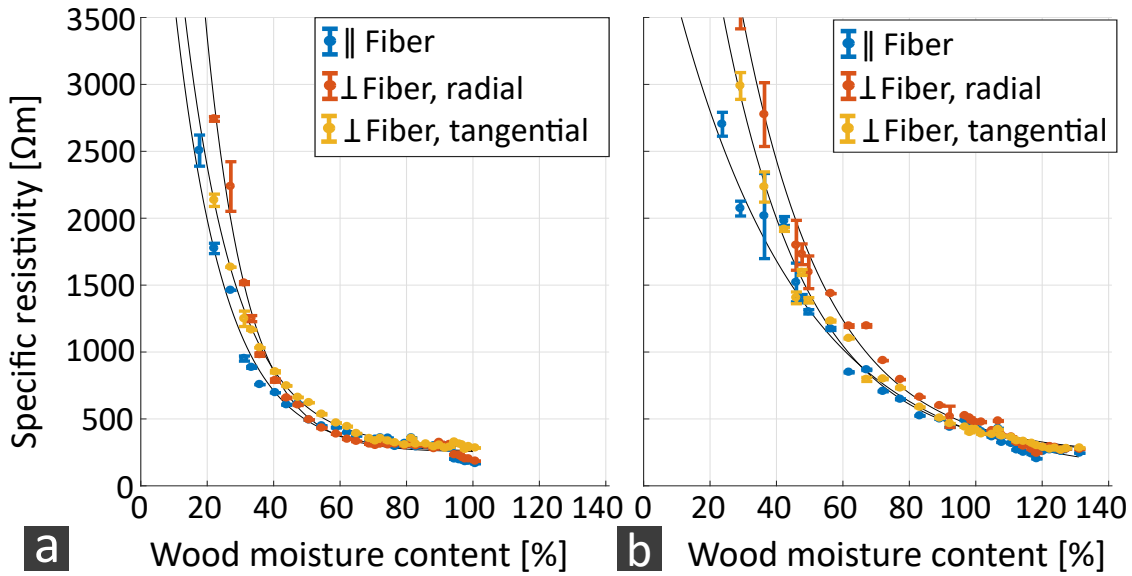


Figure 4.6: Electric resistivity of (a) oak and (b) spruce depending on the wood moisture content in the fiber direction (blue error bar), in the direction across the fiber, radial to annual rings (red error bar), and in the direction across the fiber, tangential to annual rings (yellow error bar). The equations of the fitted curves can be found in Table 4.6.

anisotropy effects become smaller. The anisotropy effects of the wood have a maximum of 15%.

	Spruce Kiln-Dry ($u = 0\%$)	Spruce Moisturized ($u = 200\%$)	Oak Kiln-Dry ($u = 0\%$)	Oak Moisturized ($u=111\%$)
Fiber	>2500 Ωm	79 Ωm	>3500 Ωm	312 Ωm
\perp Fiber, radial to annual rings	>2500 Ωm	297 Ωm	>3500 Ωm	272 Ωm
\perp Fiber, tang. to annual rings	>2500 Ωm	270 Ωm	>3500 Ωm	286 Ωm

Table 4.5: Summary of electric resistivity values for oak and spruce wood in the kiln-dry and in the fully saturated state (extrapolated).

4.3.3 Dielectric Permittivity

Figure 4.7 presents the results of the dielectric permittivity with increasing wood moisture content. Again the wood types oak (Figure 4.7a) and spruce (Figure 4.7b) as well as the three anisotropy measurement directions are distinguished. The measurement uncertainties are 5%, 4%, and 2% for the kiln-dry, fiber-saturated, and maximally saturated states, respectively. The offset that results from picking the first maxima of the wavelets (Figure 4.3b, option 1) instead of the first breaks (Figure 4.3b, option 2) is about 5% in the dry state and about 20% in maximum saturated state. For oak wood, we found an exponential increase in the relative dielectric permittivity with moisture content (Figure 4.7 and Table 4.6). The three measurement directions show a relative dielectric permittivity of 2 in the kiln-dry state. For the maximally reached wood moisture content in the experiment, the relative dielectric permittivity increases to 12–22 according to fiber direction. The dielectric permittivity values extrapolated to full water saturation are summarized in Table 4.7. As a result of the unsteady measurement curve for the tangential direction across the fiber of the spruce wood, we used an estimate instead of the extrapolation. The ratio of the three measuring directions at the last measured value was maintained. This suggests that anisotropy effects become larger with increasing wood moisture content. The minimum and maximum permittivity values for all measurement directions of spruce wood are slightly lower than those of the oak. The anisotropy effects of the GPR measurements have a maximum of 30%.

4.3.4 Relative Material Parameter Contrasts

From the investigations of the electric resistivity and the dielectric permittivity of moisturized wood extrapolated from the experiment, the relative material contrasts of wood in different subsoils could be calculated using additional literature values. Figure 4.8 and Table 4.8 summarizes the results, which distinguish between geoelectrical (Wenner α) and GPR material contrasts of wood in fresh water, a clayey subsoil, and a sandy subsoil. Figure 4.8 is based on the tangential direction across the fiber. Table 4.8 provides the variation of contrasts when additionally considering the fiber direction

	ρ_s : Fitted Curve	Corr. Coeff.	ϵ_r : Fitted Curve	Corr. Coeff.
Oak, Fiber	$310.0 + 8068 \cdot e^{-\frac{u}{13}}$	0.99	$-9.5 + 9.9 \cdot e^{\frac{u}{85.5}}$	1
⊥ Fiber, radial to annual rings	$270.8 + 16520 \cdot e^{-\frac{u}{12}}$	0.99	$1 + 1.6 \cdot e^{\frac{u}{51.8}}$	1
⊥ Fiber, tangential to annual rings	$278.5 + 7549 \cdot e^{-\frac{u}{16}}$	1	$-7.6 + 9.2 \cdot e^{\frac{u}{100.9}}$	0.99
Spruce, Fiber	$52 + 4578 \cdot e^{-\frac{u}{39}}$	0.95	$-4.6 + 6 \cdot e^{\frac{u}{92.9}}$	0.99
⊥ Fiber, radial to annual rings	$294 + 11120 \cdot e^{-\frac{u}{24}}$	0.87	$1.2 + 1.3 \cdot e^{\frac{u}{60.5}}$	1
⊥ Fiber, tangential to annual rings	$266.9 + 8592 \cdot e^{-\frac{u}{25}}$	0.94	$-0.1 + 1.5 \cdot e^{\frac{u}{55.2}}$	0.98

Table 4.6: Summary of curve parameters fitting the electric resistivity and dielectric permittivity measurements for oak and spruce wood in three measurement directions.

	Spruce Kiln-Dry ($u = 0\%$)	Spruce Moisturized ($u = 200\%$)	Oak Kiln-Dry ($u = 0\%$)	Oak Moisturized ($u = 111\%$)
Fiber	1.8	47	2	27
⊥ Fiber, radial to annual rings	1.8	37	2	15
⊥ Fiber, tangential to annual rings	1.8	41	2.1	20

Table 4.7: Summary of dielectric permittivity values for oak and spruce wood in the kiln-dry and in the fully saturated state (extrapolated).

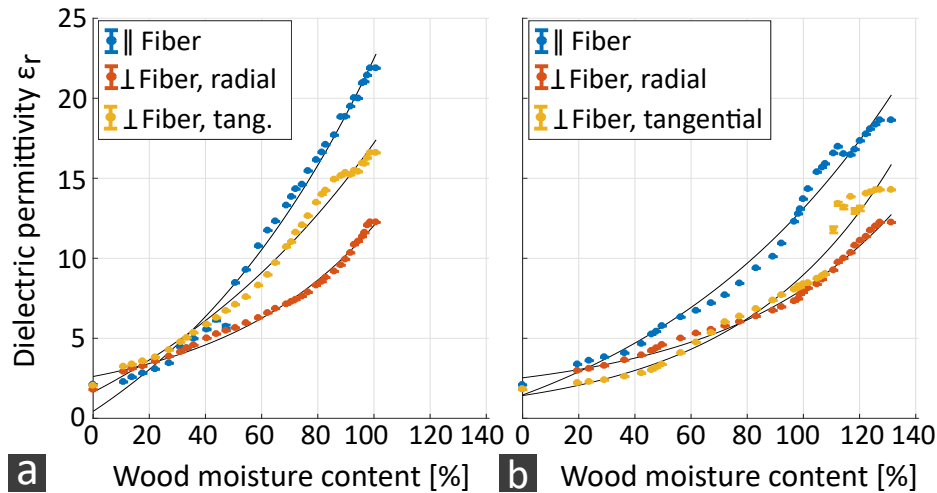


Figure 4.7: Dielectric permittivity of (a) oak and (b) spruce depending on the wood moisture content in the fiber direction (blue error bar), in the direction across the fiber, radial to annual rings (red error bar), and in the direction across the fiber, tangential to annual rings (yellow error bar).

and the radial direction across the fiber. In addition, relative seismic material contrasts whose physical parameters were taken from Arnott et al. (2005) are listed. The pine wood used in the study of Arnott et al. (2005) is listed as spruce wood for reasons of comparability of soft and hard woods. Comparing the three methods, the largest parameter contrasts can be expected for the geoelectric measurements, followed by GPR, and seismic measurements. For all methods, the highest material contrasts for nonweathered wood can be found in water, followed by a clayey, and sandy subsoil. For both GPR and seismic measurements, there are exceptions where the surrounding materials cause very low contrasts. This applies in particular to the contrast of oak wood compared to a sandy subsoil and of pine wood compared to a clayey subsoil.

4.3.5 Geophysical Detection Swell of Wooden Targets in Lacustrine Environment

Figure 4.9 a shows the linear relationship between the body diameter and its maximum detection depth for geoelectric measurements. A wooden body of the diameter 0.5 m can be detected at a depth of 0.5 m–1.5 m. The shape of the body is more important than the surrounding material. The deepest objects can be detected in fresh water, followed by saturated clay and saturated sand. For GPR measurements, an object with a diameter of 0.5 m can be detected at between 0.5 m and 3 m in depth (Figure 4.9b). The surrounding materials show a stronger influence on the results, whereas the curves for cylinders and spheres are in similar value ranges. The deepest penetration is reached in freshwater, followed by saturated sand. In particular, saturated clay shows a high attenuation. There is a clear difference between the methods. In contrast to geoelectrics, GPR measurements can detect diameters of >10 cm at depths of

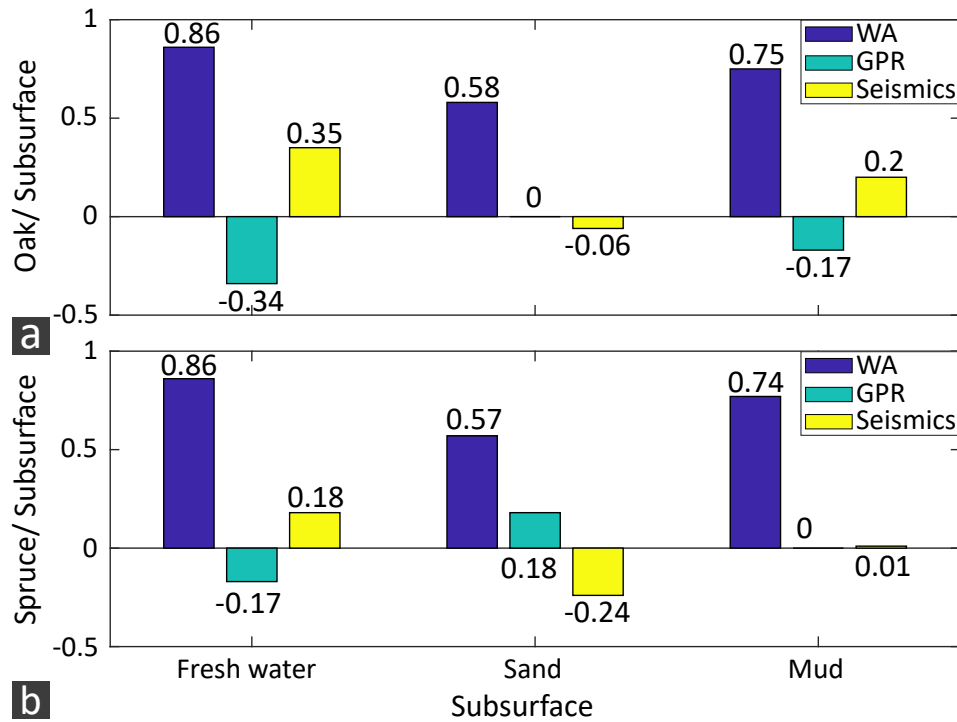


Figure 4.8: Comparison of relative material contrasts of oak wood (a) and spruce wood in tangential the direction across the fiber (b) to fresh water (left), sandy subsurface (middle), and clayey subsurface (right) for geoelectrical (Wenner α , blue), ground penetrating radar (GPR) (green), and seismic measurements (yellow).

0.5 m–2.75 m. For a 400 MHz antenna and for diameters >0.5 m, the maximum depth penetration is reached, whereas geoelectrical measurements are not limited here.

4.4 Discussion

4.4.1 Swelling and Density Increase of Moisturized Wood during the Experiment

Swelling

The percentage of wood swelling observed in our experiment coincides with studies of Niemz and Sonderegger (2017) and Skaar (2012). They found a linear swelling until the fiber-saturated state was reached (at a wood moisture content of 30% and 23% for spruce and oak wood, respectively). After that, the curve converges to a maximum limit. In our experiment, a linear increase in swelling of the same order was observed, too. The linear swelling was observed until a wood moisture content of 50% and 30% was reached for oak and spruce wood, respectively. These differences can be explained by the irregular water absorption of the wooden cube during the watering process in

	ERT	GPR	Seismics
Oak/ fresh water	0.86 to 0.87	-0.4 to -0.27	0.35
Spruce/ fresh water	0.87 to 0.58	-0.19 to -0.14	0.18
Oak/ sandy subsoil	0.56 to 0.61	-0.07 to 0.07	-0.06
Spruce/ sandy subsoil	0.6 to 0.3	0.15 to 0.21	-0.24
Oak/ clayey subsoil	0.74 to 0.77	-0.24 to -0.1	0.2
Spruce/ clayey subsoil	0.76 to 0.33	-0.01 to 0.04	0.01

Table 4.8: Comparison of the reflection coefficient of unweathered oak and spruce wood with the subsoil and the water column for the following methods: electric resistivity tomography (ERT), GPR, and seismics. For ERT and GPR, the range of material contrasts determined in the radial direction across the fiber (first value) and in the fiber direction (second value) are given. The seismic reflection coefficients were calculated for pine instead of spruce wood.

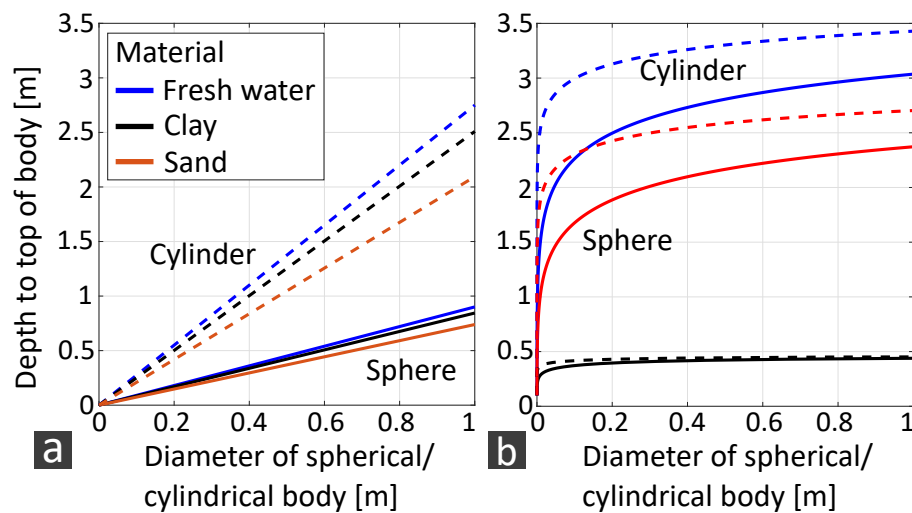


Figure 4.9: Estimation of the maximum detectable depth position of a spherical (solid line) and cylindrical (dashed line) wooden body as a function of its diameter x . (a) Geoelectrical (Schlumberger) and (b) GPR investigations (400 MHz) as well as the subsurface materials fresh water (blue line), clay (black line), and sand (red line) are distinguished.

our experiment. By the time the fiber-saturated state was reached in the wood core, the edges of the cube showed a higher wood moisture content than the maximum fiber saturation. The maximum swelling limit depends on the anisotropy direction and type of wood. Oak as the denser wood shows the greater swelling. The experimentally determined swelling in the fiber direction fits well with the values from Niemz and Sonderegger (2017) (see also Table 4.9). However, the internal wood structure of the spruce cube does not allow a clear separation of radial and tangential anisotropy axes in the direction across the fiber for the chosen measurement directions on each side of the wood cubes. Thus, the radial and tangential directions across the fiber show an

Swelling	Experiment	Literature
Spruce, Fiber	0.29%	0.2% - 0.4%
Spruce, ⊥ Fiber, radial	6.4%	3.7%
Spruce, ⊥ Fiber, tangential	6%	8.5%
Oak, Fiber	0.5%	0.3% - 0.6%
Oak, ⊥ Fiber, radial	4%	4.6%
Oak, ⊥ Fiber, tangential	5.1%	10.9%

Table 4.9: Comparison of wood swelling observed during our experiment and from the studies in Niemz and Sonderegger (2017).

State	Measurement Errors		Wood Type		Anisotropy	
	Kiln dry	Wet	Kiln dry	Wet	Kiln dry	Wet
Electric Resistivity	<3%	<2%	30%	15%	15%	5%
Dielectric permittivity	<5%	<5%	3%- 19%	3%- 19%	7%	32%

Table 4.10: Weighting of the influences of measurement errors, wood types, and anisotropy effects on the measured values of electric resistivity and dielectric permittivity.

average value of the reported values in the literature. For oak wood, the swelling in the direction across the fiber remains smaller than presented in Niemz and Sonderegger (2017). This may have been caused by incomplete wood moisture saturation.

Density

Focusing on the average raw density of the woods, Niemz and Sonderegger (2017) reports average values of $0.43 \frac{\text{g}}{\text{cm}^3}$ and $0.63 \frac{\text{g}}{\text{cm}^3}$ for spruce and oak, respectively. The wood cubes used for our laboratory experiment show values of $0.39 \frac{\text{g}}{\text{cm}^3}$ and of $0.57 \frac{\text{g}}{\text{cm}^3}$ for spruce and oak wood, respectively. Hence, they represent their respective wood types. The observed linear density increase of the wood cubes with increasing wood moisture content during the experiment corresponds to investigations presented in Kollmann (1968).

4.4.2 Electric Resistivity

Experimental Data

The decrease in the electric resistivity with moisture content in our experiment is in accordance with the studies in Kollmann (1968), Skaar (2012) and Lin et al. (1965). In Kollmann (1968), the specific resistivity is determined as a function of the moisture content for redwood. The study states that kiln-dry wood is a good isolator and that there is a linear relationship between the logarithm of the specific resistivity and the wood moisture content up to fiber saturation. At fiber saturation, the curve converges towards $80 \Omega\text{m}$. The same trend is also observed in our experiment. A constant decrease in the electric resistivity can be observed until a wood moisture content of 50% for spruce and of 33% for oak was reached. Then, the values converge towards $250 \Omega\text{m}$ for both oak and spruce, which could be fitted by exponential decay curves. Deviations of the asymptotes of the fitted curves from the average values of the measurements are within the limits of the measurement inaccuracies of 3%.

Anisotropy

We determined higher anisotropy effects of 15% for experimental measurements in the fiber-saturated state (30% wood moisture content) than at the maximum wood moisture content reached (120% wood moisture content). Here, anisotropy effects of 5% become almost negligible (see also Table 4.10). A comparable study in Niemz and Sonderegger (2017) investigated the specific electric resistivity in the directions along and across the fiber for a wood moisture content of 9% for copper beech. The significantly higher observed anisotropy effects of 110% are possibly related to the low wood moisture content of 9% used in the study.

Wood Species

We also consider the relative standard deviations of the arithmetical averaged electric resistivity from the two types of wood. In our experiment, differences between the two wood types of 30% were obtained in relatively dry condition (see Table 4.10). With a maximally reached wood moisture content of 130%, the value decreases to 15%, so that the differences between the wood types become smaller. In order to compare the results with the literature, again a study in Niemz and Sonderegger (2017) was taken into account. Here, deviations of 57% were observed for a wood moisture content of 20%, which are again significantly larger than our experimentally determined values. From this, it can be concluded that there are also large inhomogeneities within a wood species that are caused by age and density differences as well as different parts of the internal trunk structure.

Wood Moisture Content	Experiment	Literature
0%	1.8	1.7
30%	3.2	3.5
80%	6.1	7

Table 4.11: Comparison of dielectric permittivity values of spruce wood depending on the wood moisture content observed during our experiment and in Niemz and Sonderegger (2017).

4.4.3 Dielectric Permittivity

Experimental Data

In our experiment, we could see an increase in dielectric permittivity observed in Trapp and Pungs (1956) and James (1975). The dielectric permittivity as a function of the wood moisture content is discussed in detail for spruce wood (in the radial across fiber direction) in Niemz and Sonderegger (2017) and Trapp and Pungs (1956). The results of Niemz and Sonderegger (2017) are summarized in Table 4.11. The observed results of our experiment agree with those of the literature. Spruce wood showed higher permittivity values than oak wood (see Table 4.7) due to its higher reached maximum wood moisture content. In our experiment, the highest permittivity values were obtained in the fiber direction, followed by the tangential and radial direction to the annual rings in the direction across the fiber. This is comparable to the values in Peyskens et al. (1984). In Kröner and Pungs (1952), the dielectric constant in the directions with and across the fibers for kiln-dry spruce and oak wood is also investigated. A permittivity of 3.06 was obtained for spruce in the fiber direction, whereas permittivity values of 1.98 and of 1.91 were obtained for the radial and tangential directions across the fiber. Oak wood shows a dielectric permittivity of 2.86 in the fiber direction, of 2.3 in the radial direction and of 2.46 in the tangential direction across the fiber. In addition to the measurement errors of less than 5%, the deviations compared to the reference literature values are within the scope of the inaccuracy, which is caused by picking the maximum signal amplitude instead of the first break of the signal amplitude. Our results apply to the GHz range. A discussion of the change in permittivity with the measurement frequency is given in Skaar (2012) and Trapp and Pungs (1956). The dielectric permittivity of spruce wood in the radial direction at a wood moisture of 96% is about 10 for a measurement frequency of 400 MHz and about 7 for a measurement frequency of 2 GHz (Trapp and Pungs, 1956). Thus, we expect slightly higher permittivity values for lower measurement frequencies used during field prospections than in the experiment. This also affects the material contrasts. However, our results regarding the resolution of wood in various embedding materials and the influence of wood species and cutting directions on the material contrasts remain unchanged.

Anisotropy

In order to derive anisotropy coefficients of hard and soft wood from the literature, which we defined as relative standard deviations between the measured values of the three anisotropic directions, we refer to Peyskens et al. (1984) and Kröner and Pungs (1952). In Kröner and Pungs (1952), they investigated the dielectric permittivity of oak and spruce for the three anisotropy axes of kiln-dry wood. On the basis of these results, we calculated an anisotropy effect of 28% for spruce wood and of 11% for oak wood. Our experimentally measured data shows lower anisotropy effects of 8% for kiln-dry wood (see Table 4.10). To investigate the anisotropy effects for a wood moisture content of 30%, we considered the study of Peyskens et al. (1984). Here, the dielectric permittivity was investigated for the three anisotropic directions for pine wood. On the basis of these results, we calculated a relative standard deviation of 27%, which fits well to the anisotropy effects of 20% to 37% observed in our experiment.

Wood Species

To investigate the influence of different wood species on the dielectric permittivity with increasing wood moisture content in the literature, we refer to Niemz and Sonderegger (2017) and Kröner and Pungs (1952). In Kröner and Pungs (1952), they investigated the dielectric permittivity for kiln-dry oak and spruce wood in three anisotropy directions. On the basis of these results, we calculated relative standard deviations of 5% to 18% depending on the measurement axis. Furthermore, we used Niemz and Sonderegger (2017) to differentiate between deviations of wood species in moisturized state in the fiber direction. For spruce and birch wood, we calculated deviations of 11% for a wood moisture content of 30%, and deviations of 18% for a wood moisture content of 80% from the study. From the dielectric permittivity values observed in our experiment, deviations of 3% to 19% (see Table 4.10) were reached for dry and moisturized wood.

4.4.4 Relative Material Parameter Contrasts

Our investigations show that GPR and seismic measurements have an equal amount of advantages and disadvantages in the resolution of fresh water-saturated, unweathered wood in different embedding materials. In particular, material contrasts of hardwood compared to sand and softwood compared to mud clay are difficult to prospect. The wood species and the structural orientation of the wood contribute to whether a wooden object can be found. For geoelectric measurements, we cannot distinguish between the influences of the wood species and the structural orientation of wood on the material contrasts. This is different with GPR measurements. Here, the type of wood and the structural orientation show different effects on the material contrasts. Moreover, the wood species have a stronger influence on the contrasts than the structural orientation of the wood. The described differences of the measurement methods can be explained by the varying the maximum wood moisture content of the wood species. The electrical resistivity values observed during the experiment did

not change significantly for higher saturation rates. The dielectric permittivity, on the other hand, increases proportionally to the maximum wood moisture content of the respective wood species. In this study, we do not consider the effect of weathered wood on the contrasts. Compared to moisturized wood, even lower electric resistivity values and higher dielectric permittivity values are to be expected for weathered wood. Thus, we can assume that material contrasts of weathered wood compared to fresh water become smaller, whereas contrasts compared to a sandy or clayey subsoil might increase. This will also affect the depth range. Therefore, in a freshwater environment, weathered wood can be prospected at shallower depths than unweathered wood. In a clayey or sandy subsurface, this might be reversed. As a result of the increased material contrasts, weathered wood can possibly be prospected at greater depths than unweathered wood.

4.4.5 Comparison of Measurement Methods

For geoelectric measurements, sufficient material contrasts can be expected for hard and soft wood compared to all investigated embedding materials regardless of the structural orientation of the wood. With this method, cylindrical objects of diameters >2 m can be prospected in depths >3 m. The method is limited to the resolution of objects >0.5 m for depths of >0.5 m. However, the method can hardly distinguish between wood species and cutting directions. GPR is suitable for prospecting objects of 10 cm–50 cm diameter in depths of 1 m–3 m. There are limitations for the depth penetration of clayey soil. Under certain conditions (depending on the wood species, structural orientation of the wood, and embedding materials), material contrasts may be too low to be detected. The method is suitable to distinguish heterogeneities of wood species and structural orientation within an object. Seismic and GPR measurements show similar material contrasts. The major advantage of seismic measurements is the depth penetration in saline water, whereas GPR measurements are unsuccessful in this media. Limitations are possible in very shallow water and in gassy subsurfaces.

4.4.6 Conclusions

In our study, we define the scopes of application of geoelectrics and, GPR, supplemented by and seismics to prospect submerged wooden archaeological objects in a shallow water environment. Therefore, we had to experimentally determine changes in the dielectric permittivity and the electric resistivity of wooden samples for a large range of wood moisture contents. We systematically distinguish hard and soft woods as well as three main measuring axes with small-scale geophysical measurements. The dielectric permittivity increases by 90%, while the electric resistivity decreases by 90% with a 130% change in wood moisture content. When comparing the three main measuring axes, anisotropy effects of up to 30% for dielectric permittivity measurements and up to 15% for electric resistivity measurements occur. Different types of wood also account for a change of up to 20% in dielectric permittivity measurements and up to 30% in the electric resistivity measurements. The calculated material contrasts from

wood compared to the embedding materials (freshwater, saturated clay, and sand) show the potential of the methods to complement each other. ERT generally shows the highest material contrasts. Here, differences in wood species and structural orientation of the wood do not significantly affect the material contrasts. This is different with GPR measurements; here, material contrasts depend on the wood species and the structural orientation of the wood. GPR and seismic measurements show especially low contrasts of oak wood compared to saturated sand and of spruce wood compared to saturated clay. However, seismics is the preferable method in saline water. Depth estimates show that geoelectrics is particularly suitable for cylindrical objects (>0.8 m in diameter) at depths of >2 m and in a clayey environment. For spherical objects with diameters <0.8 m at depths of <2 m, the GPR prospection of wood embedded in saturated sand and freshwater with a 400 MHz antenna is suitable. In general, wood can be most successfully prospected in freshwater, followed by saturated clay and sand. For further investigations on the prospection of submerged archaeological wood, it will be necessary to calculate the material contrasts of weathered wood.

Author Contributions Conceptualization, A.F., D.W., T.W. and W.R.; methodology, A.F., D.W., T.W. and W.R.; software, A.F. and W.R.; validation, D.W. and T.W.; formal analysis, A.F.; investigation, A.F.; resources, A.F.; data curation, A.F.; writing—original draft preparation, A.F.; writing—review and editing, D.D, T.W. and W.R.; visualization, A.F., D.W.; supervision, D.W., T.W. and W.R.; project administration, W.R.; funding acquisition, D.W., T.W. and W.R. All authors have read and agreed to the published version of the manuscript.

Funding The research leading to these results has received funding by the German Research Foundation (DFG) in a project (RA 496/26-2) situated in the frame of the Priority Program 1630 ‘Harbours from the Roman Period to the Middle Ages’ (of Carnap-Bornheim and Kalmring 2011).

Acknowledgements Funding: The research leading to these results has received funding by the German Research Foundation (DFG) in a project (RA 496/26-2) situated in the frame of the Priority Program 1630 ‘Harbours from the Roman Period to the Middle Ages’ (of Carnap-Bornheim and Kalmring 2011). Acknowledgments: The authors acknowledge especially support from the student assistant Raphael Kahn with his help during the measurements. Stefan Dreibrodt offered his help using the kiln-drying method for the wood cubes. Special thanks is also dedicated to Thomas Günther (LIAG Hannover) for his support to use the program “pyGIMLi” to calculate the geometry factor of the wood cubes. The carpenter’s workshop “Stefan Wolter” provided and cut the wood cubes for free. We acknowledge financial support by DFG within the funding programme Open Access Publizieren.

Conflicts of Interest The authors declare no conflict of interest. The funders had no role in the design of the study; in the collection, analyses, or interpretation of data; in the writing of the manuscript, or in the decision to publish the results.

5 Conclusion

Geophysical prospection of archaeological issues in the littoral zone will continue to have an increasing importance in the upcoming years, since many underwater sites have not yet been surveyed or even discovered. This thesis might contribute to a more frequent application of geoelectrics and GPR commonly used on land to the water environment. The characteristics of the methods in this medium are now much better known than before and were compared to the most commonly used method seismics. The advantages of seismics (see below) in comparison to GPR and geoelectrics will remain, so it will continue to be the most widely used method. However, it is now possible to precisely quantify and classify the previously known limited sensitivity of GPR and geoelectrics in the water column. Thus, it is possible to use the methods under precisely defined conditions, primarily as an additional method to complement seismic measurements, or also on their own. For an evaluation of the methods, it was especially important to know in detail the physical properties of the materials to be prospected in the subsurface and to deduce the corresponding material contrasts. By focusing on the material wood, an important basis was set for the most frequently used archaeological building material in northern Europe. A similar approach would be useful for other materials such as bricks.

In the following, the most important advantages and disadvantages of the three measurement methods are summarised. This allows a first brief assessment of the choice of method for possible upcoming research issues, especially of wooden targets, in water. Previously known arguments are supplemented by the results from this thesis. The suitability of the methods for the detection of different material contrasts is additionally summarised in Table 5.1.

a) Seismics

Advantages:

- There is a high resolution in the cm-dm range with deep penetration >20 m (at a measurement frequency of 4 kHz).
- Almost all archaeological materials are resolvable (e.g. sand and stone, gyttia and wood).
- The data collection is fast, basic on-site evaluation is possible.
- Arrays can be used for area coverage and for resolution in the cm range across the profile direction.

Disadvantages:

- The analysis of data recorded in extremely shallow water depth <50 cm might be difficult due to multiples.
- In the presence of gas, there is no penetration of the method into the subsurface.
- The Equipment for using the method in water may not be available at small companies.
- The resolution of the material contrasts sand- clay, sand- wood and clay-wood is poor
- Ambiguities of reflection coefficients of water- peat and water-gyttia cause materials not to be addressed with certainty.

b) GeoelectricsAdvantages:

- The equipment and data evaluation scheme is partly known/available from land, only a (sub)water electrode streamer is required.
- Different measurement configurations and setups can be flexibly used depending on the research issue.
- The method is particularly well suited for the material contrasts sand- stone, clay- wood.
- Towed, floating electrode arrays are timesaving and show a spatial resolution on the sea-floor > 2 m for a conductivity of 0.3 Ωm with a water depth of 1 m. Submerged electrodes show a spatial resolution of 0.5 m–1 m for above conditions.
- Wooden objects with diameters of > 0.5 m can be detected at depths of > 0.5 m below the water surface.
- A Special evaluation scheme considers the specificities of water.

Disadvantages:

- An electrode streamer of more than 20 m is required, this needs lots of space and people to handle it.
- A spatial resolution in the cm range is hardly possible.
- The resolution of the material contrasts clay and sand as well as of various rock types with a porosity < 15% is poor.
- There is a high influence of the water column on the specific resistivity values in the subsurface, so that specific resistivity values in the subsurface or the true depth of objects could be incorrect.

- Ambiguities of reflection coefficients of sand-clay and sand-gyttia cause materials not to be addressed with certainty.
- The resolution of vertically complex structures or structures below high-resistance layers is poor.
- Due to the equivalence principle, it might not be possible to distinguish between 2, 3 or 4 layers.
- The water layer is challenging for inversion programs, a standard analysis is not sufficient (better proceed from 1D to 2D analysis and decide individually, whether and how a priori information is included).

c) Ground-penetrating radar

Advantages:

- The land equipment can be used quickly and without special knowledge in a water environment.
- There is a high resolution in the cm to dm range in profile direction, that can be reached across profile direction with an antenna array.
- The method is hardly affected by organic material in the water column.
- The method is particularly well-suited for material contrasts of freshwater-stone, sand-gyttia and clay-gyttia.
- A 400 MHz antenna is able to resolve wooden objects of 0.1 m–0.5 m diameter at a depth of 1 m–3 m below the water surface.
- The penetration depth of 1 m–3 m in fresh water could be enlarged by lowering the antenna.

Disadvantages:

- The penetration depth is low, especially at high salinities.
- The resolution of the material contrasts peat-gyttia, sand-clay and clay-wood is poor.
- Ambiguities of reflection coefficients of sand-stone and sand-wood cause materials not to be addressed with certainty.
- Multiples might occur in shallow water depth <50 cm.
- The spatial resolution in the dm-m range across profile direction is too low for archaeological prospection
- The use of an array or a lowered antenna to improve the spatial resolution or depth penetration might be very elaborately and therefore possibly ineffective.

Subsurface material contrasts	Geoelectrics	GPR	Seismics
Fresh water- Sand	✓	✓	✓
Fresh water- Clay	(✓)	✓	(✓)
Fresh water- Peat	✓	(✓)	✓
Fresh water- Gyttia	×	×	✓
Fresh water- Wood	✓	✓	✓
Fresh water- Granite	✓	✓	✓
Sand- Clay	(✓)	(✓)	(✓)
Sand- Peat	(✓)	✓	✓
Sand- Gyttia	✓	✓	✓
Sand- Wood	✓	(✓)	(✓)
Sand- Granite	✓	✓	✓
Clay- Peat	(✓)	(✓)	✓
Clay- Gyttia	✓	✓	✓
Clay- Wood	✓	(✓)	(✓)
Clay- Granite	✓	(✓)	✓
Peat- Gyttia	✓	(✓)	(✓)
Peat- Wood	✓	(✓)	✓
Peat- Granite	✓	✓	✓
Gyttia- Wood	✓	✓	✓
Gyttia- Granite	✓	✓	✓
Wood- Granite	✓	✓	✓

Table 5.1: The feasibility of the geophysical methods geoelectrics, GPR and seismics with regard to the prospection of different material contrasts in aquatic environments. There are checks for all materials with $|R| > 0.1$. When $|R|$ might be < 0.1 , the checks are parenthesised. For materials with $|R| < 0.1$, crosses are used.

6 Outlook

In this section, research ideas are presented that exceed the framework of this thesis and that might complement and improve the previous investigations. First, outlooks for the methods geoelectrics and GPR applied in the littoral zone are shown, before further possibilities to investigate and prospect the material wood are discussed. Finally, a possible application target is provided.

6.1 Geoelectrics

To investigate the application of geoelectrics in the littoral zone in this thesis, I used a Schlumberger configuration. Of course, other configurations are also possible here, which will bring quite different sensitivities with them. In addition, potential applications of a Schlumberger streamer were mainly investigated based on theoretical considerations, except for measurement uncertainties that were determined from field data. It is now essential to gather further experience with the practical application of the method, as well as to enhance and verify the conclusions regarding depth penetration, spatial resolution and the preferable measurement setup that were drawn from the theoretical considerations. This includes, for example, the handling of the measurement equipment with and without using a boat, as well as the prospection of targets of different dimensions, depth and materials. An application example is presented in section 6.4 more detailed. During the measurements, my suggested prospection scheme should be followed. Floating, and possibly towed electrodes should be used for overview profiles providing information on the subsurface material and water column, as well as for large-scale applications such as the resolutions of ground water upwelling areas below the sea bottom. Submerged electrodes should be used for detailed measurements of areas of interest, especially for the prospection of decimetre-scale archaeological constructions. These inversion results should be carefully supplemented with a priori information from the overview profiles.

In my thesis, I have considered geoelectric prospections in 1D and 2D. Further analysis should also include 2.5D and 3D prospections, in particular for complex structures, both in and across the profile. This leads to the question of the required distance between measurement profiles in order to track objects over several profiles. Furthermore, it has to be investigated to what extent this distance can be realized using the three measurement setups. For shore-parallel measurements, I noted that with an inclined seabed, the water volume to the sides of the measurement profile is different. An evaluation of these profiles would require some analysis of whether the vicinity to

the beach affects the measured data and how the results can be corrected if appropriate.

The large resistivity contrast between the water column and the sea bottom is challenging for the inversion of geoelectric data that was prospected in the littoral zone. Thus, the choice of an appropriate inversion software is essential. The software should provide reasonable inversion results which are not affected by boundary effects, without specifying a priori information on the water column for floating electrodes. At the same time, for the evaluation of submerged electrodes, a transparent specification of a priori information (in order to test each parameter specification individually) in the inversion process is required. It is particularly important that the specification of the water depth is not necessarily related to the specification of the water resistivity. So far I observed strengths and weaknesses in the programs RES2DINV (Loke and Barker, 1996) and BERT (Rücker et al., 2006; Günther et al., 2006) regarding the two aspects, a further evaluation of the established inversion programs should be done.

The approach used in my study is not only relevant for meter-scale, respectively archaeological targets. It can easily be transferred to issues of a larger dimensions in water depths >5 m, e.g. issues on the stratigraphy or freshwater upwelling in the sub bottom. For an increased depth of the water column, preliminary considerations are essential concerning these targets as well.

6.2 Ground-Penetrating Radar

After I used four exemplary measurement locations to theoretically analyse the use of GPR for archaeological prospection in water, further studies should focus on possible targets and gain experience with them. Especially after we have theoretically determined the material contrasts to be expected for the prospection of archaeological targets in water with GPR, these should also be verified in practice.

A challenge that could be seen in a radargram with a very low water column < 50 cm and a high reflection coefficient at the river surface due to sand and pebbles is the occurrence of multiples. Here, it is necessary to consider how these should be dealt with. Approaches from seismic investigations could be followed, e.g. (Schwardt et al., 2021).

My study showed that organic material can be well imaged in the water column. In addition, the bottom of the water hardly shows any deviations in the amplitudes, regardless of whether material is found in the water column or not. This indicates that the method is well suited for both documenting and possibly quantifying the siltation of lakes. This would require a concept of how the amplitudes can be calibrated with the actual organic mass, of course taking into account scattering effects. In addition to archaeological prospection, this may provide a new field of application for GPR in water.

Both the resolution across profile direction and the penetration depth in water might

be improved. The resolution across the profile direction would be significantly improved by using a GPR array. The penetration depth could be improved by reducing the water column by lowering the antenna. Both would imply a considerable technical effort that would require a reconsideration of how a GPR array could be manoeuvred and controlled on the water or possibly even under the water. The increased effort should be reasonable for the respective problem.

6.3 Material contrasts of wood

For the investigations on the prospection of wood in aquatic environments, in this thesis archaeological wood was approximated by modern, freshwater-saturated wood. This experiment could be repeated using salt water to determine material contrasts of wooden objects in the sea. In this case, only geoelectric material contrasts have to be considered, as the high attenuation due to salt water does not allow the application of GPR. Further useful approaches would include the influence of the weathering degree and measurements on excavated archaeological woods in order to map and quantify its characteristics. A similar procedure is already known from studies determining seismic velocities of archaeological woods (Dix et al., 2001; Arnott et al., 2005). The final step would consider the prospection of archaeological woods of different sizes and orientations in situ.

Weathering of wood has various sources (e.g. bacteria, mushrooms) and the degree of weathering can be classified in different ways. It correlates to the density of fully water-saturated wood. Thus, the laboratory experiment in which the physical parameters electrical resistivity and dielectric permittivity were determined depending on the water saturation could be continued. Hence, in case of a full water saturation of the wood pieces the parameter's dependence on the wood density could be determined. An acceleration of the weathering process, e.g. by adding bacteria or fungi should be considered. I expect lower specific resistivity and higher dielectric permittivity values for weathered wood, so that the material contrasts decrease to fresh water and possibly increase to saturated clayey and sandy soils. The influences of anisotropy directions and wood species remain to be examined.

To determine the physical parameters of excavated archaeological woods, it must be considered that excavated wood shows a great variability regarding age, wood species, weathering and cutting direction. Thus, a sufficient number of samples of each category must be examined in order to obtain a reliable result. This is very time-consuming because all categories must be taken into account, but are not necessarily known after the excavation or when the wood is stored in a water basin until conservation (e.g. the type of wood and its density). In contrast to my experiment, the wood pieces are not cubic and cannot be cut. Besides the mass of the wood, the volume, which is essential to know for calculating the wood density, must be determined with a 3D scanner, for example. However, the scanning of wet wood is difficult, so that the wooden surfaces would have to be dried. Another problem is the unknown dry mass of the wood. It is therefore not known, to what extent the weathering degree of the wood, the tree

growth or possible air inclusions have an influence on the current density. A full water saturation of the wood must be ensured for conclusions on the weathering degree, but the larger the object, the less likely is a full water saturation. After the excavation of archaeological wood, the degree of saturation is not known and usually the wood is not stored in the water tanks for long enough to exclude air inclusions and to achieve complete water saturation. All in all, to minimize the effort in determining the physical parameters of excavated archaeological woods, a reasonable approach must carefully be chosen and adapted to the scope of possibilities.

The last step includes measurements of archaeological woods in situ with different sizes, orientations and in various surrounding material with the methods geoelectrics and GPR. Again, it must be taken into account that the wood might be weathered, but not necessarily fully saturated with water.

6.4 Example of application: A Viking age ship in Hadebyer Noor, Schleswig, Germany

In chapters 2 to 4 I have mostly theoretically investigated the application of geoelectrics and GPR in the littoral zone with a specific focus on the prospection of archaeological wooden targets. In the last step I would like to give an outlook on the prospection of a target, in which the theoretical considerations could be synthesised and first results may be promising. It is an in situ well preserved cargo ship from the Viking Age, the so called "Wreck III" that is well investigated from diving exploration (Kramer, 2000). It is located in the "Hadebyer Noor", a brackish water bulge (specific resistivity of averagely 1 Ωm of the Schlei close to the well-known Viking settlement Haithabu, Schleswig, Germany (see Figure 6.1). The ship was built in the local area from oak wood, is 22 m long, 5.5 m wide and about 80 cm high. It is situated at a depth of 2.2 m–3.12 m below the water surface and partially rises from the soil into the water column. In the surrounding area there are also poles and other in situ findings of various wooden structures.

The most commonly used method, seismics, is well suited for this objective, both in terms of depth penetration and spatial resolution. Therefore, seismic reflection measurements (for profile location see Figure 6.1) were carried out with a 3D "Ping-Pong" array (Wilken et al., 2019). However, the material contrast between the oak ship wreck and the surrounding presumably muddy soil might be difficult to resolve according to Arnott et al. (2005). This also would explain the results of Figure 6.2a, in which the shipwreck shows only slight anomalies. However, the bathymetry results as secondary information could be useful for further investigations with geoelectrics. I used this method as the second, which is suitable both in terms of spatial resolution and the material contrasts to be expected, since the application of GPR is unpromising due to the salinity of the water. However, it is possible that the depth penetration of geoelectrics is critical or that the true depth of the target is distorted. Here, the inverse Schlumberger streamer with length and configuration of chapter 2 was chosen.

To achieve a higher sensitivity in the bottom, the electrodes were lowered by 1 m in the water column. The towed profile can be seen in Figure 6.1b). First results were obtained with the inversion program BERT (Rücker et al., 2006; Günther et al., 2006) without providing a priori information. An anomaly of increased resistivity of $4\ \Omega\text{m}$ compared to the surrounding bottom resistivity of $2\ \Omega\text{m}$ can be observed at the location where the wreck has been roughly located by divers (Figure 6.2). The result was confirmed by repetition profiles. No similar anomalies were observed in the geoelectric profiles in the surrounding environment. However, since the anomaly is much deeper than known, further processing and analysis of the data is required to verify the preliminary results. In the next step, the bathymetry should be included as a priori information in the inversion and compared to the previous results. This should confirm whether the anomalies are caused by the material of the subsoil or by the shipwreck whose true depth could be better estimated then as well. The measurements should also be repeated with stationary, totally submerged electrodes, as the best resolution can be expected here. This example shows how important the combination of methods is in the water and how seismics in this case can provide a priori information for geoelectrics, that might resolve the material contrast from the shipwreck to the bottom, but cannot provide its real depth.

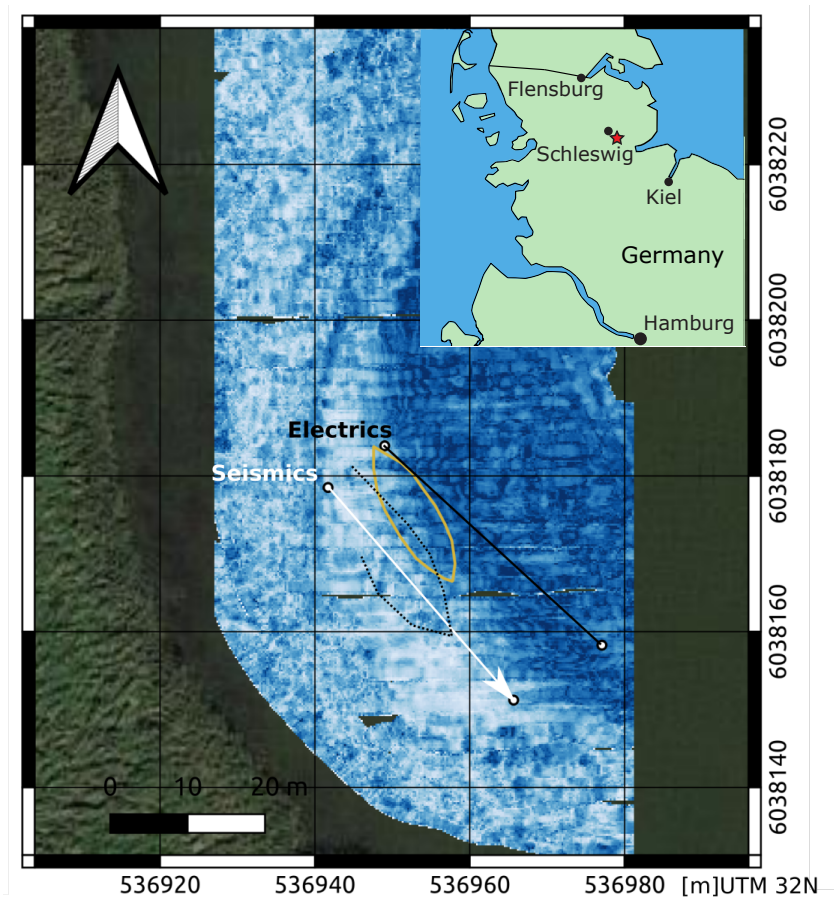


Figure 6.1: Location of Haithabu (red star) near Schleswig in Germany and detailed map of the location of "wreck III" in the Hedeby Noor (Kramer, 2000) (coloured orange). The geoelectric profile is coloured black, the seismic profile is coloured white.

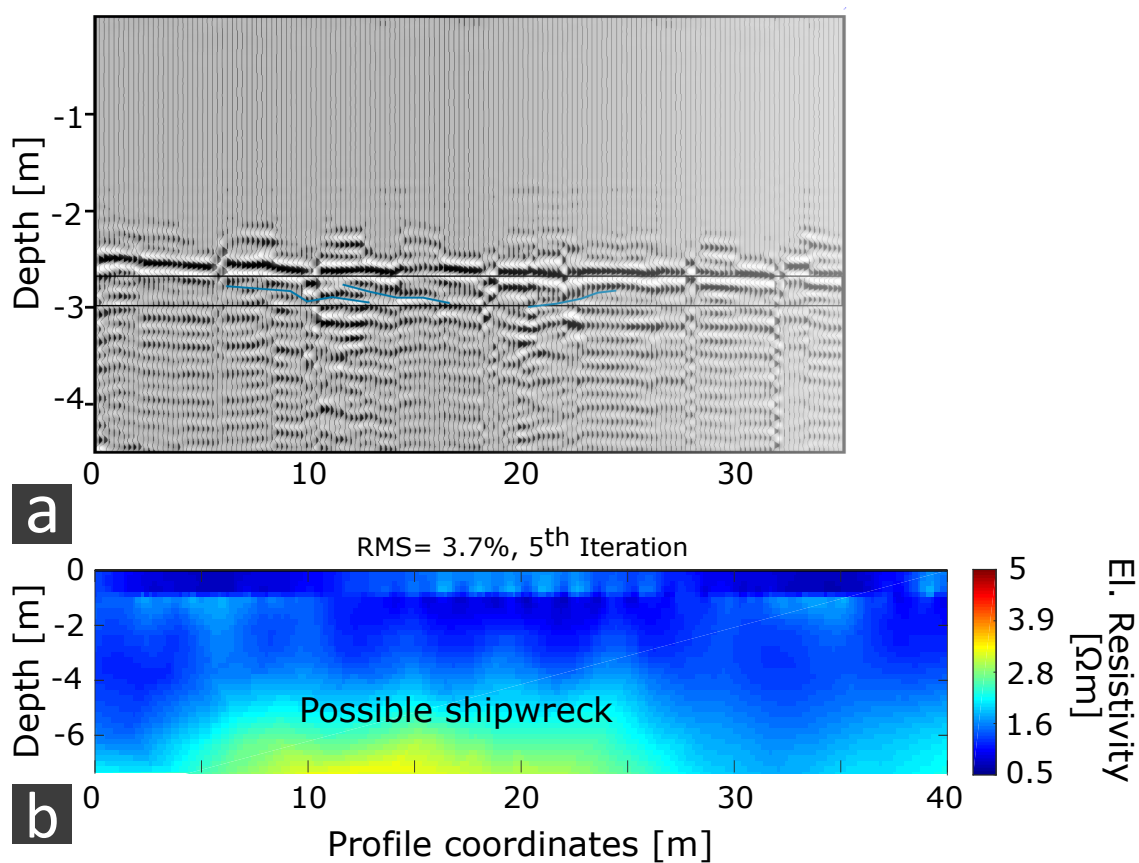


Figure 6.2: a) Seismic profile (white line in Figure 6.1), crossing the "wreck III". A 3D "Ping-Pong" array (Wilken et al., 2019) was used. b) Geoelectric profile (black line in Figure 6.1), that crosses the "wreck III". A 20 m long inverse Schlumberger configuration was used, whose electrodes were lowered 1m into the water column.

Bibliography

- Abramov, A. and Vasiliev, A. (2004). Underwater ground penetrating radar in archaeological investigation below sea bottom. In *Proceedings of the Tenth International Conference on Grounds Penetrating Radar, 2004. GPR 2004.*, pages 455–458. IEEE.
- Annan, A. (2005). Ground-penetrating radar. In *Near-surface geophysics*, pages 357–438. Society of Exploration Geophysicists.
- Annan, A. and Davis, J. (1977). Impulse radar applied to ice thickness measurements and freshwater bathymetry. *Geological Survey of Canada, Report of Activities Paper*, pages 117–124.
- Annan, A., Davis, J., et al. (1977). Radar range analysis for geological materials. *Geological Survey of Canada*, 77(1B):117–124.
- Annan, P. (2003). Ground penetrating radar principles, procedures and applications. *Sensors and software*, 278.
- Archie, G. E. et al. (1942). The electrical resistivity log as an aid in determining some reservoir characteristics. *Transactions of the AIME*, 146(01):54–62.
- Arcone, S., Finnegan, D., and Boitnott, G. (2010). Gpr characterization of a lacustrine uxo site. *Geophysics*, 75(4):WA221–WA239.
- Arcone, S., Grant, S., Boitnott, G., and Bostick, B. (2008). Complex permittivity and clay mineralogy of grain-size fractions in a wet silt soil. *Geophysics*, 73(3):J1–J13.
- Arcone, S. A. (1995). Numerical studies of the radiation patterns of resistively loaded dipoles. *Journal of Applied Geophysics*, 33(1-3):39–52.
- Arcone, S. A., Chacho Jr, E. F., and Delaney, A. J. (1992). Short-pulse radar detection of groundwater in the sagavanirktok river floodplain in early spring. *Water Resources Research*, 28(11):2925–2936.
- Arnott, S. H., Dix, J. K., Best, A. I., and Gregory, D. J. (2005). Imaging of buried archaeological materials: The reflection properties of archaeological wood. *Marine Geophysical Researches*, 26(2-4):135–144.
- Avnimelech, Y., Ritvo, G., Meijer, L. E., and Kochba, M. (2001). Water content, organic carbon and dry bulk density in flooded sediments. *Aquacultural engineering*, 25(1):25–33.
- Bartsch, H.-J. (1982). *Taschenbuch mathematischer Formeln*. Number BOOK. Verlag Harri Deutsch.

- Baumgartner, F. (1996). A new method for geoelectrical investigations underwater 1. *Geophysical Prospecting*, 44(1):71–98.
- Beblo, M. (1997). *Umweltgeophysik*. Ernst & Sohn.
- Bevan, B. (1977). Ground-penetrating radar at valley forge. *Geophysical Survey System, North Salem, New Hampshire*.
- Bhattacharya, P. and Patra, H. (1968). Direct current geoelectric, sounding methods in geochemistry and geophysics.
- Blakely, R. J. (1996). *Potential theory in gravity and magnetic applications*. Cambridge university press.
- Bowers, R. J. and Bidwell, B. A. (1999). Geophysics and uxo detection. *The Leading Edge*, 18(12):1389–1391.
- Boyce, J. I., Reinhardt, E. G., Raban, A., and Pozza, M. R. (2004). Marine magnetic survey of a submerged roman harbour, caesarea maritima, israel. *International Journal of Nautical Archaeology*, 33(1):122–136.
- Bull, J. M., Gutowski, M., Dix, J. K., Henstock, T. J., Hogarth, P., Leighton, T. G., and White, P. R. (2005). Design of a 3d chirp sub-bottom imaging system. *Marine Geophysical Researches*, 26(2):157–169.
- Butler, D. K. (1997). Landmines and uxo. *The Leading Edge*, 16(10):1460–1460.
- Butler, D. K. (2005). *Near-surface geophysics*. Number 13. SEG Books.
- Buynovich, I. V. and Fitzgerald, D. M. (2003). High-resolution subsurface (gpr) imaging and sedimentology of coastal ponds, maine, usa: implications for holocene back-barrier evolution. *Journal of Sedimentary Research*, 73(4):559–571.
- Corradini, E., Dreibrodt, S., Erkul, E., Groß, D., Lübke, H., Panning, D., Pickartz, N., Thorwart, M., Vött, A., Willershäuser, T., et al. (2020). Understanding wetlands stratigraphy: Geophysics and soil parameters for investigating ancient basin development at lake duvensee. *Geosciences*, 10(8):314.
- Costa, J., Cheng, R., Haeni, F., Melcher, N., Spicer, K., Hayes, E., Plant, W., Hayes, K., Teague, C., and Barrick, D. (2006). Use of radars to monitor stream discharge by noncontact methods. *Water Resources Research*, 42(7).
- Crumlin-Pedersen, O. (2004). Nordic clinker construction. *The philosophy of shipbuilding. Conceptual approaches to the study of wooden ships*, pages 37–64.
- Davis, J. L. and ANNAN, A. P. (1989). Ground-penetrating radar for high-resolution mapping of soil and rock stratigraphy 1. *Geophysical prospecting*, 37(5):531–551.
- Delaney, A. J., Sellmann, P. V., and Arcone, S. A. (1992). Sub-bottom profiling: a comparison of short-pulse radar and acoustic data. In *Fourth International Conference on Ground Penetrating Radar*, pages cp–303. European Association of Geoscientists & Engineers.

- Diener, A. (2012). Holzbau in mittelalter und neuzeit. *Mitteilungen der Deutschen Gesellschaft für Archäologie des Mittelalters und der Neuzeit*.
- Dix, J., Arnott, S., Best, A., and Gregory, D. (2001). The acoustic characteristics of marine archaeological wood.
- Fassbinder, J. W. (2009). *Geophysikalische Prospektionsmethoden—Chancen für das archäologische Erbe*. na.
- Fediuk, A., Wilken, D., Thorwart, M., Wunderlich, T., Erkul, E., and Rabbel, W. (2020a). The applicability of an inverse schlumberger array for near-surface targets in shallow water environments. *Remote Sensing*, 12(13):2132.
- Fediuk, A., Wilken, D., Wunderlich, T., and Rabbel, W. (2020b). Physical parameters and contrasts of wooden objects in lacustrine environment: Ground penetrating radar and geoelectrics. *Geosciences*, 10(4):146.
- Fediuk, A., Wilken, D., Wunderlich, T., Rabbel, W., Seeliger, M., Laufer, E., and Pirson, F. (2019). Marine seismic investigation of the ancient kane harbour bay, turkey. *Quaternary International*, 511:43–50.
- Fuchs, M., Beres, M., and Anselmetti, F. S. (2004). Sedimentological studies of western swiss lakes with high-resolution reflection seismic and amphibious gpr profiling. In *Proceedings of the Tenth International Conference on Grounds Penetrating Radar, 2004. GPR 2004.*, pages 577–580. IEEE.
- Goddio, F. (1998). *Alexandria: the submerged royal quarters*. Periplus.
- Gorin, S. and Haeni, F. (1989). *Use of surface-geophysical methods to assess riverbed scour at bridge piers*, volume 88. Department of the Interior, US Geological Survey.
- Grøn, O., Boldreel, L. O., Cvikel, D., Kahanov, Y., Galili, E., Hermand, J.-P., Nævestad, D., and Reitan, M. (2015). Detection and mapping of shipwrecks embedded in sea-floor sediments. *Journal of Archaeological Science: Reports*, 4:242–251.
- GRØN, O., JØRGENSEN, A. N., and HOFFMANN, G. (2007). Marine archaeological survey by high-resolution sub-bottom profilers.
- Günther, T., Rücker, C., and Spitzer, K. (2006). Three-dimensional modelling and inversion of dc resistivity data incorporating topography—ii. inversion. *Geophysical Journal International*, 166(2):506–517.
- Gutowski, M., Bull, J. M., Dix, J. K., Henstock, T. J., Hogarth, P., Hiller, T., Leighton, T. G., and White, P. R. (2008). 3d high-resolution acoustic imaging of the sub-seabed. *Applied Acoustics*, 69(3):262–271.
- Hilterman, F. (1975). Amplitudes of seismic waves; a quick look. *Geophysics*, 40(5):745–762.
- James, W. L. (1975). *Dielectric properties of wood and hardboard: variation with temperature, frequency, moisture content, and grain orientation*, volume 245. Department of Agriculture, Forest Service, Forest Products Laboratory.

- Johnson, T. (2004). Chris gaffney & john gater. revealing the buried past: geophysics for archaeologists. *Antiquity*, 78(301):740–742.
- Jol, H. M. and Albrecht, A. (2004). Searching for submerged lumber with ground penetrating radar: Rib lake, wisconsin, usa. In *Proceedings of the Tenth International Conference on Grounds Penetrating Radar, 2004. GPR 2004.*, pages 601–604. IEEE.
- Kaatze, U. (1989). Complex permittivity of water as a function of frequency and temperature. *Journal of Chemical and Engineering Data*, 34(4):371–374.
- Kenyon, J. L. and Bevan, B. (1977). Ground-penetrating radar and its application to a historical archaeological site. *Historical Archaeology*, 11(1):48–55.
- Klein, C. (2011). Geophysical investigations in shallow water at the harbor site of elaiia: Harbor city of the ancient pergamon. In *Proceedings of the 9th International Conference on Archaeological Prospection, Izmir, Turkey*, pages 19–24.
- Knödel, K., Krummel, H., and Lange, G. (2013). *Handbuch zur Erkundung des Untergrundes von Deponien und Altlasten: Band 3: Geophysik*. Springer-Verlag.
- Kollmann, F. F. (1968). Physics of wood. In *Principles of wood science and technology*, pages 160–291. Springer.
- Kovacs, A. (1991). Impulse radar bathymetric profiling in weed-infested fresh water. Technical report, COLD REGIONS RESEARCH AND ENGINEERING LAB HANOVER NH.
- Kovacs, A., Morey, R. M., et al. (1985). Electromagnetic measurements of multi-year sea ice using impulse radar.
- Kramer, W. (2000). Highend archaeologie.
- Kritikakis, G., Papadopoulos, N., Simyrdanis, K., and Theodoulou, T. (2015). Imaging of shallow underwater ancient ruins with ert and seismic methods. In *8th Congress of the Balkan Geophysical Society*, volume 2015, pages 1–5. European Association of Geoscientists & Engineers.
- Kröner, K. and Pungs, L. (1952). Zur dielektrischen anisotropie des naturholzes im großen frequenzbereich. *Holzforschung-International Journal of the Biology, Chemistry, Physics and Technology of Wood*, 6(1):13–16.
- Kuroda, N. and Tsutsumi, J. (1982). Anisotropic behaviour of electrical conduction in wood. *Mokuzai Gakkaishi= Journal of the Japan Wood Research Society*.
- Kwon, H.-S., Kim, J.-H., Ahn, H.-Y., Yoon, J.-S., Kim, K.-S., Jung, C.-K., Lee, S.-B., and Uchida, T. (2005). Delineation of a fault zone beneath a riverbed by an electrical resistivity survey using a floating streamer cable. *Exploration Geophysics*, 36(1):50–58.
- Lagabrielle, R. (1983). The effect of water on direct current resistivity measurement from the sea, river or lake floor. *Geoexploration*, 21(2):165–170.

- Le Borgne, E. (1955). Susceptibilité magnétique anormale du sol superficiel. *Ann. Geophys.*, pages 399–419.
- Leckebusch, J. (1998). Georadar in binnengewässern. *Archäologie unter Wasser*, 2:51–57.
- Lin, R. T.-t. et al. (1965). study of electrical conduction in wood.
- Lin, Y.-T., Wu, C., Fratta, D., and Kung, K.-J. (2010). An integrated acoustic and electromagnetic wave-based technique to estimate subbottom sediment properties in a freshwater environment. *Near surface geophysics*, 8(3):213–221.
- Linington, R. E. (1963). The application of geophysics to archaeology. *American Scientist*, 51(1):48–70.
- Loke, M. (2002). Res2dmod ver. 3.01. *Rapid 2D resistivity forward modelling using the finite-difference and finite-elements method*. Geotomo Software. Manual.
- Loke, M. and Barker, R. (1996). Rapid least-square inversion of apparent resistivity pseudosections by a quasi-newton method. *Geophys. Prospect*, 44:13.
- Loke, M., Chambers, J., Rucker, D., Kuras, O., and Wilkinson, P. (2013). Recent developments in the direct-current geoelectrical imaging method. *Journal of applied geophysics*, 95:135–156.
- Manheim, F. T., Krantz, D. E., and Bratton, J. F. (2004). Studying ground water under delmarva coastal bays using electrical resistivity. *Groundwater*, 42(7):1052–1068.
- Mansoor, N. and Slater, L. (2007). Aquatic electrical resistivity imaging of shallow-water wetlands. *Geophysics*, 72(5):F211–F221.
- Mavko, G., Mukerji, T., and Dvorkin, J. (2020). *The rock physics handbook*. Cambridge university press.
- McGrail, S. (2014). *Ancient Boats in North-West Europe: The archaeology of water transport to AD 1500*. Routledge.
- McKee, A. (1973). The search for king henry viii's 'mary rose'. *Marine Archaeology*, pages 185–202.
- Mellett, J. S. (1995). Ground penetrating radar applications in engineering, environmental management, and geology. *Journal of Applied Geophysics*, 33(1-3):157–166.
- Menounos, B. (1997). The water content of lake sediments and its relationship to other physical parameters: an alpine case study. *The Holocene*, 7(2):207–212.
- Millonas, M. (1994). Swarms, phase transitions, and collective intelligence. *Proc. Artificial Life*.
- Mommsen, H. (1986). Archäometrische prospektion. In *Archäometrie*, pages 15–64. Springer.

- Moorman, B. J. and Michel, F. A. (1997). Bathymetric mapping and sub-bottom profiling through lake ice with ground-penetrating radar. *Journal of Paleolimnology*, 18(1):61–73.
- Müller, C., Woelz, S., Ersoy, Y., Boyce, J., Jokisch, T., Wendt, G., and Rabbel, W. (2009). Ultra-high-resolution marine 2d–3d seismic investigation of the liman tepe/karantina island archaeological site (urla/turkey). *Journal of Applied Geophysics*, 68(1):124–134.
- Niemz, P. and Sonderegger, W. (2017). *Holzphysik: Physik des Holzes und der Holzwerkstoffe*. Carl Hanser Verlag GmbH Co KG.
- Okyar, M., Yilmaz, S., Tezcan, D., and Çavaş, H. (2013). Continuous resistivity profiling survey in mersin harbour, northeastern mediterranean sea. *Marine Geophysical Research*, 34(2):127–136.
- Orlando, L. (2013). Some considerations on electrical resistivity imaging for characterization of waterbed sediments. *Journal of Applied Geophysics*, 95:77–89.
- Papadopoulos, N., Simyrdanis, K., and Theodoulou, T. (2016). Reconstructing the cultural dynamics of shallow marine archeological sites through electrical resistivity tomography. In *Near Surface Geoscience 2016-22nd European Meeting of Environmental and Engineering Geophysics*, volume 2016, pages cp–495. European Association of Geoscientists & Engineers.
- Parasnis, D. S. (2012). *Principles of applied geophysics*. Springer Science & Business Media.
- Park, I., Lee, J., and Cho, W. (2004). Assessment of bridge scour and riverbed variation by a ground penetrating radar. In *Proceedings of the Tenth International Conference on Grounds Penetrating Radar, 2004. GPR 2004.*, volume 1, pages 411–414. IEEE.
- Passaro, S. (2010). Marine electrical resistivity tomography for shipwreck detection in very shallow water: a case study from agropoli (salerno, southern italy). *Journal of Archaeological Science*, 37(8):1989–1998.
- Peyskens, E., De Pourcq, M., Stevens, M., and Schalck, J. (1984). Dielectric properties of softwood species at microwave frequencies. *Wood Science and Technology*, 18(4):267–280.
- Plets, R. M., Dix, J. K., Adams, J. R., Bull, J. M., Henstock, T. J., Gutowski, M., and Best, A. I. (2009). The use of a high-resolution 3d chirp sub-bottom profiler for the reconstruction of the shallow water archaeological site of the grace dieu (1439), river hamble, uk. *Journal of Archaeological Science*, 36(2):408–418.
- Porsani, J. L., Assine, M. L., and Moutinho, L. (2005). Application of gpr in the study of a modern alluvial megafan: the case of the taquari river in pantanal wetland, west-central brazil. *Subsurface Sensing Technologies and Applications*, 6(2):219–233.
- Powers, C., Haeni, F., and Smith, S. (1999). Integrated use of continuous seismic-reflection profiling and ground-penetrating radar methods at john’s pond, cape cod,

- massachusetts. In *12th EEGS Symposium on the Application of Geophysics to Engineering and Environmental Problems*, pages cp–202. European Association of Geoscientists & Engineers.
- Rücker, C., Günther, T., and Spitzer, K. (2006). Three-dimensional modelling and inversion of dc resistivity data incorporating topography—i. modelling. *Geophysical Journal International*, 166(2):495–505.
- Rücker, C., Günther, T., and Wagner, F. (2016). pygimli—an open source python library for inversion and modelling in geophysics. In *78th EAGE Conference and Exhibition 2016*, volume 2016, pages 1–2. European Association of Geoscientists & Engineers.
- Ruffell, A. (2006). Under-water scene investigation using ground penetrating radar (gpr) in the search for a sunken jet ski, northern ireland. *Science & Justice*, 46(4):221–230.
- Ruffell, A. (2014). Lacustrine flow (divers, side scan sonar, hydrogeology, water penetrating radar) used to understand the location of a drowned person. *Journal of hydrology*, 513:164–168.
- Sambuelli, L. and Bava, S. (2012). Case study: A gpr survey on a morainic lake in northern italy for bathymetry, water volume and sediment characterization. *Journal of Applied Geophysics*, 81:48–56.
- Sambuelli, L., Calzoni, C., and Pesenti, M. (2009). Waterborne gpr survey for estimating bottom-sediment variability: A survey on the po river, turin, italy. *Geophysics*, 74(4):B95–B102.
- Schön, J. (1983). *Petrophysik: Physikalische eigenschaften von gesteinen und mineralen*. Akademie-Verlag Berlin.
- Schwamborn, G., Dix, J., Bull, J., and Rachold, V. (2002). High-resolution seismic and ground penetrating radar–geophysical profiling of a thermokarst lake in the western lena delta, northern siberia. *Permafrost and Periglacial Processes*, 13(4):259–269.
- Schwan, H., Sheppard, R., and Grant, E. (1976). Complex permittivity of water at 25° c. *The Journal of Chemical Physics*, 64(5):2257–2258.
- Schwardt, M., Wilken, D., and Rabbel, W. (2021). Attenuation of seismic multiples in very shallow water: An application in archaeological prospection using data driven approaches. *Remote Sensing*, 13(10):1871.
- Scollar, I., Tabbagh, A., Hesse, A., and Herzog, I. (1990). *Archaeological prospecting and remote sensing*.
- Seeliger, M., Bartz, M., Erkul, E., Feuser, S., Kelterbaum, D., Klein, C., Pirson, F., Vött, A., and Brückner, H. (2013). Taken from the sea, reclaimed by the sea: The fate of the closed harbour of elaiia, the maritime satellite city of pergamum (turkey). *Quaternary International*, 312:70–83.
- Seeliger, M., Brill, D., Feuser, S., Bartz, M., Erkul, E., Kelterbaum, D., Vött, A., Klein,

- C., Pirson, F., and Brückner, H. (2014). The purpose and age of underwater walls in the bay of elaiia of western turkey: a multidisciplinary approach. *Geoarchaeology*, 29(2):138–155.
- Sellmann, P. V., Delaney, A. J., and Arcone, S. A. (1992). Sub-bottom surveying in lakes with ground-penetrating radar. Technical report, COLD REGIONS RESEARCH AND ENGINEERING LAB HANOVER NH.
- Shields, G., Grossman, S., and Humphrey, A. (2004). Waterborne geophysical surveys on shallow river impoundments. In *17th EEGS Symposium on the Application of Geophysics to Engineering and Environmental Problems*, pages cp–186. European Association of Geoscientists & Engineers.
- Simyrdanis, K., Moffat, I., Papadopoulos, N., Kowlessar, J., and Bailey, M. (2018). 3d mapping of the submerged crowie barge using electrical resistivity tomography. *International Journal of Geophysics*, 2018.
- Simyrdanis, K., Papadopoulos, N., and Cantoro, G. (2016). Shallow off-shore archaeological prospection with 3-d electrical resistivity tomography: The case of olous (modern elounda), greece. *Remote Sensing*, 8(11):897.
- Simyrdanis, K., Papadopoulos, N., Kim, J.-H., Tsourlos, P., and Moffat, I. (2015). Archaeological investigations in the shallow seawater environment with electrical resistivity tomography. *Near Surface Geophysics*, 13(6):601–611.
- Skaar, C. (2012). *Wood-water relations*. Springer Science & Business Media.
- Smith, G. (1984). Directive properties of antennas for transmission into a material half-space. *IEEE transactions on antennas and propagation*, 32(3):232–246.
- Snyder, D. D. and Wightman, W. E. (2002). Application of continuous resistivity profiling to aquifer characterization. In *Symposium on the Application of Geophysics to Engineering and Environmental Problems 2002*, pages GSL10–GSL10. Society of Exploration Geophysicists.
- Stamm, A. J. (1927). The electrical resistance of wood as a measure of its moisture content. *Industrial & Engineering Chemistry*, 19(9):1021–1025.
- Stevens, C. W., Moorman, B. J., and Solomon, S. M. (2008). Detection of frozen and unfrozen interfaces with ground penetrating radar in the nearshore zone of the mackenzie delta, canada. In *Proceedings of the Ninth International Conference on Permafrost, Fairbanks, AK, USA*, volume 29.
- Stümpel, H. (1988). Erdradar: Ein neues prospektionsverfahren in der archäologie. *Archäologie in Deutschland*, (1):28–31.
- Stümpel, H. and Meissner, R. (1982). Haithabu—entdeckung neuer funde durch hochauflösende kleinseismische messungen. *Naturwissenschaften*, 69(8):353–360.
- Telford, W. M., Telford, W., Geldart, L., Sheriff, R. E., and Sheriff, R. (1990). *Applied geophysics*. Cambridge university press.

- Töpfer, K. (1969). Die ortung von störkörpern mit dem schlumberger-meßverfahren. *Archiv für Meteorologie, Geophysik und Bioklimatologie, Serie A*, 18(1-2):191–220.
- Trapp, v. W. and Pungs, L. (1956). Einfluß von temperatur und feuchte auf das dielektrische verhalten von naturholz im großen frequenzbereich. *Holzforschung-International Journal of the Biology, Chemistry, Physics and Technology of Wood*, 10(5):144–150.
- Vickers, R. S. and Dolphin, L. T. (1975). A communication on an archaeological radar experiment at chaco canyon, new mexico. *MASCA newsletter*, 11(1):3–3.
- Waite, A. H. and Schmidt, S. J. (1962). Gross errors in height indication from pulsed radar altimeters operating over thick ice or snow. *Proceedings of the IRE*, 50(6):1515–1520.
- Wensink, W., Greeuw, G., Hofman, J., and Van Deen, J. (1990). Measured underwater near-field e-patterns of a pulsed, horizontal dipole antenna in air: Comparison with the theory of the continuous wave, infinitesimal electric dipole1. *Geophysical Prospecting*, 38(7):805–830.
- Whiticar, M. J., Faber, E., and Schoell, M. (1986). Biogenic methane formation in marine and freshwater environments: Co₂ reduction vs. acetate fermentation—isotope evidence. *Geochimica et Cosmochimica Acta*, 50(5):693–709.
- Wightman, W., Jalinoos, F., Hanna, K., Sirles, P., et al. (2003). Application of geophysical methods to highway related problems. Technical report, United States. Federal Highway Administration.
- Wilken, D. and Rabbel, W. (2012). On the application of particle swarm optimization strategies on scholte-wave inversion. *Geophysical Journal International*, 190(1):580–594.
- Wilken, D., Wunderlich, T., Hollmann, H., Schwaradt, M., Rabbel, W., Mohr, C., Schulte-Kortnack, D., Nakoinz, O., Enzmann, J., Jürgens, F., et al. (2019). Imaging a medieval shipwreck with the new pingpong 3d marine reflection seismic system. *Archaeological Prospection*, 26(3):211–223.
- Woelz, S., Erkul, E., Rabbel, W., and Stümpel, H. (2004). Multisensor-a mobile geophysical multi-sensor system for archaeological prospecting. In *Near Surface 2004-10th EAGE European Meeting of Environmental and Engineering Geophysics*, pages cp–10. European Association of Geoscientists & Engineers.
- Woelz, S., Rabbel, W., and Mueller, C. (2009). Shear waves in near surface 3d media-sh-wavefield separation, refraction time migration and tomography. *Journal of Applied Geophysics*, 68(1):104–116.
- Wunderlich, T. and Rabbel, W. (2013). Absorption and frequency shift of gpr signals in sandy and silty soils: empirical relations between quality factor q, complex permittivity and clay and water contents. *Near Surface Geophysics*, 11(2):117–128.

- Wunderlich, T., Wilken, D., Andersen, J., Rabbel, W., Zori, D., Kalmring, S., and Byock, J. (2015a). On the ability of geophysical methods to image medieval turf buildings in iceland. *Archaeological Prospection*, 22(3):171–186.
- Wunderlich, T., Wilken, D., Erkul, E., Rabbel, W., Vött, A., Fischer, P., Hadler, H., and Heinzelmann, M. (2018). The river harbour of ostia antica-stratigraphy, extent and harbour infrastructure from combined geophysical measurements and drillings. *Quaternary International*, 473:55–65.
- Wunderlich, T., Wilken, D., Riedel, P.-B., Karle, M., and Messal, S. (2015b). Marine magnetic and seismic measurements to find the harbour of the early medieval slavic emporium groß strömkendorf/eric, germany. *Archaeologia Polona*, 53:543–546.
- Wyllie, M. R. J., Gregory, A. R., and Gardner, L. W. (1956). Elastic wave velocities in heterogeneous and porous media. *Geophysics*, 21(1):41–70.

List of Figures

2.1	Left column: Schematic view of different measurement setups including stationary floating electrodes (setup F , a), stationary submerged electrodes (setup S , b) and towed floating electrodes (setup T , c). Right column: Images of two-layer (2L , d) respectively three-layer cases (3L , e) approximating metre-scale targets. “C” indicates the current electrodes and “P” the potential electrodes of the streamer.	14
2.2	a) Location of Eckernförde Bay in Germany, b) Profile using setup F in Eckernförde Bay, Baltic Sea, Germany. Ranging-poles mark the profile of 40 m length in which the 20 m long, inverse Schlumberger multi-electrode streamer is positioned.	15
2.3	Sketch of a geoelectric measurement cycle, showing a) the strength of the injected current and b) the measured potential differences with time within the time window of two half cycles. The red line describes the full length of either 0.5 s or 0.25 s used for the measurements. The blue box highlights the time interval of current injection. The yellow line shows the interval for the calculation of the mean measured value of current and potential, from which the standard deviation is given, defining the measurement noise.	17
2.4	Simplified drawing of measurements carried out parallel to the coastline causing a deflected streamer, approximated by the height of a small circle segment. α is the centre angle of the arc, r is the circle radius, b is the length of the streamer, s is the secant, a is the orthogonal displacement from the midpoint, e is the relative inline displacement. C1 and C2 are the current electrodes, P7a and P7b are the potential electrodes, f is the distance between P7a and C1 respectively P7b and C2, g is the distance between P7a and C2 respectively P7b and C1.	19
2.5	Subsurface models used for forward calculations in the 2L case for a) a shallow water environment, setup F , b) a shallow water environment, setup S and c) an onshore environment, as well as in the 3L case for d) a shallow water environment, setup F , e) a shallow water environment, setup S and f) an onshore environment.	20
2.6	Comparison of mean values a)-c) and relative standard deviations d)-f) from repeated measurements for eight electrode pairs (y-axis) along the profile (x-axis). Left column: setup S (submerged), centre column: setup F (floating), right column: setup T (towed).	26

2.7	Sounding curves of a 2L case for various water depths (coloured curves) and a first layer resistivity of $0.3 \Omega\text{m}$ and a second layer resistivity of a) $1 \Omega\text{m}$ and b) $100 \Omega\text{m}$. Errors of setup T (blue error bars), setup F (red error bars) and streamer deflections (black error bars) from Eckernförde Bay repetition measurements are added.	28
2.8	Histogram of GNSS (global navigation satellite systems) coordinate deviations d , of all towed profiles from the average measurement profile calculated from a regression curve of the coordinates.	29
2.9	Comparative plotting of arithmetical average values (a-c) and relative standard deviations (d-f) of eight 2D inversion results calculated from repetition profiles of Eckernförde Bay with the software RES2DInv. a), d) setup S (submerged), b), e) setup F (floating) and c), f) setup T (towed).	30
2.10	Comparison of Schlumberger sounding curves for a 2L case (top row) and a 3L case (bottom row). 2L case: fixed top layer of 1 m depth and $0.3 \Omega\text{m}$ for a) setup F , b) setup S and $10 \Omega\text{m}$ for c) an onshore scenario. The resistivity of the second layer varies from $1 \Omega\text{m}$ – $1000 \Omega\text{m}$. 3L case: fixed top layer of 1 m depth and resistivity values of $0.3 \Omega\text{m}$ for d) setup F , e) setup S in a shallow water environment and $10 \Omega\text{m}$ for e) an onshore scenario. Resistivity values of the second layer (1 m depth) vary from $1 \Omega\text{m}$ – $1000 \Omega\text{m}$, the third layer is fixed with $10 \Omega\text{m}$. Red box: array length used within the field measurements.	45
2.11	Required streamer length (y-axis) to resolve the specific resistivity of the homogeneous half space of a 2L case (x-axis) with a tolerance of 100%. We differentiate between a shallow water (a-c) and an onshore scenario (d) and the measurement setups S (submerged, a), T (towed, b) and F (floating, c-d). We use water depths from 0.2 m–2 m	46
2.12	Plot of the maximum depth to which a layer of variable thickness and resistivity can be differentiated from the surrounding sea-bottom. The depth is defined as the distance between the sea floor for a brackish water column of 1 m to the upper edge of the layer. The sea-bottom shows resistivity values of $1 \Omega\text{m}$ (a-c) and $10 \Omega\text{m}$ (d). The measurement uncertainties of setup S (submerged, a), F (floating, c-d) and T (towed, b) are compared.	47
2.13	Left column: Model results from the stochastic inversion, color-coded by their misfit values and normalized to the relative misfit of 14%. The black line represents the true model; the white dashed line represents the expected model. Right column: normalized correlation matrix of the subsurface parameters. Case 2L and setup F (a-b), case 2L and setup S (c-d), case 3L and setup F (e-f) as well as case 3L and setup S (g-h) are distinguished.	48
2.14	Comparison of sensitivity kernels from the inverse Schlumberger array used for repetition measurements in Eckernförde Bay, Germany, consisting of eight electrode pairs (Table 2.1). a) setup F and b) setup S are compared, the lateral highly sensitive area is framed in black.	49

2.15	Left column: Synthetic checkerboard pattern of 1 m × 1 m size with sub-surface resistivity values of 1 Ωm and 10 Ωm, an additional water column of 1 m depth and 0.3 Ωm resistivity for shallow water measurements. For d), one row of 2 m × 2 m pattern size and a lateral distance of 4 m was chosen. Right column: 2D inversions of synthetic checkerboard data. a) Onshore electrode setup, b) setup S, c) and d) setup F.	50
3.1	GPR profiles comparing the 400 MHz and 200 MHz antenna from GSSI using a SIR-4000 registration unit at the measurement location “Flooded gravel pit”. The data was processed with t_0 correction, bandpass filter, fk-filter, background removal and trace normalizing. The lake bottom is highlighted yellow; remarkable noise in the water column is framed blue.	54
3.2	GPR profiles comparing the 400 MHz and 200 MHz antenna from GSSI using a SIR-4000 registration unit at the measurement location “Swimming Pool”. The data was processed with t_0 correction, bandpass filter, fk-filter, background removal, and trace normalizing. The pool bottom is highlighted with a yellow dashed line, steps to the pool are framed blue and a lowered piped is marked with a red circle.	55
3.3	GPR profiles comparing the 400 MHz and 200 MHz antenna from GSSI using a SIR-4000 registration unit at the measurement location “River”. The two antenna frequencies were used to prospect different sections of the river with varying water depths. The data was processed with t_0 correction, bandpass filter, fk-filter, background removal, and trace normalizing. The river bottom is highlighted with a yellow (dashed) line, diffraction hyperbolas are marked with a red circle; multiples are emphasized via green dotted lines.	56
3.4	GPR profiles using a 400 MHz antenna with a SIR-4000 registration unit at the measurement location “Pond”. The data was processed with t_0 correction, bandpass filter, fk-filter, background removal, and trace normalizing. The bottom is highlighted with a yellow (dashed) line, diffraction hyperbolas are marked with red circles. Parts of much and no organic material in the water column are emphasized via green and blue frames.	58
3.5	a) Standard GPR acquisition system that consists of a floating box containing the GPR antenna, which is attached to a catamaran, which in turn is navigated by an inflatable boat using an electric motor. The positioning is realized with a total station. b) Measurement setup of a 200 MHz antenna in the swimming pool, using a floatable box. The position was set by hand each metre, based on rope markers.	59
3.6	Schematic drawing of the resolvable areas (horizontal resolution) following from different criteria: 2D/3D survey without migration (1st Fresnel zone, blue), 3D survey after 3D migration (the $\frac{\lambda}{4}$ criterion, pink), 2D survey with inline migration only (green). In addition, the footprint estimated from the 3 dB threshold of the inline antenna radiation pattern is shown for water depths > 1 m (red dashed line).	64

3.7	Comparison of the measured (yellow bar) and calculated attenuation coefficients (blue and red line) at the measurement location swimming pool (approx. 25 °C) for the 400 MHz and 200 MHz antennas. For the calculated attenuation coefficients, the imaginary part of permittivity is taken into account in one case (blue line) and neglected in the other (red line).	69
3.8	a) Amount of absolute reflection amplitude (summed up from the water surface to just below the lake bottom) at 5 m intervals along the profile at the measurement location "Pond", recorded with a 400 MHz antenna from GSSI. b) Plot of the reflection coefficient of the lake bottom along the profile.	70
3.9	Determination of the maximum penetration depth and its standard deviation (grey shading) for three measurement locations. The maximum penetration depth is defined as the intersection of the exponential fitted curve (grey solid line) through picked amplitude values with depth (coloured solid lines) and of the maximum noise level for type 1 and 2 (dotted lines). The "Swimming pool" (blue line), "Pond" (red line) and "Flooded gravel pit" (green line) are distinguished. The standard deviation of the maximum penetration depth is defined as the intersection of the deviation of the fitted exponential curve (dashed lines) and of the respective noise level. A distinction is made between a) the 400 MHz antenna and b) the 200 MHz antenna from GSSI.	72
3.10	Comparison of the horizontal resolution vs. the water depth based on the footprints of the first Fresnel zone (blue) and of the 3dB threshold of the antenna radiation pattern (red). Furthermore, the horizontal resolution under field conditions was determined (black dots) and fitted (green) based on the width of migrated diffraction hyperbolas in different water depths.	75
3.11	Comparison of directivity functions from far-field approximations, E-plane, air-water interface (black line), as well as from the experimental estimate at the measurement locations "Pool" (blue line) and "Pond" (red line). The 400 MHz antenna from GSSI was used.	76
3.12	a)-b) Unmigrated and c)-d) migrated GPR signal (a,c) and envelope (b,d) of steps from the measurement location "Swimming pool". The 400 MHz from GSSI with the registration unit SIR 4000 was used.	77
3.13	The physical parameter of relative permittivity (based on the CRIM formula) is shown as a function of the volumetric water content.	78
3.14	Absolute values of negative (dashed line) and positive (solid line) GPR reflection coefficients. The reference materials a) freshwater and b) water-saturated sand are distinguished. Their material contrast to clay-free rocks of various porosities is shown in the form of lines. In addition, their contrast with various other (in)organic and archaeological materials such as clay, granite, wood, sand, bricks, peat and gyttia is presented as bars. The values are calculated according to Tables 3.2-3.3.	79

4.1	Anisotropy axes of wood: (1) in the fiber direction; (2) in the direction across the fiber, radial to the annual rings; (3) in the direction across the fiber, tangential to the annual rings	89
4.2	Schematic drawing of: (a) the setup for electric resistivity measurements of wood using a Wenner α configuration; (b) 2 GHz Palm antenna used for dielectric permittivity measurements of wood. Anisotropy axes of wood are highlighted: (1) in the fiber direction; (2) in the direction across the fiber, radial to annual rings, (3) in the direction across the fiber, tangential to annual rings.	90
4.3	Wiggle plot of spreading corrected radar signals that change with increasing wood moisture content for: (a) spruce wood cube of size 10 cm \times 10 cm \times 10 cm in the fiber direction (red and blue marks highlight the picked amplitudes); and (b) spruce wood cube of size 10 cm \times 10 cm \times 50 cm in the fiber direction. Here, two possible definitions of the travel time through the wood cubes for kiln-dry and moisturized wood are compared: (1) the maximum signal amplitude from the direct wave respectively wood–metal interface (green); and (2) the zero position before the respective signal amplitude (yellow).	92
4.4	(a) Wood moisture content of oak (blue) and spruce wood (red) plotted against the wood watering time in days. (b) Development of wood density depending on the wood moisture content for oak (blue) and spruce (red).	96
4.5	Swelling α of oak (blue) and spruce wood (red) depending on the wood moisture content (a) in the direction across the fiber, radial to annual rings, (b) in the direction across the fiber, tangential to annual rings, and (c) in the fiber direction.	98
4.6	Electric resistivity of (a) oak and (b) spruce depending on the wood moisture content in the fiber direction (blue error bar), in the direction across the fiber, radial to annual rings (red error bar), and in the direction across the fiber, tangential to annual rings (yellow error bar). The equations of the fitted curves can be found in Table 4.6.	98
4.7	Dielectric permittivity of (a) oak and (b) spruce depending on the wood moisture content in the fiber direction (blue error bar), in the direction across the fiber, radial to annual rings (red error bar), and in the direction across the fiber, tangential to annual rings (yellow error bar). . . .	101
4.8	Comparison of relative material contrasts of oak wood (a) and spruce wood in tangential the direction across the fiber (b) to fresh water (left), sandy subsurface (middle), and clayey subsurface (right) for geoelectrical (Wenner α , blue), ground penetrating radar (GPR) (green), and seismic measurements (yellow).	102
4.9	Estimation of the maximum detectable depth position of a spherical (solid line) and cylindrical (dashed line) wooden body as a function of its diameter x . (a) Geoelectrical (Schlumberger) and (b) GPR investigations (400 MHz) as well as the subsurface materials fresh water (blue line), clay (black line), and sand (red line) are distinguished.	103

6.1 Location of Haithabu (red star) near Schleswig in Germany and detailed map of the location of "wreck III" in the Hedeby Noor (Kramer, 2000) (coloured orange). The geoelectric profile is coloured black, the seismic profile is coloured white. 120

6.2 a) Seismic profile (white line in Figure 6.1), crossing the "wreck III". A 3D "Ping-Pong" array (Wilken et al., 2019) was used. b) Geoelectric profile (black line in Figure 6.1), that crosses the "wreck III". A 20 m long inverse Schlumberger configuration was used, whose electrodes were lowered 1m into the water column. 121

List of Tables

2.1	Inverse Schlumberger configuration used for Eckernförde repetition measurements.	15
2.2	Summary of relative standard deviations for different measurement setups arithmetically averaged from 40 measurement positions for the most affected electrode layout ($L/2$ [m], see Table 2.1). Additional aspects such as the bin size, the towing direction depending on the wind and the measurement cycle length are listed.	27
2.3	Relative standard deviations (1σ) for various measurement cycles of setup F . The values are determined from a single measurement position for an electrode layout of $L/2 = 10$ m.	27
2.4	Measurement errors resulting from noise, streamer deflections and water-level variations are estimated for an electrode of $L/2 = 7$ m and compared among the measurement setups.	27
2.5	Expected model and variance calculated from all models saved during the stochastic inversion using six iteration steps. The subsurface parameters layer thickness h_i and resistivity ρ_i are distinguished for the 2L and 3L case as well as for setup F and setup S	33
3.1	Comparison of water and soil properties and of the measurement setup for the GPR investigations at four different measurement locations: Swimming pool, Pond, River system and Flooded gravel pit.	57
3.2	Physical parameters of dielectric permittivity and volumetric water content of the reference materials freshwater and saturated sand based on data from Schön (1983) and Annan (2003).	67
3.3	Physical parameters dielectric permittivity and volumetric water content of the reference materials of different target materials. The values are based on data from Schön (1983), Annan (2003), Corradini et al. (2020), Fediuk et al. (2020b) and Knödel et al. (2013).	68
3.4	Comparison of the attenuation coefficients for the measurement locations “Flooded gravel pit”, “Swimming pool” and “Pond”. They were determined based on field data using Equation 3.37 and additionally calculated with Equations 3.38 and 3.40.	69
3.5	Comparison of the mean GPR signal/noise ratio type 1 (water ringing) and type 2 (common noise) of processed data at the measurement locations “Pond”, “Swimming Pool”, “River” and “Flooded gravel pit” and the antenna frequencies 200 MHz and 400 MHz. The values are given in dB ($10 \cdot \log(S/N_{Mean})$).	71

3.6	Comparison of the constant parameter $[\log(s_0 A_0 R) + \alpha s_0]$ (impact of the reflexion coefficient and the antenna parameters on the depth penetration) and of the attenuation α , as well as of the maximum depth penetration and its standard deviation, for the 200 MHz and 400 MHz antennas from GSSI calculated from GPR profiles at three measurement locations.	73
3.7	The suitability of GPR for resolving contrasts between the materials freshwater, sand, clay, peat, gyttja, wood and granite. Material contrasts of $ R > 0.1$ labeled with a check mark. When it might be that $ R < 0.1$, the checkmarks are parenthesised. Material contrasts of $ R < 0.1$ show a cross.	80
4.1	Reference values of the electric resistivity and dielectric permittivity for the embedding materials freshwater, saturated sand, and saturated clay.	93
4.2	Summary of the material parameters assumed for the wood and the embedding material, freshwater, saturated clay, and sand to discuss the implications for the depth range.	95
4.3	Summary of curve parameters fitting the wood moisture content u , swelling α , and density d for oak and spruce wood in three measurement directions.	97
4.4	Summary of physical wood properties for oak and spruce wood in the kiln-dry and in the saturated state.	97
4.5	Summary of electric resistivity values for oak and spruce wood in the kiln-dry and in the fully saturated state (extrapolated).	99
4.6	Summary of curve parameters fitting the electric resistivity and dielectric permittivity measurements for oak and spruce wood in three measurement directions.	100
4.7	Summary of dielectric permittivity values for oak and spruce wood in the kiln-dry and in the fully saturated state (extrapolated).	100
4.8	Comparison of the reflection coefficient of unweathered oak and spruce wood with the subsoil and the water column for the following methods: electric resistivity tomography (ERT), GPR, and seismics. For ERT and GPR, the range of material contrasts determined in the radial direction across the fiber (first value) and in the fiber direction (second value) are given. The seismic reflection coefficients were calculated for pine instead of spruce wood.	103
4.9	Comparison of wood swelling observed during our experiment and from the studies in Niemz and Sonderegger (2017).	104
4.10	Weighting of the influences of measurement errors, wood types, and anisotropy effects on the measured values of electric resistivity and dielectric permittivity.	104
4.11	Comparison of dielectric permittivity values of spruce wood depending on the wood moisture content observed during our experiment and in Niemz and Sonderegger (2017).	106

5.1 The feasibility of the geophysical methods geoelectrics, GPR and seismics with regard to the prospection of different material contrasts in aquatic environments. There are checks for all materials with $|R| > 0.1$. When $|R|$ might be < 0.1 , the checks are parenthesised. For materials with $|R| < 0.1$, crosses are used. 114

Danksagung

Mein Dank geht zuerst an Herrn Rabbel für die fachliche Begleitung der ganze Arbeit.

Zudem danke ich der ganzen Arbeitsgruppe Angewandte Geophysik für deren Unterstützung. Tina Wunderlich hatte stets gute Ratschläge sowie kleine Naschis parat und ist die schnellste Korrekturleserin. Mit Dennis Wilken hatte ich tolle Messkampagnen und konnte von seinen kreativen Ideen und der guten Zusammenarbeit sehr profitieren. Martin Thorwart hat mir mit Schokolade und als Ansprechpartner für alle möglichen und unmöglichen (IT) Probleme oftmals die Nerven gerettet. Ercan Erkul war einfach immer unterwegs, aber trotzdem für mich da.

Ich danke Clemens Mohr und Detlef Schulte-Kortnack für ihren technischen und menschlichen Support der Messungen. Harald Stümpel, Martin Proksch, Christina Klein und Manfred Wenk haben die Begeisterung für Messfahrten in mir geweckt. Diese Anfänge werde ich nie vergessen.

Nicht zu vergessen sind alle 8 anderen Doktorandinnen, die mit mir durchgehalten haben. Mit Michaela Schwardt hatte ich tolle gemeinsamen Jahre im SPP Projekt und im Büro. Danke, dass wir immer zusammengehalten haben. Ohne Katharina Rusch und Laura Dzieran wären Messfahrten und Fachschaftsabende undenkbar gewesen. Erica Corradini hat mit mir die Foo Fighters gerockt.

Zudem danke ich allen (damaligen) Hiwis und freiwilligen Helfer*innen, die an den Messungen beteiligt waren: Raphael Kahn, Lana Wallrabenstein, Felix Wolf, Peter Jung, Ines Budde, Marilisa Thomardakil und Anke Dannowski.

Ich danke Michael Gräber und Thomas Günther für ihre Zeit und deren externe Unterstützung.

Meine Mentorin Heidrun Kopp und Birger Lühr haben mich über viele Jahre lang begleitet und mir gezeigt, wo ich noch wachsen kann. Ganz herzlichen Dank dafür!

Katharine Simmons und Ulf Evert haben mir gezeigt, wie ich meine Wissenschaft vor mehreren hundert Leuten und dem Prinz von Jordanien kommunizieren kann und mich so immer wieder motiviert, durchzuhalten.

Ich danke allen Mitarbeiter*innen von Eastern Atlas, deren Flexibiliät es möglich gemacht hat, die Doktorarbeit fertig zu schreiben und trotzdem nach Chile und Jordanien reisen zu können. Danke Burkart Ullrich, Beate Wolff, Ron Freibothe, Henning Zöllner, Rudolf und Sandra Knieß, Niklas Royar, Robert Kell, Jessica Meyer und Lisa Voss.

Dann bedanke ich mich noch bei meinen lieben Freundinnen Josefine Hahn, Gesa Eirund, Svenja Ryan und Wilma Huneke für die schönen Studienjahre und eine absolut unvergessliche Zeit in Kiel. Ich sehe euch auf der ganzen Welt wieder. Kristin Burmeister danke ich für alle Höhen und Tiefen, die eine einzigartige Freundschaft hervorgebracht haben und für die Neugierde und die Lust auf das Leben.

Ich danke Tim Fischer und seiner frechen Mäuseschar, die mein Leben auf wunderbare Weise durcheinander gewirbelt haben und mir immer Halt geben.

Meinen Eltern Sigrun Meier-Fediuk und Friedhold Fediuk danke ich für ihre bedingungslose Unterstützung und dass sie mir die Liebe für Natur und Naturwissenschaften jedes Mal aufs Neue vermitteln können.

Erklärung

Hiermit erkläre ich, dass diese Arbeit – abgesehen von den angegebenen Quellen und Hilfsmitteln und der Beratung durch meinen Betreuer- nach Form und Inhalt meine eigene ist. Die Arbeit hat weder ganz noch zum Teil schon einer anderen Stelle im Rahmen eines Prüfungsverfahrens vorgelegen. Die Arbeit wurde – mit Ausnahme der einbezogenen und gekennzeichneten Publikationen – weder veröffentlicht noch zur Veröffentlichung eingereicht. Die Arbeit ist unter Einhaltung der Regeln guter wissenschaftlicher Praxis der Deutschen Forschungsgemeinschaft entstanden. Ein akademischer Grad wurde mir nicht entzogen.

Kiel, den 15.06. 2022

(Annika Fediuk)